RICE UNIVERSITY

Transport in Single Molecule Transistors

by

Lam H. Yu

A Thesis Submitted
in Partial Fulfillment of the
Requirements for the Degree

Doctor of Philosophy

Approved, Thesis Committee:

Douglas Natelson, Assistant Professor of Physics and Astronomy and Electrical and Computer Engineering

---

Qimiao Si, Professor of Physics and Astronomy

Kevin Kelly, Assistant Professor of Electrical and Computer Engineering

Houston, Texas

January, 2006

Abstract

Transport in Single Molecule Transistors

by

Lam H. Yu

As the size of a physical system decreases toward the nanoscale, quantum mechanical effects such as the discretization of energy levels and the interactions of the electronic spins become readily observable. To understand what happens when an isolated quantum mechanical object, such as an individual molecule, is coupled to a classical object, such as a macroscopic piece of metal, is one of the goals of modern condensed matter physics. The central question of our research is: How do the degrees of freedom of a single molecule (both electronic and mechanical) interact with an electrostatic environment under a constrained geometry? We have chosen to answer this question by looking at the electronic transport through single molecule transistors (SMTs), nanometer-scale transistors in which charge transport occurs through individual molecular states.

We use an electromigration technique to fabricate SMTs based on C_{60} and transition metal coordination complexes (TMCCs). In these devices, the molecule of interest is constrained between two metallic electrodes which act as reservoirs of

electrons and energy. At low temperatures, each transistor acts as a single-electron device in the Coulomb blockade regime.

Our experimental results suggest that the vibrational modes of the molecules contribute to the transport characteristics of the SMTs. From measurements of the differential conductance of these devices, we observe direct tunneling features that are consistent with vibrational excitations of the molecules. In the TMCC-based SMTs, we also observe inelastic cotunneling features that correspond energetically to vibrational excitations of the molecule, as determined by Raman and infrared spectroscopy. This is a form of gate-modulated inelastic tunneling spectroscopy.

In some of the SMTs we observe conductance features characteristic of the Kondo effect, a coherent many-body state comprising an unpaired spin on the molecule coupled by electronic correlation effects to the conduction electrons of the leads. The inferred Kondo temperature in these devices typically exceeds 50 K. In TMCC-based SMTs that exhibit the Kondo effect we observe unusual transport characteristics that deviate from the simplest model of Kondo physics in single electron devices. We suggest possible mechanisms, including strong intramolecular exchange and electron-phonon interaction, that may explain the observed deviation.

Acknowledgments

To begin, I would like to thank my advisor, Professor Doug Natelson, for giving me the opportunity to work with and learn from him. He is a great teacher and researcher. The breath and depth of his knowledge of condensed matter physics is truly impressive. He is always patient and approachable. He has the ability to explain an idea from various perspectives, and he excels at coming up with apt physical pictures to describe difficult concepts. The experimental works described in this thesis are the fruits of both of our labors. Without his guidance and helpful suggestions, I am sure that much of my effort would have been misdirected.

I am grateful to my committee members, Professor Qimao Si and Kevin Kelly for giving up their time to provide me with advice and comments on my thesis.

Without the collaboration of Professor Jim Tour and his post-docs and graduate students, much of the work presented in this thesis would not have been possible. The transition metal coordination complexes described in thesis were synthesized by Jake Ciszek, who is my go-to-guy whenever I have chemistry questions.

I am thankful for the camaraderie provided to me by my fellow Natelsonites: Behrang Hamadani, Zachary Kane, Sungbae (Jay) Lee, and Aaron Trionfi. Our interesting discussions and their questions about my work really helped me grow as a scientist. I have learned much from each one of them, but I would like to especially thank Jay for his patience with me and his generosity in sharing his knowledge.

Professor Alex Rimberg and his students, especially Wei Lu and Jennifer Steele,

were tremendously helpful in teaching me about the operation of the scanning electron microscope. The Rimberg group also was my number one source for emergency liquid helium. They have helped me keep my experiment going many times when BOC Edwards failed me.

I am forever indebted to Mark Junker who introduced me to alcohol, Clayton Simien who is always smiling and taught me the joy of tree climbing, and Chris Oubre who throws the best party and taught me about buck knives.

I would like to thank Professor Van Lewis, Brian Hickey, Marci Hendrickson and Tim Gilheart. I have known them all for many years, and they have been my most loyal and best friends. Their kindness, good humor, and support help make me a better person.

Special thanks go to my girlfriend, Diane Larrabee. Without her love and support and proofreading of my thesis, my life and this thesis would be much poorer. She is my better half, a fine experimentalist, and a great cook too.

I want to thank my family. My Mom and Dad are the pillars of my life. They give me love and strength. I am inspired by their selflessness and industry. I also want to thank my brother. No one can make me laugh like he can. He is so funny and kind. Finally, I am truly thankful for my maternal grandmother. All my life I have known nothing but kindness and compassion from this lady.

Contents

Illustrations

Chapter 1

Introduction

This thesis details the results of our investigations of electronic transport through single molecules. The interfacing of a small number of molecules with macroscopic electrodes for electronic characterization is a thirty years old idea [1] that only recently has become technologically feasible to achieve [2,3]. The first molecular devices were of the two-terminal configurations including nanopore structures [4, 5], crossed wires [6–8], mechanical break junctions [9–13], and scanning tunneling microscope (STM) [14–19] or conducting probe atomic force microscope (AFM) [20, 21].

These two-terminal devices exhibit a number of interesting phenomena, including molecular rectification [22], negative differential resistance [4], and switching between low and high conductance states [5–7, 18, 19]. However, many of these two-terminal experiments employ relatively high bias voltage or subject the molecules in the device to significant mechanical deformation, thus making careful study of these systems difficult. We have chosen to concentrate our studies in the transport behaviors of three-terminal nanometer-scale planar single molecule transistors (SMTs) [23–25], following the works first pioneered by Park, *et. al.* [26–29]. A SMT is composed of metallic source and drain electrodes bridged by a single molecule of interest plus a gate electrode that couples capacitively to the molecule (see Fig. 1.1). The single molecule of a SMT is coupled by tunnel junctions to the source and drain electrodes,

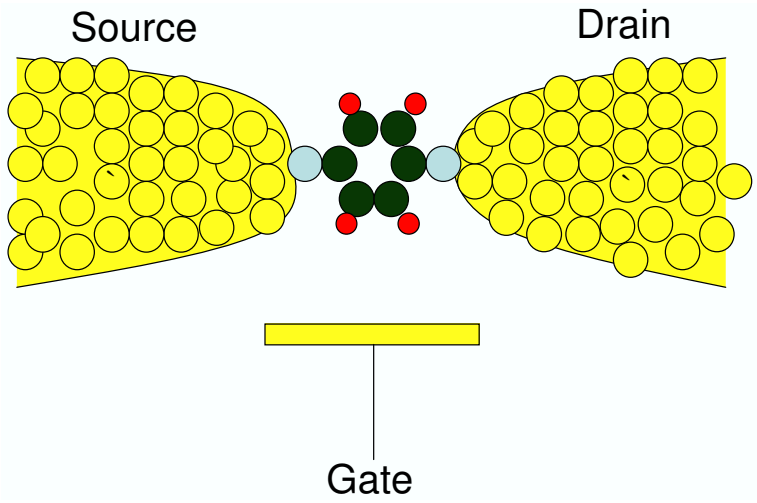

Figure 1.1 : A cartoon of a SMT.

but it is only capacitively coupled to the gate electrode, which is used to shift the molecular levels with respect to the source and drain Fermi levels. The three-terminal configuration of our devices provides us with *in situ* control of the energetic and charge state of the molecules in our devices. This added tunability has helped us understand the nonlinear effects observed in our molecular devices.

Charge transport through individual molecules is either nonresonant or occurs via the discrete molecular levels. In nonresonant transport, the molecule simply acts as a potential barrier in the device through which electrons must tunnel. In general, the tunneling current decreases exponentially with the molecule length [30], and this behavior has been studied in two-terminal molecular devices [31]. In our SMTs we observe resonant tunneling through molecular levels resulting in nonlinear conduction. When planar SMTs exhibit nonlinear conduction [23, 25, 27–29, 32],

they generally have electronic properties similar to that of single-electron transistors (SETs) [33].

At low temperatures, the average number of electrons on the molecule of a SMT can only be changed discretely due to quantum mechanical effects and electron-electron interactions. One can define an electron addition energy, E_a, associated with changing the charge on the molecule by a single electron. The electron addition energy is generally written as the sum of two contributions. The first is the single particle level spacing, δE; this is the energetic cost of promoting an electron on the molecule from the highest occupied molecular orbital (HOMO) to the lowest unoccupied molecular orbital (LUMO). The second contribution to E_a is a charging energy, E_C, which account for the Coulomb interactions on the molecule. A common approximation is to define a classical total capacitance, C, for the electron-electron interactions on the molecule, in which case one finds that the $E_C = e^2/C$.

For thermal energy $k_BT \ll E_a$, it is generally energetically forbidden at zero source-drain bias to change the charge state of the molecule. The resulting suppression of transport is called Coulomb blockade [33]. Coulomb blockade may be lifted in two ways. First, a source-drain voltage large compare to E_a applied across a SMT can allow resonant tunneling through the device. Second, applying voltage to the gate electrode can lift the blockade at zero source-drain bias by adjusting the electrostatic potential near the molecule so that it is energetically degenerate to change the charge of the molecule by one electron. It should be noted that higher order

processes such as cotunneling [34–38] and slow internal relaxation rate of electrons on the molecule [39] can allow transport in the classically blockaded regime.

One significant challenge in the fabrication of SMTs is that the required source-drain separation is on the order of one nanometer. We have succeeded in studying SMTs by using a combination of electron-beam lithography, electromigration technique [26] and statistical method. Our SMTs incorporate C_{60} molecules [23] as well as a new class of transition metal coordination complexes (TMCCs), created by our collaborators in the Tour group [25].

In approximately 10% of the devices we fabricate, Coulomb blockade behavior is observed. C_{60} vibrational resonances were observed in the transport characteristics of some of our C_{60}-based SMTs [23], consistent with observation made by Park,*et.al.* with similar devices [27].

New physical phenomena observe by our study include inelastic electron tunneling spectroscopy of single molecule and strong Kondo effect in SMTs. We develop a novel molecular vibrational spectroscopy technique in the TMCC-based SMTs [25]. The conduction of electrons through a SMT can be influenced by the vibrational energy levels of the molecule. When electrons interact inelastically with one of the molecular vibrational modes, a change in conductance is observed, and this transport-based spectroscopy is called inelastic electron tunneling spectroscopy (IETS). Unlike more conventional IETS [40, 41], our devices have the capability to measure the vibration spectrum of a single molecule while at the same time tuning the energetics of the

inelastic processes of the device by applying a voltage to the gate electrode.

We were the first to report that SMTs made with C_{60} exhibit the Kondo effect [23]. In general, the Kondo effect arises whenever an impurity with a single quantum mechanical degree of freedom (such as an unpaired spin on a molecule; it can either be spin up or down) is coupled to a system with many degrees of freedom (such as the combination of spin configurations of the conduction electrons). The Kondo effect observe in our C_{60}-based SMTs result from the formation of a many-body state comprising an unpaired spin on the C_{60} molecule and an antiferromagnetically coupled screening cloud of conduction electrons in the source and drain electrodes [42]. The signature of a Kondo resonance in a SMT is the appearance of a peak in the differential conductance near zero source-drain bias when the number of charges on the molecule is odd. This effect is only fully manifested below the Kondo temperature, T_K; the characteristic energy scale of the Kondo effect is $k_B T_K$. The T_K values of our C_{60}-based SMTs were in excess of 50 K.

We also observe Kondo resonances in the conduction of the TMCC-based SMTs with T_K in excess of 50 K. In these devices we find that the gate voltage dependence of the Kondo temperature is strongly inconsistent with the simple single-dot-level model of Kondo physics. We suggested that strong intramolecular exchange in the molecules is the cause of the non-trivial gate dependence, based on electronic structure calculations of the molecules.

This thesis is organized as follows: Chapter 2 describes the method we use to

fabricate the SMTs and the characterization of the individual components of our devices (such as the structure of the substrate and the chemical properties of the molecules). In chapter 3, we provide a detailed discussion of device characterization. This is of particular concern, since the lack of appropriate direct observational technique in determining the presence of a molecule in the inter-electrode gap. We discuss the theoretical treatments of SMTs in the Coulomb blockade regime in chapter 4. We focus on the case where sequential tunneling describable by a rate equation approach is the dominant mode of electron transport. We treat the case where only a few quantum levels are accessible. In chapter 5, we will describe the experimental result of our SMT related to the Coulomb blockade physics as detailed in chapter 4. A brief discussion of the theory of the second-order cotunneling processes, both elastic and inelastic, is given in chapter 6. Our newly developed technique of gate-modulated single molecule inelastic electron tunneling spectroscopy will be described in chapter 7. Chapter 8 will give a qualitative discussion of the theoretical treatment of the Kondo effect in SMT. In chapter 9, our experimental result with regard to the Kondo effect in SMT will be related. Some suggested mechanisms for the unusual transport behavior we observe in the Kondo regime of the TMCC-based SMTs will be described at the end of the chapter. Finally, chapter 10 will summarize the results and present the outlook. For a review of recent experimental and theoretical results in the study of single molecule transistors, I have consulted with a review article written by my advisor that will be publish in 2006 [43].

Chapter 2

Fabrication

A canonical SMT has metallic source and drain electrodes bridged by a single molecule of interest, and a third electrode called the gate which is used to shift the electrochemical potential of the molecule relative to those of the source and drain. At specific voltages applied across the gate, current flows between the source and drain electrode via the single molecule. Generally, the gate electrode is only capacitively coupled to the molecule and current flow between it and the molecule is assumed to be negligible. For all the experiments discussed in this thesis, the drain electrode is grounded.

Base on the specifications enumerated above, the fabrication of a SMT will require successful implementation and integration of three technical objectives: (1) Production of metallic lead pairs whose separation length is comparable to the dimension of a molecule $\sim$ 1 nm. (2) Placement and semi-permanent attachment of single molecules in the gaps created in objective 1. (3) Positioning of a metallic gate electrode at a distance from the single molecule of the device such that the separation between them is small enough to allow for gate manipulation of the electrochemical potential of the molecule, but large enough that current flow between the two are negligible.

We achieve objectives (1) and (3) by employing a electromigration technique [26]

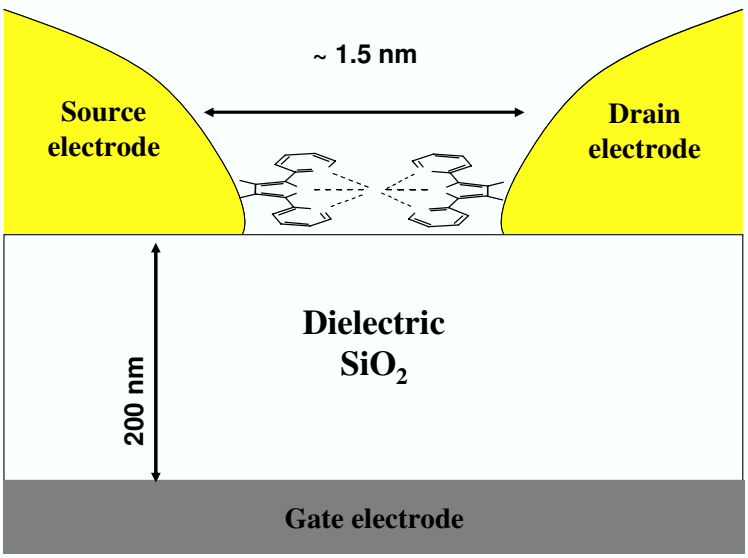

Figure 2.1 : A cross-sectional view of a SMT. The presence of the source and drain electrodes close to the molecule will increase the total capacitance C of the system, thus lowering the ratio C_G/C. Our capability of changing the electrochemical potential of the molecule is proportional to both the ratio C_G/C and the maximum gate voltage we can apply to the device without a gate failure. We have chosen to maximize the gate voltage we can apply across our devices by using a thick gate oxide layer (200 nm), even though this decreases C_G. This thick oxide layer allows us to apply very high electric field across our gate electrode, typically $\sim \frac{1}{2}V/nm$. This means that we can safely apply up to $\pm$ 100 V to the gate. In the end, the range of energy shifts possible in our devices from gating is not much different from devices using thinner SiO_2 or Al_2O_3 layers. [28, 29]

to form distinct source and drain electrodes from lithographically fabricated thin film metal constrictions made on degenerately p^+ doped silicon substrates topped by 200 nm of thermal SiO_2 [23]. Electromigration is a process in which the scattering of conduction electrons by static disorder in a metallic structure, such as grain boundaries, vacancies and impurity sites, results in momentum transfer from the electrons to the lattice [44]. This momentum transfer, commonly called the "electron wind force", leads to reconstruction of the metallic structure. The rate of electromigration is related directly to the current densities through the metallic structure. The degenerately p^+ doped silicon substrate is used as our gate electrode (see Fig. 2.1). The capacitance between the gate electrode and the molecule, C_G, is maximized when the molecule of the device is placed directly on the thermal SiO_2 layer. The shift in electrochemical potential of the molecule relative to those of the source and drain as a function of gate voltage, V_G, is proportional to C_G.

Our typical fabrication procedure is as follows. First, electron-beam lithography and standard development and lift-off processes are used to define 45 metal constrictions connected to contact pads on a silicon substrate like those described above. The transverse dimension of the narrowest portion of the constriction is typically 80-120 nm. The narrowness of the initial constriction ensures that the voltage require to perform electromigration is limited to a few hundred mV. This energy scale, while large compared to the biases used in subsequent characterization and measurement, is generally small compared to the electronic energies needed to break chemical

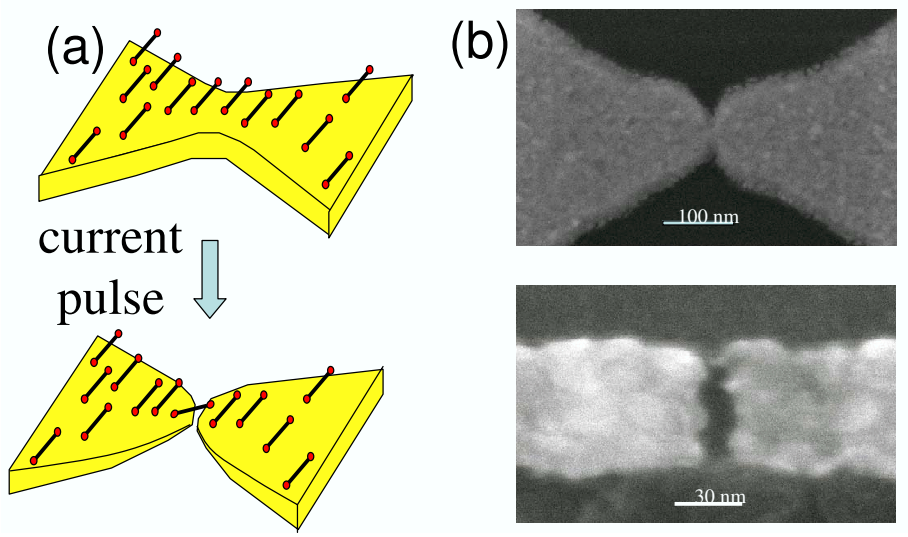

Figure 2.2 : (a) Cartoon of the electromigration process. A current pulse breaks a lithographically defined metal strip decorated with molecules into two electrodes by electromigration. In some devices, a molecule bridges the gap and has significant capacitive coupling to the underlying gate (see Fig. 2.1). (b)SEM images of the lithographically defined constriction before and after the electromigration process.

bonds. An example of such a constriction is shown in Figure 2.2b top. The metal, 1 nm of Ti (deposited at a rate of 0.1 nm/s) and 15 nm of Au (deposited at a rate of 0.2 nm/s), is deposited in an electron-beam evaporator with base pressure of 10^{-7} mB. The Ti layer is evaporated first, and it serves as an adhesion layer for the gold. After lift-off the surface is cleaned by UV ozone for 5 minutes and O_2 plasma for 1 min.

Next, the molecules of interest are deposited onto the metal structures. The method of deposition varies between different kinds of molecule. In this thesis, we will discuss SMT made with C_{60} molecules and a new class of transition metal coordination complexes (TMCCs), created by our collaborators in the Tour group at Rice University [25].

In the case of the C_{60}-based SMTs, an 80μL of C_{60} (1 mg C_{60}/4 mL toluene) in toluene solution is spin cast (spin speed $\sim$ 900 rpm) onto the metal structures. No particular precautions are taken to avoid exposure to ambient atmosphere during the spinning process. The C_{60} form a charge-transfer bond with the gold. It was shown by x-ray-photoemission (XPS), inverse-photoemission, and surface-enhanced Raman scattering measurements that adsorption of C_{60} on gold results in charge transfer and leads to additional bonding beyond Van der Waals bonding [45, 46]

Theoretical and experimental studies have shown that the C_{60}-Au binding energy is $\sim$ 1 eV, and the distance between the C_{60} center (C_{60} diameter $\sim$ 0.8 nm) and the gold surface is about 0.6 nm [45–49]. Scanning tunneling microscopy (STM) images

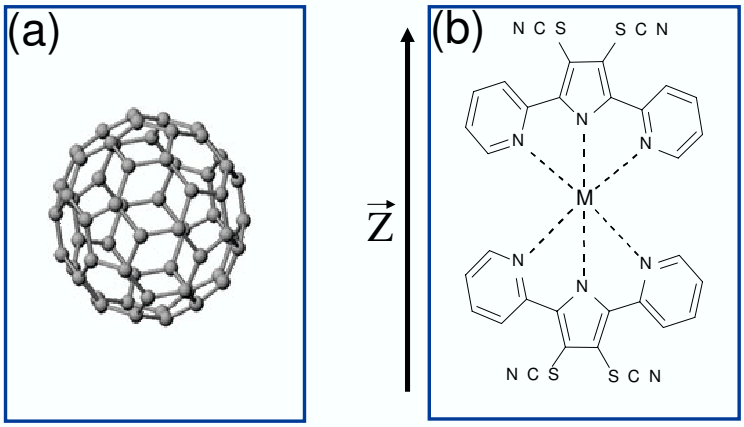

Figure 2.3 : Structure diagram of the molecules used in this thesis.

of C_{60} deposited by the spin casting on an evaporated Ti/Au film show approximately monolayer coverage of the metal by the adsorbed molecules [50].

Figure 2.3b is a structure diagram of the TMCCs used in our later studies, as-synthesized. In these neutral complexes, a transition metal ion (M) is coordinated by two planar, conjugated ligands perpendicular to each other, providing an octahedral crystal field compressed along the inter-ligand (z) axis. We have examined complexes with M = Co, Cu, and Zn, as well as individual ligands and alkane chains. The as-synthesized molecules are characterized by EPR, SQUID, x-ray diffraction, cyclic voltammetry (CV), IR, and Raman spectroscopy [25]. The Co(II) complex is high spin (3/2), with CV in solution suggesting easily accessible Co(II) $\leftrightarrow$ Co(III) redox transitions. The Cu(II) complex is spin (1/2), with CV supporting easily accessible Cu(II) $\leftrightarrow$ Cu(I) redox transitions. These complexes self-assemble on Au in tetrahydrofuran (THF) through loss of the -CN moieties and formation of Au-S covalent

bonds. The binding energies of Au-CN and Au-S are $\sim$ 3.90 eV and 1.73 eV, respectively [51–53]. The theoretical size (in the z direction) of a Co-based TMCC is 1.4 nm, and the measured thickness from ellipsometric measurement of a self-assembled monolayer of the molecule is around 1.28 nm [25, 54]. In fabricating TMCC-based SMTs, the chip containing the lithographically defined metal structures is soaked in a solution (1.5 mg TMCC/ 1mL THF) of the molecules in THF in the dark for 48 hours. During the soak, the TMCC self-assemble on the metallic structures. After the soak, the chip is rinsed in THF and dried in a nitrogen stream.

After the deposition step, the chips are placed in a variable temperature vacuum probe station (Desert Cryogenics) for the electromigration procedure and subsequent electrical characterization. After placement of the chip, the probe station is evacuated by a turbomolecular pump, and when the pressure in the probe station $< 10^{-4}$ mB, an inline cold trap is filled with liquid nitrogen for cryopumping. The base pressure of probe station at 300 K is 4 x 10^{-7} mB.

Our next step is to use electromigration to produce inter-electrode gaps between our lithographically defined metallic constrictions, a technique pioneered by Park *et.al.* [26] (see Fig. 2.2a). The precise electromigration procedure used for gap generation varies between research groups. We employ a two-step electromigration technique to separate the constrictions into distinct source and drain electrodes. Using an HP 4145B semiconductor parameter analyzer, at 300 K the voltage across each junction is ramped from 0 to 400 mV while monitoring the resulting current. When

electromigration-induced junction breaking begins, indicated by decreased junction conductance, the maximum voltage across the junction is reduced in steps of 40 mV until the junction resistance is increased to 400-1000 Ω. Once each junction is "partially broken", the sample is cooled to liquid helium temperatures. At 4.2 K the electromigration process is continued, with the maximum voltage ramps across the junction increased in steps of 200 mV as the junction conductance decreases. This process is halted when the resistance of the resulting electrodes exceeds 100 kΩ. This requirement ensures that no significant metallic bridge remains connecting the source and drain electrodes. We note that while the rate of electromigration is enhanced by elevated temperature because of the temperature dependence of atomic diffusion processes, electromigration is a non-thermal process. The breaking of a nanoscale constriction is not from local melting. Empirically, melting leads to comparatively large inter-electrode separation (> 5 nm) and electrode morphologies ill-suited to SMT experiments.

One advantage of performing the final breaking at cryogenic temperatures is that the probe station is at an effective ultrahigh vacuum environment at those temperatures (The base pressure of the probe station at 4.2 K is $\sim 10^{-7}$ mB), thus minimizing the risks of unintentional contamination of the newly exposed electrode surfaces by confounding adsorbates. Another consequence of performing the electromigration at low temperature is that the configuration of the resulting electrode surfaces is metastable upon breaking, due to the inhibition of surface reconstruction at cryo-

genic temperatures. Upon raising such devices to room temperature, even in UHV conditions, we observe the devices' gap size change significantly as diffusion of metal atoms increases. This is particularly relevant in our devices because Au is known to have large bulk and surface atomic diffusion rates and undergo annealing at room temperature.

Our two-step electromigration technique allows us to make relatively high conductance electrodes consistently, which we infer corresponds to a very small inter-electrode gap. Accurate scanning electron microscopy (SEM) assessment of the inter-electrode gap is difficult because of the surface reconstruction at room temperature discussed above. From SEM images of the resulting electrodes (Figure 2.2b bottom), we can see that the separation is less than 2 nm, the resolution of the SEM. Since the molecules of interest in our experiments are ~ 1 nm in size, closely spaced electrodes are essential for our SMTs.

Thus far in our discussion, I have avoided stating directly how we achieve technical objective (2), the placement of single molecules into the gaps. The semi-permanent attachment part of the objective is achieve by choosing molecules that will attach chemically to gold. However, the placement of the molecules of interest into the gap formed by electromigration is entirely a statistical process. Basically, we make the gaps with electromigration, and statistically a fraction of the electrode pairs made will have a single molecule of interest be placed at the right place within the gap. Due to the stochastic nature of the electromigration process, every electrode pair made

will be different at the atomic level. Therefore, even if the closest inter-electrode separation is the right size for the molecule of interest, the presence of a molecule at that location is probabilistic. When a molecule is present, its coupling to the source, drain, and gate electrodes are determined by the microscopic arrangement of the gap region, which is uncontrollable and different in every device. We know of no atomic-scale imaging technique at present that is capable of directly assessing *in-situ* the presence of an individual molecule between source and drain electrodes and the morphology of the gold electrodes adjacent to the molecule. Furthermore, the local charge environment of the SMT is unknown *a priori* due to the existence of surface trap states at the oxide surface. However, by analyzing many samples statistically we can estimate the percentage of the starting junctions that will become SMTs given our fabrication procedure.

Chapter 3

Characterization

Due to the lack of microscopy techniques that would allow the direct assessment of the presence of a single nanometer-scale molecule at the source-drain inter-electrode gap and our less than optimal placement technique for the molecule, we must infer the presence of a molecule of interest in the gap from transport measurements. Because every electrode pair produced by electromigration is different at the nanometer scale, and the exact position, orientation and electrode coupling of the molecule are all probabilistic, a statistical approach with large number of devices is essential for a true understanding of transport data from our single molecule devices. Given the exponential sensitivity of tunneling probability to device geometry, even for devices that have a single molecule of interest in their gap, one may be concern that geometric variations from device to device would render systematic understanding impossible.

However, the geometric sensitivity of the tunneling probability is actually an advantage in our system. In scanning tunneling microscopy (STM) experiments, it is often possible to obtain tips capable of atomic resolution imaging without any special procedure to control the atomic morphology of the tips. This is because, provided that the densities of states of the tip are smooth and featureless, conductance data obtained through tunneling experiments are essentially insensitive to the detailed shape of the tip. Most of the transport characteristics in a STM experiment are

dominated by the atom on the tip closest to the substrate. Similarly, in our SMT experiments, the conductances measured are dominated by the extremely small region around the point of minimum inter-electrode separation. The gaps form by electromigration are often irregular in shape, and this mean that in most junctions there is only one point of least distance between the source and drain electrodes. If a molecule happens to be placed at that point of the gap, then the transport characteristics of the device will be dominated by the transport through that single molecule. Even when there are other molecules and adsorbates near that single molecule, the transport behavior of the device will still be dominated by the molecule at the point of least inter-electrode distance due to the exponential sensitivity of tunneling to geometry.

Given the variability of molecular positions inherent in the electromigration process, we need to characterize and analyze hundreds of devices fabricated with the molecules of interest as well as control devices, so that when we look at a set of transport data (i.e. conductance as a function of source-drain bias and gate voltage) from a particular device we can tell whether the data are resulted from a device with the molecule of interest or are from spurious artifacts. To ensure systematic characterization of our molecular devices, we perform many control experiments including:

- (1) Ellipsometry, x-ray photoemission, infrared and Raman spectroscopy and STM on large area 1 nm Ti / 15 nm Au films ($\sim$ 1 mm^2), prepared identically (*e.g.* metal evaporation, surface cleaning and molecular deposition) and

simultaneously with the actually devices. These tests allow us to quantify the self-assembly process of the molecules on Ti/Au structures and the vibrational modes of the molecules.

- (2) Transport measurements of junctions prepared and tested as actual devices except that these junctions are exposed only to solvents used to prepare the molecular solution (toluene for the C_{60}-based devices and THF for the TMCC-based device). These junctions serve as a control to identify possible spurious effects from adsorbed solvent contaminants.

- (3) Transport measurements of junctions prepared and tested as actual devices except that these junctions are exposed to thiolated alkane molecules in solution. These junctions allow us to compare the transport behavior from devices made with our molecules of interest and molecules whose transport characteristics are well documented. These control devices are expected to act essentially like tunnel junctions.

For device stability we generally limit the voltage amplitude applied across the source and drain, $|V_{SD}|$, of our devices to less than 200 mV. To ensure no leakage current flow between the gate electrode and the other electrodes, the gate voltage amplitude, $|V_G|$, applied to the devices is limited to be less than 100 V. All transport measurements are performed in a variable temperature vacuum probe station using an HP 4145B semiconductor parameter analyzer at cryogenic temperatures. We note that most measurements are performed while the devices are in the dark, to avoid any

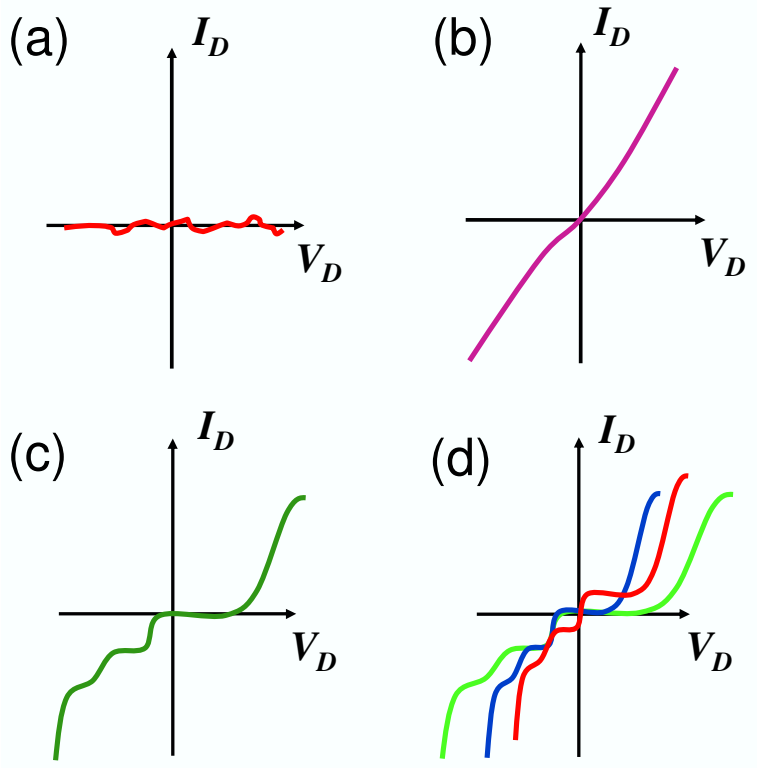

Figure 3.1 : The four kinds of IV curves seen in experiments. (a) No measurable inter-electrode conduction. (b) Linear or weakly nonlinear conduction with no significant V_G response. (c) Strongly nonlinear conduction with no significant V_G response. (d) Strongly nonlinear conduction with significant V_G response.

spurious photoconductance effects. For devices prepared with the molecules of interest, conduction characteristics measured at low temperatures after electromigration can be divided into four general classes (see Fig. 3.1):

- (I) *No detectable source-drain current at bias amplitude < 100 mV.* The most likely explanation for these conduction characteristics, confirmed by SEM observation, is that the resulting inter-electrode gaps of these devices are too large for detectable conduction by either tunnelings or thermionic or field emission.

- (II) *Weak nonlinearity, no gate response.* Transport data of these devices can usually be fitted by direct tunneling. Upon subsequent examination by SEM, these devices generally show nanometer-scale inter-electrode gaps. The natural interpretation is that in these devices, tunneling junctions have been formed, but no molecule of interest is located at the point of closest inter-electrode separation.

- (III) *Strong nonlinearity, no gate response.* Such transport characteristics can arise when a molecule, multiple molecules, contaminants, or metal nanoparticles are positioned between the source and drain, but the object is positioned in a way that results in extremely poor gate coupling. With no gate dependence, it is impossible to establish the origin of the nonlinearity in the transport behavior.

- (IV) *Strong nonlinearity, gate response.* These are the devices of the most in-

terest, since the gate response allows further investigation to determine whether the junction conductance is dominated by a molecule, multiple molecules, contaminants, or metal nanoparticles.

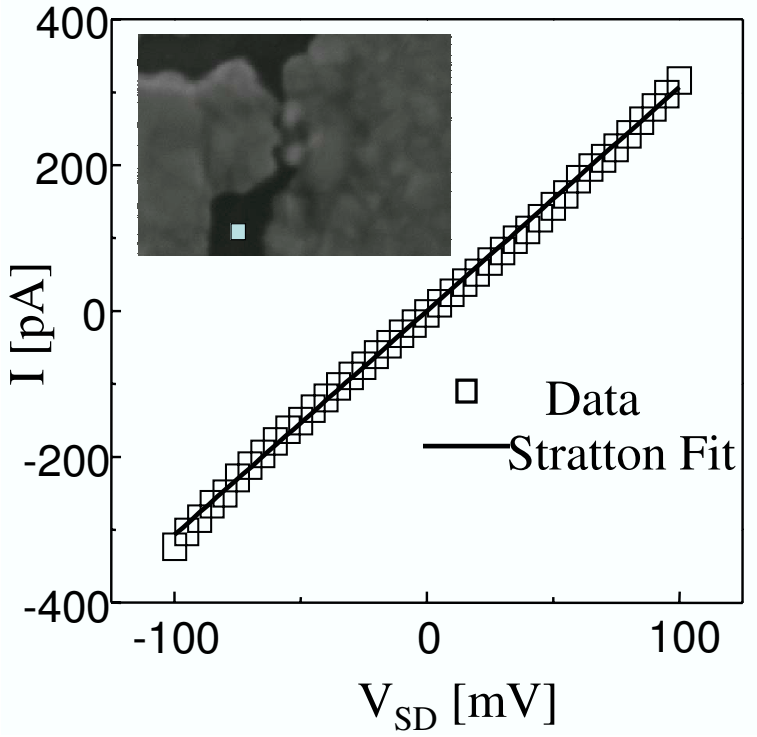

Figure 3.2 : IV curve of a tunneling junction. The fit indicate the size of the tunneling gap $\sim$ 1 nm. Insert SEM image of a electrode pair with small inter-electrode gap. The white square in the image has an area of 1 nm^2.

Interestingly, the proportions of device yield among the four classes of conduction characteristics are essentially the same in both the C_{60}-based and TMCC-based devices. We have examined 724 C_{60}-deposited, 407 Co-TMCC-deposited, and 225 Cu-TMCC-deposited electrode pairs, and the breakdown of conductance properties is 20%/40%/25%/15% for the classes I to IV, respectively. From over 500 control

junctions, the breakdown of conductance properties is 20%/78%/1%/1% for the four classes of data. For most control devices, their current-voltage curves reveal that they are tunneling junctions with gap size $\sim$ 1 nm (see Figure 3.2). This suggests that a significant fraction of the devices that exhibit class III and class IV transport characteristics are devices whose transport behaviors is dominated by the molecule of interest. However, not all gateable devices are SMTs because a small fraction of the control samples show some gateability.

To characterize the electronic conduction of a single-molecule device at a fixed temperature, it is useful to plot the differential conductance, dI/dV_{SD}, as a function of V_{SD} and V_G. These data are acquired by measuring the current, I, as a function of V_{SD} for each value of V_G using a HP4145B semiconductor parameter analyzer. The differential conductance is obtained by numerical differentiation of these data, using Savitzky-Golay smoothing to help reduce the noise in the resulting curves at the cost of V_{SD} resolution. This approach has the advantage of being significantly faster than lock-in techniques that directly measure the differential conductance via AC bias modulation. We have performed spot comparisons between the two methods, and found excellent agreement between the numerically computed values and those obtained directly from the lock-in technique. For a given temperature the resulting differential conductance is plotted as a function of V_{SD} and V_G in a conductance contour map, where the contrast of the map represents the conductance.

One common behavior observes in SMT is Coulomb blockade, the suppression

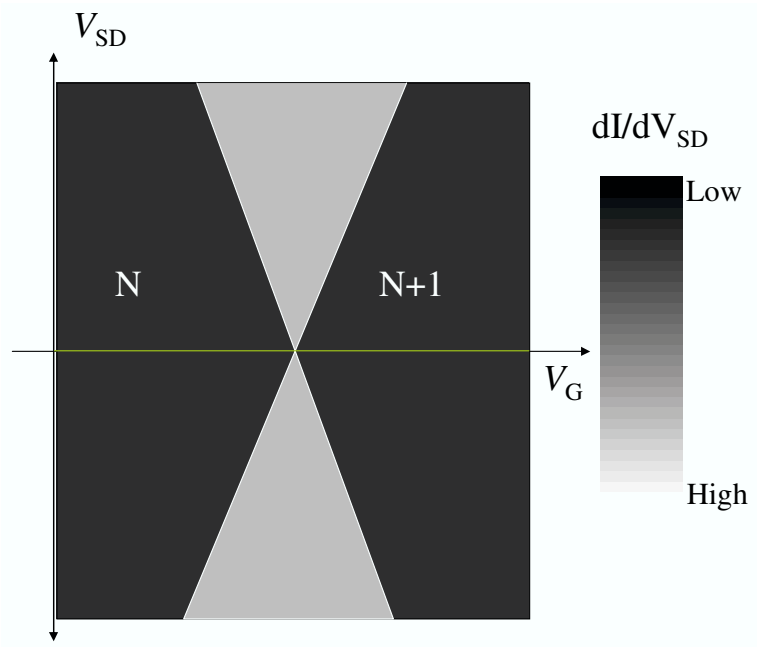

Figure 3.3 : A cartoon of a conductance map for a generic SMT. Brightness is proportional to differential conductance.

of transport when no molecular energy level is available for resonant tunneling between the source and drain electrodes. Coulomb blockade is a signature physical phenomenon that most single-electron devices including SMTs exhibit. Accounting for electron-electron interaction and molecular level spacing, one can define a charge addition energy associated with changing the charge on the molecule by a single electron. It is possible to use V_G to allow charge transport at zero source-drain bias by adjusting the electrochemical potential of the molecule so that it is energetically degenerate to change the charge of the island by one electron. Similarly, current may flow once eV_{SD} exceeds the charge addition energy. Mapping differential conductance as a function of V_{SD} and V_G, one finds a result like that shown in (Figure 3.3): diamond-shaped blockade regions where the charge on the island is quantized, separated by a "crossing point", called the charge degeneracy point, where, at $V_{SD} = 0$ and with increasing V_G, the occupation on the island changes from N to $N+1$ electrons. We will discuss the physics of Coulomb blockade in more detail in chapter 4.

Given that a molecule-deposited device exhibits gateable nonlinear transport characteristics consistent with Coulomb blockade physics, there are four other essential issues that must be considered before that device may be regarded as a SMT. First, we must decide whether the charge addition energy is of a sensible size for the molecule under consideration. The charge addition energy, which may be estimated from the maximum V_{SD} of the blockaded region on a conductance map, should be

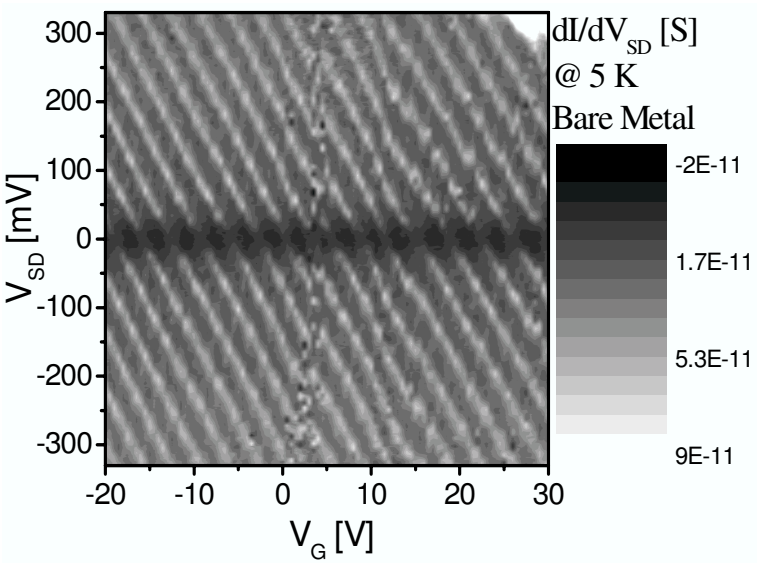

Figure 3.4 : Conductance map of a control device that exhibit Coulomb blockade at $\sim$ 5 K. This device has 17 clearly visible charge degeneracy points.

at least 50 meV for it to correspond to the Coulomb charging energy of a nanoscale object in a dielectric environment. Figure 3.4 shows the conductance map at 4.2 K for a particular control device made with no molecules intentionally deposited. There are clear Coulomb diamonds, indicating Coulomb blockade transport, and the charge addition energy is $\sim$ 25 meV. The relatively small value of the charge addition energy of this device implies that the object responsible for the observed Coulomb blockade behavior has size exceeding 40 nm in diameter. Therefore, it is most probable that this conductance map represent the transport characteristics of a gold nanoparticle created inadvertently by the electromigration process.

Second, we need to determine the number of reasonable accessible charge states for the SMTs. Solution-based electrochemistry provides an upper limit to the number

of valence states that is reasonably accessible for a molecular device made with a given molecule. In electrochemical experiments, such as cyclic voltammetry, the excess molecular charge is compensated by the presence of ions in the solvent. Since those ion can move to within a nanometer of the molecule, this screening should be more efficient than any possible in a conventional field effect geometry. For example, C_{60} may be reduced in solution seven times [55]. But we find that it is possible to add at least 17 electrons to the device whose conductance map is shown in Fig. 3.4 (the map has 17 charge degeneracy points). Clearly the data presented in Fig. 3.4 are inconsistent with the transport characteristics of a realistic C_{60} molecular device.

Third, to positively identify a SMT, we need to be certain that the gateable, nonlinear characteristics we observed in a molecule-deposited device are observed only in devices made with the same kind of molecule. We have observed Coulomb blockade with various charge addition energies in a small percentage of the control devices made with toluene, THF and thiolated alkane. These observations show that Coulomb blockade characteristics alone are not sufficient to confirm the molecular character of a molecular device. And this brings us to the final issue we need to consider: are there features in the data of a molecule-deposited device that uniquely specify the molecule? Known vibrational resonances in particular can be extremely useful, and we will discuss in detail the vibrational signatures we observed in our molecular devices in later chapters.

I hope that I have demonstrated that a systematic and statistical approach with

large number of devices is essential to studying molecular devices fabricated by electromigration, and that gate coupling is an important consideration when evaluating candidate SMTs. Without data as a function of gate voltage, it is extremely challenging to tell the difference between devices containing metal nanoparticles, adsorbed contaminants, and the molecules of interest. At times, even with gate dependent data, the situation is not always clear.

Chapter 4

The Coulomb Blockade Theory

4.1 Molecule as Tunnel Junction

The simplest transport behavior that a molecular device can exhibit is tunneling. The molecule acts as an insulating layer between two electrodes through which electrons from each electrode can quantum-mechanically tunnel. The two electrodes are termed the source and drain, and the electronic levels of each electrode are filled up to their respective electrochemical potentials (Fermi level), μ_S and μ_D. The difference between the electrochemical potentials is determined by the voltage, V_{SD}, applied across the device from an external circuit, such that μ_D - $\mu_S = |e|V_{SD}$. If we assume the molecule acts as a rectangular barrier with height ϕ, then in the limit where $V_{SD} < \phi$ and $T \to 0$, we can derive an equation for the tunneling current by the WKB approximation [56]

$$\begin{aligned} I(V) = \frac{|e|A}{4\pi^2\hbar d^2}\big((\phi - |e|V_{SD}/2)\exp^{-\frac{2d}{\hbar}(2m(\phi-|e|V_{SD}/2))^{\frac{1}{2}}} \\ - (\phi + |e|V_{SD}/2)\exp^{-\frac{2d}{\hbar}(2m(\phi+|e|V_{SD}/2))^{\frac{1}{2}}}\big). \end{aligned} \tag{4.1}$$

Here e is the elementary electric charge ($e = -1.602\times10^{-19}C$), $\hbar$ is Planck's constant, and A and d are the cross-sectional area and the length of the molecule. We can estimate ϕ as the difference between the work function of the electrode and the ionization potential of the molecule (see fig. 4.1). In the low bias limit, $V_{SD} << \phi$, we can linearize Eq.(4.1) and approximate the conductance of the device as $G \sim \exp^{-\frac{2d}{\hbar}\sqrt{2m\phi}}$,

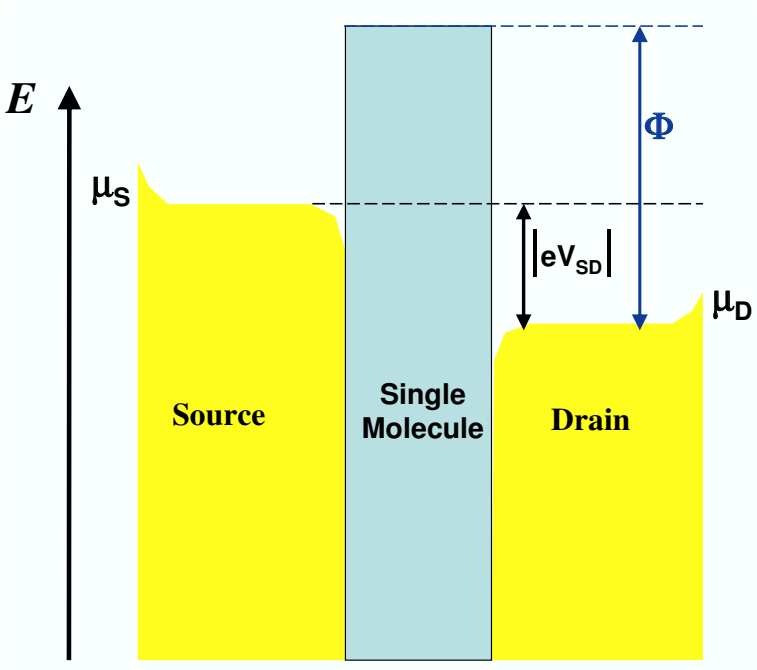

Figure 4.1 : Energy diagram to describe direct tunneling.

where $G = \frac{dI}{dV_{SD}}$. In this simple tunneling regime, as the length of the molecule increases, the zero-bias conductance of the device will decrease exponentially [30]. Such behavior has been observed in simple alkane-based molecular devices [31].

4.2 Sequential Tunneling Model

Another model for transport in a moleculardevice is sequential tunneling [33, 57–59]. In this regime the presence of a molecule between two electrodes is represented by two tunnel barriers sandwiching the discrete energy levels of the molecule (see fig. 4.2). The transparency of the tunnel barriers is determined by the contact between the

molecule and the electrodes. In the sequential tunneling model electrons are transported through the device via direct resonant tunneling (this is direct tunneling via a resonant state). The model assumes that the rate of electron relaxation within the molecule is fast compare to the electron tunneling rate into or out of the molecule, and it neglects higher-order tunneling processes such as cotunneling [33] which we will discuss later. At low temperature, electric current will flow through this device when electrons can sequentially tunnel onto the molecule and then off to the other electrode. This can occur only if there exists a molecular state between μ_S and μ_D, such that the number of electrons on the molecule can go from $N \rightarrow N+1 \rightarrow N$. When there are no molecular states between μ_S and μ_D, the transport of electrons through the device is "blockaded", leaving the number of electrons on the molecule fixed at N. In this blockaded state, a small current will flow by direct tunneling (see Eq.(4.1)) between the two electrodes. Sequential tunneling is observed in all the molecular devices described in this thesis.

This current blockade behavior which allow electron to be transport through the molecular device one at a time is called Coulomb blockade. This single electron transport behavior is a direct result of the discrete energy level structure of the molecule. The quantization of the energy levels of the molecule gives rise to two characteristic energies for the molecular device: the charging energy, E_C, and the quantized energy spacing between different electronic states of the molecule, δE [59].

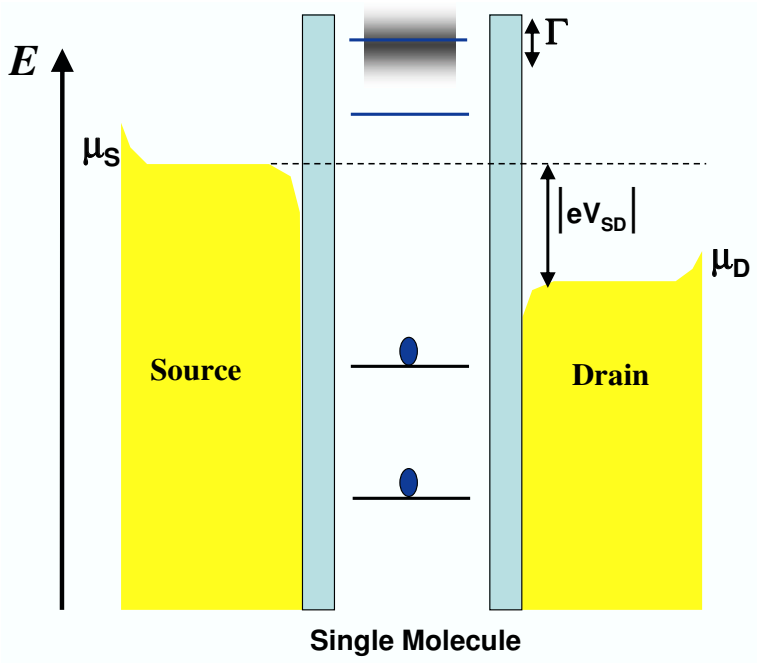

Figure 4.2 : Energy diagram to describe Sequential tunneling.

4.3 The Anderson Model

To see how these two characteristic energies come about in a molecular device let us look at the Anderson Hamiltonian which can be used to describe interacting electrons confined on a single level between two electrodes [60]. This simplified Hamiltonian considers electron-electron interaction, but does not include exchange interaction between electrons in the molecule or any vibrational modes associated with the molecule or the electrodes). The Anderson Hamiltonian is very general, and it could be use to describe any system where localized electrons exist in the presence of extended conduction electrons [59]. It has been used to understand the transport measurements in semiconductor quantum dots (also known as single electron transistors) which exhibit many of the physical effects we observed in SMT. In fact, much of the physics we will discuss in this thesis was first used to explain observations made in semiconductor quantum dots. [61–64].

The Anderson Hamiltonian is

$$\begin{aligned} H_A = & \sum_{\sigma;k<k_F;\alpha\in S,D} \epsilon_{k\sigma\alpha} c^+_{k\sigma\alpha} c_{k\sigma} + \sum_{\sigma;\nu} \epsilon_{\sigma\nu} d^+_{\sigma\nu} d_{\sigma\nu} + U n_\sigma n_{\sigma'} \\ & + \sum_{\sigma;k<k_F;\nu;\alpha\in S,D} t_{k\nu\alpha} c^+_{k\sigma\alpha} d_{\sigma\nu} + H.C. \end{aligned} \tag{4.2}$$

The Anderson model starts by describing the localized (on the molecule) and delocalized (in the electrodes) electrons, represented by creation operators, d^+ and c^+, respectively. The index k indicates the crystal momentum of an electron (k_F is the electron wavevector at the Fermi level) and the index σ represents the electron's spin, and the index α denotes the source and drain electrodes. The first term of the

Hamiltonian describes the energy of the delocalized electron in the Fermi sea of the electrodes. The second term represents the energy of the localized electrons in the molecules. Since the electrons on the molecule are localized, then by definition they have no crystal momentum, hence the k index is absent in the second term. The index ν labels all the single-particle levels of the molecule.

The third term of the Hamiltonian represents the effect of Coulomb repulsion on the energy cost of adding electrons on the molecule. Electrons interact with each other via Coulomb repulsion, and when one electron is added to a small region, the energy for adding a second electron is increased by a Coulomb repulsion energy U, possibly preventing the second electron from entering the same region. We can calculate U if we assume that all electrostatic interactions between the localized electrons on the molecule and all the electrons on the electrodes can be parameterized by the total capacitance, C, and that C does not depend on the charge state of the molecule. The total electrostatic energy for a molecule with N electrons is [59]

$$\frac{Q^2}{2C} = \frac{(Ne)^2}{2C}, \tag{4.3}$$

and since the Coulomb repulsion energy by definition is equal to (The total electrostatic energy/N^2), then

$$U = \frac{e^2}{2C}. \tag{4.4}$$

The total capacitance is at least as large as the self capacitance of the molecule. The self capacitance for a metal sphere of radius r that is capacitively coupled to an

electrode that is grounded to an infinite electron reservoir can be expressed as

$$C = 4\pi\varepsilon_0 r, \tag{4.5}$$

where ε_0 is the permittivity of free space. Finally, the last term in the Hamiltonian describes the tunneling transition between the localized and delocalized states, where $t_{k\nu\alpha}$ is the tunneling amplitude.

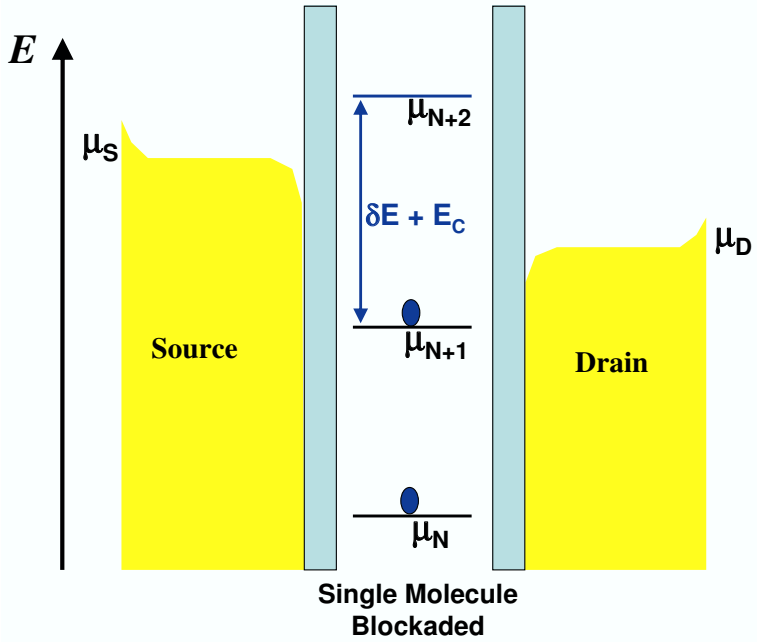

Figure 4.3 : Energy diagram showing a molecular level below the chemical potential of the source and drain, so there are N+1 electrons on the molecule (Blockaded).

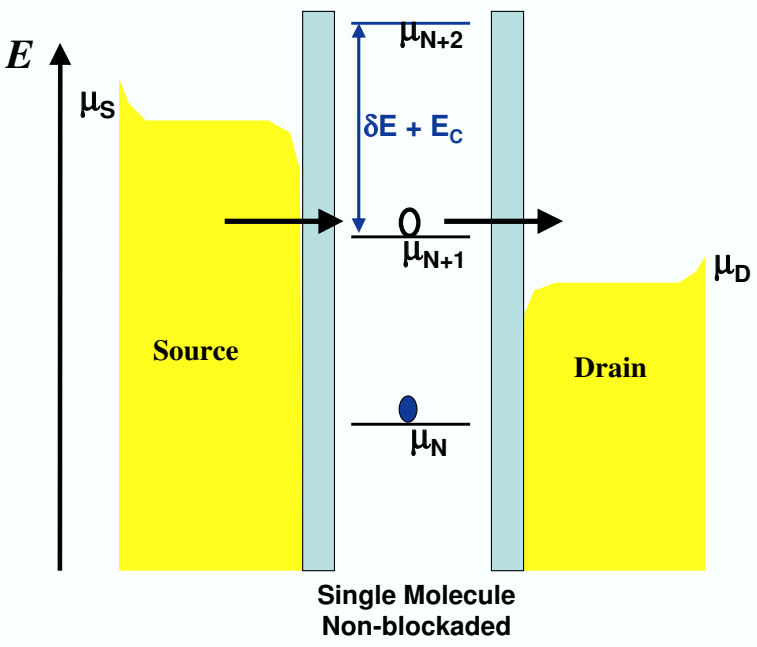

Figure 4.4 : Energy diagram showing a molecular level between the chemical potential of the source and drain (non-blockaded).

Let us ignore spin (but still allow the electrons to act like charged particles) and the electrode potentials for the moment and see what the Anderson Hamiltonian tell us. When N electrons are on the molecule, the total ground state energy on the molecule at zero temperature is

$$E(N) = \sum_{i=1}^{N} \epsilon_i + \frac{(Ne)^2}{2C}, \tag{4.6}$$

where ϵ_i is the chemical potential of the molecule with i electrons [59]. The electrochemical potential μ_N of a molecule with N electrons is

$$\mu_N = E(N) - E(N-1) = \epsilon_N + (N - \frac{1}{2})\frac{e^2}{C}. \tag{4.7}$$

From our previous discussion on sequential tunneling we note that as long as μ_N is

below both μ_S and μ_D, there will be N electrons on the molecule. Similarly, to have $N+1$ electrons on the molecule would require

$$\mu_{N+1} = \mu_N + \frac{e^2}{C} + (\epsilon_{N+1} - \epsilon_N) \tag{4.8}$$

to be below both μ_S and μ_D (see fig. 4.3). This mean that if there are N electrons on a molecule, then the external energy required to add one more electron to the molecule is $\mu_{N+1} - \mu_N = \frac{e^2}{C} + (\epsilon_{N+1} - \epsilon_N)$. The quantized energy spacing between adjacent electronic states of the molecule is defined as δE = $(\epsilon_{N+1} - \epsilon_N)$, and the charging energy is $E_C \equiv \frac{e^2}{C}$, which is the energy required to overcome the Coulomb repulsion to add one additional electron to the molecule. We will call $\frac{e^2}{C} + \delta$E the charge addition energy. In not including an index when defining δE, we are assuming that the molecular levels are evenly spaced. Although this simplification is not generally true in molecular systems, its use will not change any of the important physics we will be discussing. If there are N electrons on the molecule, then a current will flow through the molecular device as long as μ_{N+1} is between μ_D and μ_S (see Fig 4.4).

Now that we have derived the characteristic energies that are important in describing Coulomb blockade with the Anderson Hamiltonian, we need to determine the conditions under which this blockade behavior can be observed. As we have already noted, the blockade behavior results from the quantization of the energy levels of the molecule, and quantization is important when the energy levels are well defined. The conditions under which the energy levels are well defined are: (1) the thermal energy k_BT of the device should be much smaller than the charge addition

energy, (2) the uncertainty in the energy of each energy level (due to Heisenberg's uncertainty) must be much smaller than the charging energy, and (3) Γ, the intrinsic level broadening of the molecular energy level due to the tunneling between the electronic states on the molecule and the electrodes, must be much smaller than the thermal energy and the charge addition energy. These conditions can be summarized in terms of experimentally measurable parameters as [33]

$$k_B T << \frac{e^2}{C} + \delta E, \tag{4.9}$$

$$R_{contact} >> \frac{h}{e^2} = R_K, \tag{4.10}$$

$$\Gamma << k_B T, \frac{e^2}{C} + \delta E. \tag{4.11}$$

In equation(4.10), $R_{contact}$ is the contact resistance between the molecule and the electrodes, and $h/e^2 = R_K$ is the resistance of a single conductance channel. In the case of molecular devices, the $R_{contact}$ and C are depended on various factors including the microscopic geometry of the device nearest the molecule, the energy structure of the molecule, and the shape of wavefunctions of the molecular orbitals near the electrochemical potential of the source and drain electrodes.

We can see from equation(4.9) that even in the case where $k_B T > \delta E$, the blockade behavior is still observable as long as $k_B T << \frac{e^2}{C}$; we call this the "classical Coulomb blockade" regime. On the other hand, the case where $k_B T < \delta E$ and $k_B T << \frac{e^2}{C}$ is called the "quantum Coulomb blockade" regime [59]. We make a distinction between these two cases because the way that we calculate the current through

the device in each case is different. In the classical Coulomb blockade regime, an electron from an electrode can tunnel into a continuum of excited electronic states on the molecule, and the current through the device can be calculated from the tunneling rates averaged over many electronic levels. But in the quantum Coulomb blockade regime, individual tunneling rates are assigned to each quantum state. Most single molecule devices at cryogenic temperatures operate in the quantum Coulomb blockade regime. The δE of a typical molecule is of order eV, while k_BT at liquid helium temperatures ($\sim$ 4.2 K) is around 0.4 meV. In this thesis, all devices described will be assumed to be in the quantum Coulomb blockade regime.

In the quantum Coulomb blockade regime, the rate of electron tunneling between the molecule and the source and drain electrodes, γ_S and γ_D, are in general different for each quantum level of the molecule. The γ's are related to the tunneling amplitudes, t's, of the Anderson Hamiltonian in that

$$\gamma_\alpha \sim \Delta < t_{\alpha\nu}^2 >, \tag{4.12}$$

for $\alpha = S$ and D. Here Δ is the density of states in the α electrode (assume to be constant), and $t_{\alpha\nu}$ is the tunneling amplitudes that connect the state ν on the molecule with the state k in the electrode α [65]. The intrinsic level broadening is defined as $\Gamma = h\gamma$ and $\Gamma = \Gamma_S + \Gamma_D$. In the case of asymmetric coupling between the molecule and the two electrodes ($e.g$ $\Gamma_S >> \Gamma_D$), the current amplitude through the device in the non-blockaded state will be $|e|\gamma_D$ [66]. The general relation between the γ's and the current through the device in the non-blockaded state can be calculated

by solving the rate equations of the system, but before we discuses that, I would like to describe the effect of adding a gate electrode to a molecular device.

4.4 Single Molecule Transistor Physics

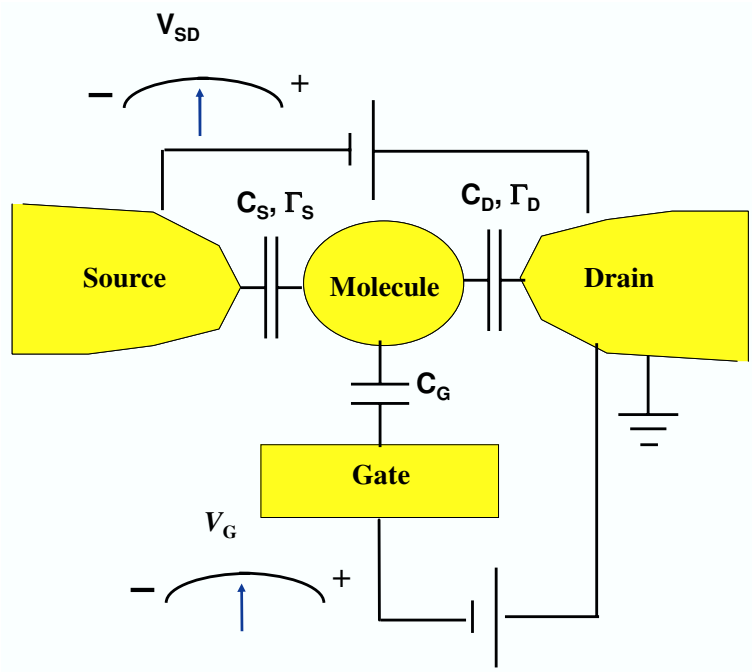

Figure 4.5 : A circuit diagram of a SMT.

With the addition of a gate electrode, the molecular device becomes a single molecule transistor. The term transistor refers to the ability to turn the current through the device on and off (change from non-blockade to blockade state) by manipulation of the gate voltage. A single molecule transistor consists of a single molecule of interest coupled capacitively to three electrodes, the source, drain and gate electrode, with

capacitances C_S, C_D and C_G, respectively.(see Fig. 4.5). As in the sequential tunneling regime, the molecule is also tunnel coupled to the source and drain electrodes. Whereas electrons are allowed to move between the molecule and the source and drain electrodes by tunneling, the transfer of electrons between the molecule and the gate electrode is assumed to be negligible. In our initial discussion of the SMT we will assume that both E_C and δE are large enough that only one additional charge state $N+1$ is accessible and that no electronically excitable quantum states are accessible for the molecule. In other words, we will initially assume for simplicity that only one electronic level on the molecule is available for tunneling namely, μ_{N+1}, and since μ_{N+1} can either be occupied or not, there are two possible occupation states, the N and $N+1$ charge state. Also, we assume there are no excited levels associated with the μ_N or the μ_{N+1} electronic levels.

In our discussion so far we have ignored the presence of the source and drain electrode potentials. In general the electrostatic energy of a single molecule transistor will depend on the charge on the molecule as well as on the applied voltages V_{SD} and V_G. We will now consider the effect of the electrode potentials, and we will see how the relative positions of μ_S, μ_D, and μ_{N+1} change with applied voltages. The inclusion of individual electrode potentials on the calculation of the total ground state energy at zero temperature, $E(N)$, causes the electrochemical potential to become [59]

$$\mu_N = \epsilon_N + (N - \frac{1}{2})\frac{e^2}{C} + eV_{dot}. \tag{4.13}$$

Here V_{dot}, the new term that describes the effect of the individual electrode potentials, is given by

$$V_{dot} = \frac{C_S}{C} V_{SD} + \frac{C_G}{C} V_G. \tag{4.14}$$

In defining V_{dot}, we have assumed the drain electrode is grounded. The total capacitance, C, is defined as

$$C = C_S + C_D + C_G. \tag{4.15}$$

We note from Eq.(4.9) and Eq.(4.10) that as long as $k_B T << E_C + \delta$E and $R_{contact} >> h/e^2$, a molecular device will exhibit single electron transport behavior. If there are N electrons on a molecular device, then from Eq.(4.13) and Eq.(4.14) and μ_D - $\mu_S = |e|V_{SD}$, we can see that for any given value of V_{SD}, there will be some range of V_G where μ_{N+1} is between μ_S and μ_D, and as a result current will flow through the device. Also, we can infer that the the range of V_G over which current will flow at a given V_{SD} is directly related to the amplitude of V_{SD}.

It is possible to have current flow at vanishing V_{SD} if the electrochemical potential of both leads is aligned with the first level available for tunneling ($\mu_S = \mu_D = 0 = \mu_{N+1}$). We will follow the convention that when $V_{SD} = 0$, $\mu_S = \mu_D = 0$. The gate voltage that realizes this condition is called the charge degeneracy point [59] and is defined by

$$V_0 = \frac{1}{|e|} \frac{C}{C_G} E_0. \tag{4.16}$$

Here E_0 is the electrochemical potential of the $N+1$ electron state when $V_{SD} = V_G = 0$. In other words, $E_0 = \epsilon_N + (N - \frac{1}{2})\frac{e^2}{C}$, so in general μ_{N+1}=E_0+V_0. If $V_{SD} \sim 0$,

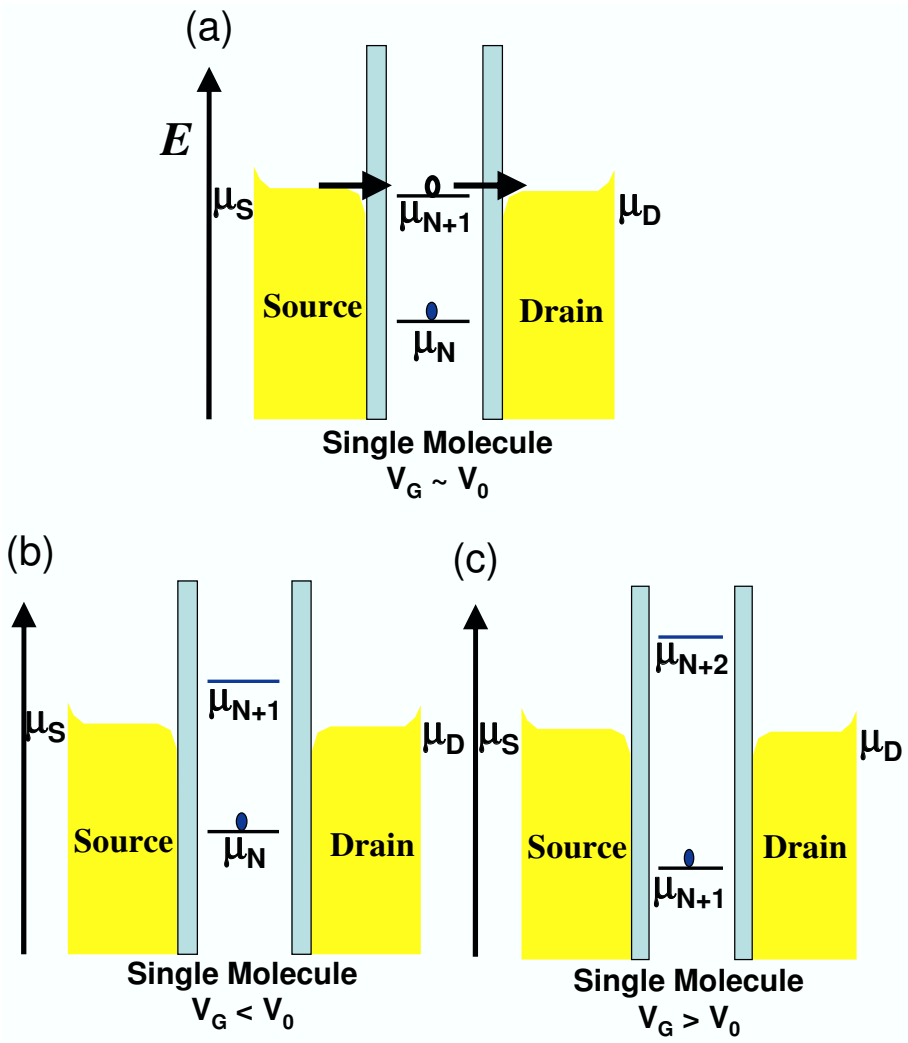

Figure 4.6 : An energy diagram that shows charge degeneracy. (a) show the case of charge degeneracy. (b) and (c) shows the cases just below and above charge degeneracy, respectively.

then current will only flow through a SMT when V_G =V_0 (see Fig. 4.6). At V_G =V_0, the two charge states N and $N+1$ of the molecule have the same energy, so an electron can hop on and off the molecule freely.

4.5 Rate Equation

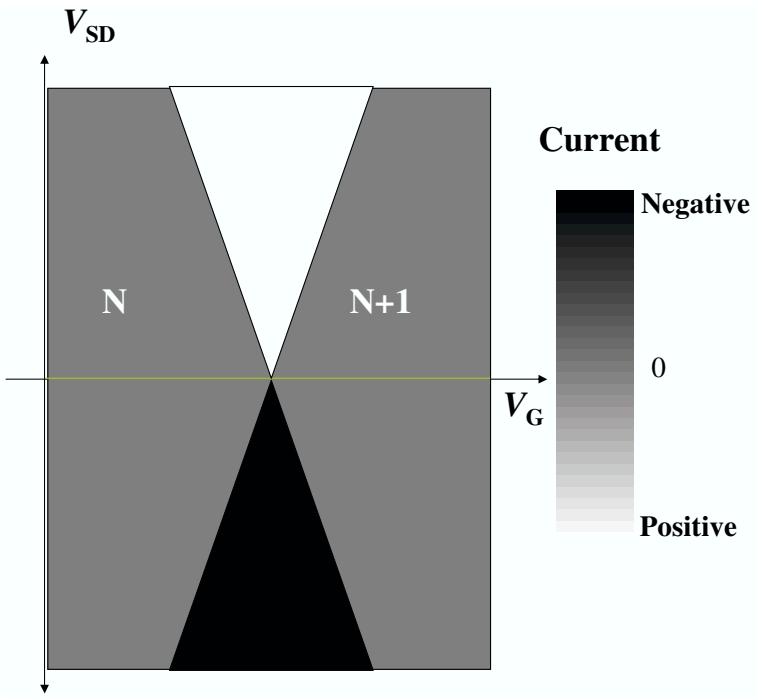

Figure 4.7 : A Cartoon of a current map.

From Eq.(4.13), Eq.(4.14), and Eq.(4.15), we have a general idea of the transport characteristics of a SMT. Qualitatively, we can infer that the current through the device as a function of V_{SD} and V_G will look like Figure 4.7. Let us introduce a quantitative way to calculate the current amplitude through a SMT using the rate

equation approach. Our discussion of the rate equation approach will follow closely the path used by Bonet *et. al.* [66]. The rate equations are a set of equations that describes the time evolution of the occupation probability, P_α , of state α given by

$$\frac{dP_\alpha}{dt} = \sum_\beta (T_{\beta\to\alpha} P_\beta - T_{\alpha\to\beta} P_\alpha), \tag{4.17}$$

where $T_{\alpha\to\beta}$ is the transition rate from state α to state β . Here α and β states refer to the occupation states (*i.e.* the N and $N+1$ states). The rate equation says that the rate of change of the occupation probability of a given state is the sum of the difference between the rate at which the occupation probability of a given state increases and decreases. The rate equation can be written in matrix form as

$$\frac{d\mathbf{P}_\alpha}{dt} = \mathbf{T} \bullet \mathbf{P}, \tag{4.18}$$

where the elements of the matrix $\mathbf{T}$ are given by:

$$T_{\alpha\beta} = T_{\beta\to\alpha} \ \texttt{if} \ \ \alpha \neq \beta, \ \ \texttt{and} \ \ T_{\alpha\alpha} = -\sum_{\beta\neq\alpha} T_{\alpha\to\beta}. \tag{4.19}$$

The matrix form of the rate equation is useful when solving a system with multiple states. Once the occupation probabilities for each state are determined at given values of V_{SD} and V_G, then the current can be calculated through either the source or drain tunnel barrier. In the steady state these two currents are equal. The current

through the source at equilibrium is

$$I = I_S = |e| \sum_{\alpha} \sum_{\beta} T^S_{\alpha\to\beta} P_\alpha, \tag{4.20}$$

where $T^S_{\alpha\to\beta} P_\alpha$ is the contribution of the source to $T_{\alpha\to\beta}$, multiplied by $+1$ or -1 depending on whether the given transition involves an electron going in or out from the electrode in question.

4.6 One Electronic Level Case

Let us solve the rate equation for the situation where the molecule has only one accessible level, μ_{N+1}. In this case the level can be occupied by either zero or one electron (the molecule is in the N or $N+1$ charge state) and the transition rates are given by:

$$T_{0\to1} = \gamma_S f_S + \gamma_D f_D \ \texttt{and}\ T_{1\to0} = \gamma_S(1 - f_S) + \gamma_D(1 - f_D). \tag{4.21}$$

Recall that γ_S and γ_D are the rates of electron tunneling between the molecule and the source and drain electrodes, respectively. The distribution functions, f_S and f_D, are given by

$$\begin{aligned} f_D &= \big(1 + \exp(\frac{\mu_{N+1} - \mu_D}{k_B T})\big)^{-1} = \big(1 + \exp(\frac{\mu_{N+1}}{k_B T})\big)^{-1} \\ f_S &= \big(1 + \exp(\frac{\mu_{N+1} - \mu_S}{k_B T})\big)^{-1} = \big(1 + \exp(\frac{\mu_{N+1} + |e|V}{k_B T})\big)^{-1} \\ \mu_{N+1} &= E_0 - |e|\frac{C_G V_G + C_S V_{SD}}{C} = -|e|\frac{C_G(V_G - V_0) + C_S V_{SD}}{C}. \end{aligned} \tag{4.22}$$

The applied voltages and temperature enter into the rate equation via the Fermi function. Putting everything together we find that

$$\begin{aligned}\frac{dP_0}{dt} &= -P_0(\gamma_S f_S + \gamma_D f_D) + P_1\big(\gamma_S(1-f_S) + \gamma_D(1-f_D)\big) \\ \frac{dP_1}{dt} &= P_0(\gamma_S f_S + \gamma_D f_D) - P_1\big(\gamma_S(1-f_S) + \gamma_D(1-f_D)\big) \\ &= -\frac{dP_0}{dt},\end{aligned} \tag{4.23}$$

and

$$I = \gamma_S(1-f_S)P_1 - \gamma_S f_S P_0. \tag{4.24}$$

We can solve for the occupation probabilities by noting that in equilibrium, $\frac{dP_0}{dt} = \frac{dP_1}{dt} = 0$. Therefore, the occupation probabilities are

$$P_0 = \frac{T_{1\to 0}}{T_{0\to 1} + T_{1\to 0}} \quad \texttt{and} \quad P_1 = \frac{T_{0\to 1}}{T_{0\to 1} + T_{1\to 0}}, \tag{4.25}$$

such that $P_0 + P_1 = 1$, and the current through the device at steady state is

$$I = |e|\frac{\gamma_S \gamma_D}{\gamma_S + \gamma_D}(f_D - f_S). \tag{4.26}$$

From Eq.(4.26), we can see that the current through the SMT is non-zero only when $f_D \neq f_S$. At low temperature this is only true if the sign of $(\mu_{N+1} - \mu_D)$ is opposite to the sign of $(\mu_{N+1} - \mu_S)$, which means $|\mu_D| < |\mu_{N+1}| < |\mu_S|$. Therefore, in agreement with our qualitative picture, a SMT is in the non-blockade regime when μ_{N+1} is located between the Fermi level of the source, μ_S, and drain, μ_D, electrodes. Figure 4.8 plots the calculated current from Eq.(4.26) as a function of V_{SD} and V_G. (Note its similarity with Figure 4.7). In Figure 4.9 we plot the differential conductance dI/dV_{SD} as a function of V_{SD} and V_G. This is known as a conductance map,

where the x-axis is the gate voltage, the y-axis is the source-drain bias, and the different brightness on the map represent the conductance. The theoretical results in this thesis are calculated using different spreadsheets and plotted using the Origin program. Most of the experimental results in this thesis will be presented as conductance maps that are plotted using the Origin program. The analytical form of dI/dV_{SD}, given by differentiating Eq.(4.26) as a function of V_{SD}, is

$$\begin{aligned}\frac{dI}{dV_{SD}} &= |e|\frac{\gamma_S\gamma_D}{\gamma_S+\gamma_D}\left(\frac{\partial(f_D-f_S)}{\partial\mu_{N+1}}\frac{\partial\mu_{N+1}}{\partial V_{SD}}-\frac{\partial f_S}{\partial V_{SD}}\right)\\ &= \frac{e^2\gamma_S\gamma_D}{k_BT(\gamma_S+\gamma_D)}\left((1-f_D)f_D\frac{C_S}{C}+(1-f_S)f_S\frac{C_D-C_S}{C}\right).\end{aligned} \tag{4.27}$$

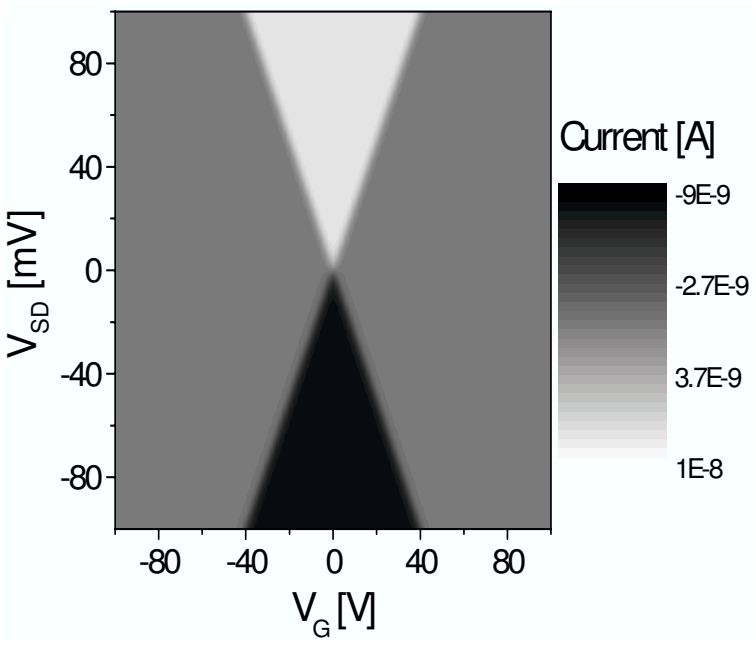

Figure 4.8 : Current map of a SMT with only one molecular level.

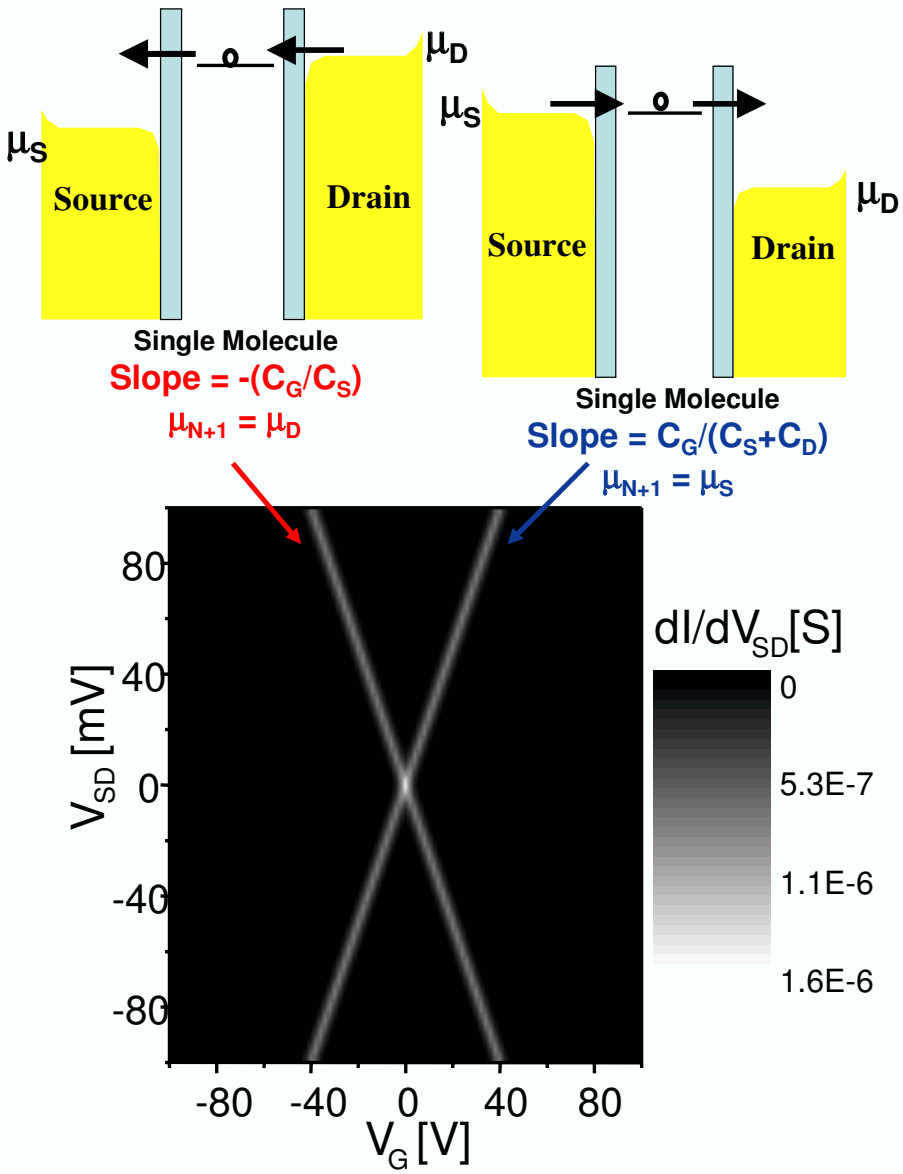

Figure 4.9 : Conductance map of a SMT with only one molecular levels. The two energy diagrams show the cases where the molecular level are aligned with one of the electrochemical potentials of the electrodes.

Equation(4.27) shows that the conductance is non-zero only when f_D and/or f_S has a value between 0 and 1. The condition for which $0 < f_D < 1$ is when

$\mu_{N+1} = \mu_D$. Similarly, $0 < f_S < 1$ only if $\mu_{N+1} = \mu_S$. We already found from our discussion of the degeneracy point that when $\mu_S = \mu_D = \mu_{N+1}$, the two charge states N and $N+1$ of the molecule have the same energy, so the number of charges on the molecule is degenerate. Now we find the other two conditions that denote charge degeneracy on the molecule: $\mu_{N+1} = \mu_D$ and $\mu_{N+1} = \mu_S$. The bright lines in Figure 4.9 represent the points in the V_{SD}-V_G parameter space where the number of charges on the molecule is degenerate. The dI/dV_{SD} line with the negative slope on the conductance map represents points where $\mu_{N+1} = \mu_D$, and the dI/dV_{SD} line with the positive slope represents points where $\mu_{N+1} = \mu_S$. We can relate the slopes of the dI/dV_{SD} lines with the capacitance to the different electrodes by recalling that $\mu_{N+1} = E_0 + eV_{dot}$ and $\mu_S = eV_{SD}$ when $\mu_D = 0$. Using Eq.(4.14), Eq.(4.16) and Eq.(4.22), we find that the condition for $\mu_{N+1} = \mu_S$ is

$$V_{SD} = \frac{C_G}{C_G + C_D}(V_G - V_0), \tag{4.28}$$

and the condition for $\mu_{N+1} = \mu_D$ is

$$V_{SD} = -\frac{C_G}{C_S}(V_G - V_0). \tag{4.29}$$

We note that the two slopes are different even when $C_S = C_D$, and this asymmetry is due to the fact that we set $\mu_D = 0$, in agreement with our experimental setup. In general, we do not expect the Coulomb blockade features in the conductance map to be symmetric with respect to the line $V_G = V_0$. We note that

$$(Slope_{\mu_{N+1}=\mu_S})^{-1} + (Slope_{\mu_{N+1}=\mu_D})^{-1} = \frac{C_G}{C}, \tag{4.30}$$

which is called the gate efficiency factor [67]. This factor is a measure of how well the molecule capacitively coupled to the gate electrode relative to the tunnel coupled electrodes; a larger gate efficiency factor means stronger gate coupling relative to the source and drain coupling.

4.7 Two Electronic Level Case

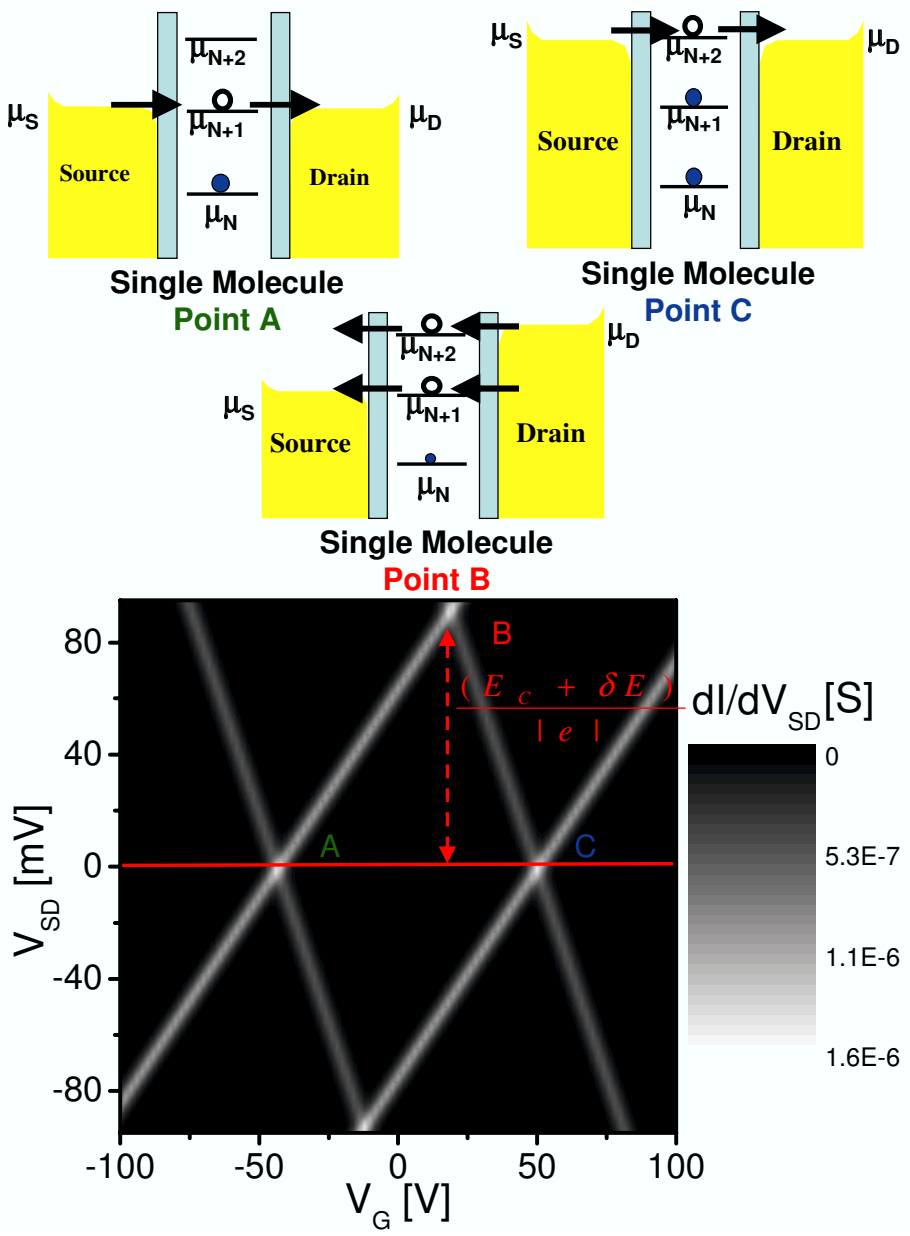

Figure 4.10 : Conductance map of a SMT with only two molecular level. The three energy diagrams demonstrate the energy level alignments at the three marked points.

So far in our discussion, we have concentrated on the case where both E_C and δE are large enough that only one additional charge state $(N+1)$ is accessible, and for the most part this is true in our experiments. However, let us briefly explore the consequences of allowing more then one electron to be added to the molecule in a SMT. Electron transport through multiple electronic levels of a molecule can be calculated by the rate equations, just like in the single level case. The two-level calculations are more tedious but similar to the single level case, so we will simply show the result. Figure 4.10 is a conductance map that describes a SMT with three accessible charge states. We have labeled the plots with 0, 1, and 2 corresponding to the N, $N+1$ and $N+2$ charge states. The areas on the conductance map where the number of charges on the molecule is well defined, thus exhibiting low current flow and low conductance, are called "Coulomb diamonds". The main consequence of electron transport through multiple charge states is the appearance of multiple Coulomb diamonds.

In Figure 4.10, point A is the degeneracy point where $\mu_{N+1} = \mu_S = \mu_D = 0$, and point B is the degeneracy point where $\mu_{N+2} = \mu_S = \mu_D = 0$. Usin Eq.(4.16), the gate voltage difference between points A and B is given by

$$|eV_G|_{A\to B} = \frac{C}{C_G}(\mu_{N+2} - \mu_{N+1}) = \frac{C}{C_G}(E_C + \delta E). \tag{4.31}$$

Let us look at Point C in Figure 4.10, which forms one of the boundaries of a Coulomb diamond. This is a point where two dI/dV_{SD} lines originating from two different degeneracy points cross on the conductance map. One of these lines denotes

points in the V_{SD}-V_G parameter space where μ_{N+1} is aligned with μ_S, and the other denotes points where μ_{N+2} is aligned with μ_D. The energy diagram clearly indicates that the bias at the crossing point represents the condition where $|e|V_{SD} = \mu_D - \mu_S = \mu_{N+2} - \mu_{N+1}$. From Eq.(4.8), we can infer that $\mu_{N+2} - \mu_{N+1} = E_C + \delta E$. Therefore, we find that

$$|eV_{SD}|_{crossingpoint} = E_C + \delta E. \tag{4.32}$$

Thus, we can infer the charge addition energy of a device from the maximum V_{SD} of the blockaded region. In general, the energy of the source-drain voltage at which two dI/dV_{SD} lines with slopes of opposite signs intersect on a conductance map corresponds to the energy difference between the two molecular states involved. The energy of $|eV_{SD}|_{crossingpoint}$ could be the energy difference between two charge states as described above, or between the ground and excited levels of the molecule.

From Eq.(4.32) and Eq.(4.31), we find that the gate efficiency factor $\frac{C_G}{C}$ allows us to convert between the magnitude of the gate voltage and the actual energy modulation of the discrete levels such that

$$|e|V_{SD} = |e|\frac{C}{C_G}V_G. \tag{4.33}$$

We will explore this relationship further in our discussion of the Kondo effect in chapters 8 and 9.

4.8 One Electronic and One vibrational Level Case

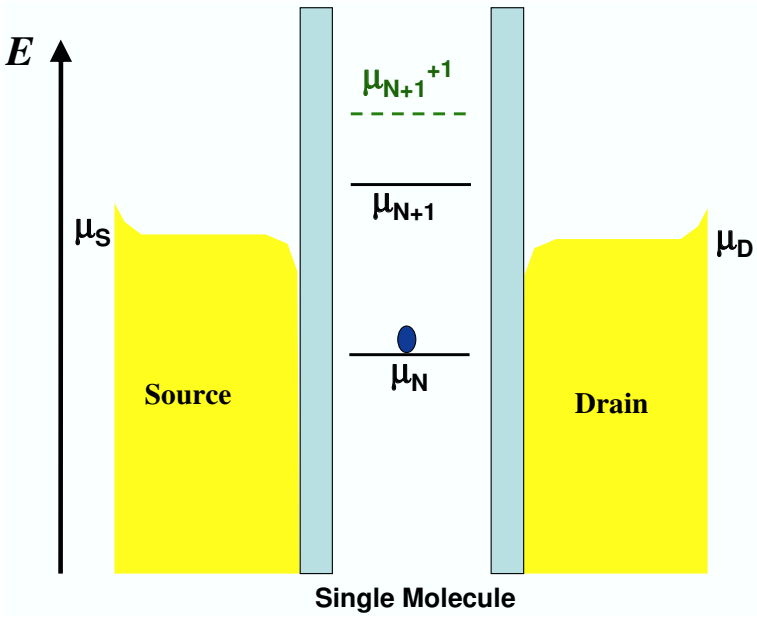

Figure 4.11 : Energy diagram of a SMT with one molecular level and an exciation level.

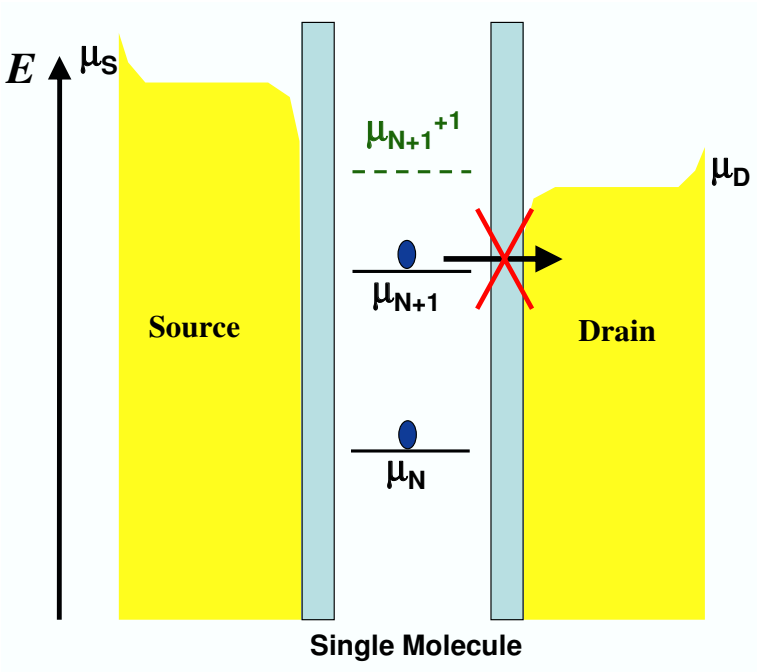

Figure 4.12 : Energy diagram of a SMT with one molecular level and an exciation level that cannot sustain current flow within the assumptions of the squential tunneling model.

We saw that electron transport through multiple electronic levels leads to Coulomb diamonds on the conductance map. Let us now see the ramifications of electron transport through vibrational excited levels of electronic states. Figure 4.11 is an energy diagram of a SMT where only one electronic level on the molecule is available for tunneling namely, μ_{N+1}. Since μ_{N+1} can either be occupied or not, there are two possible occupation states, the N charge state and the $N+1$ charge state. Now, there is also one vibrational excited level associated with μ_{N+1}. The level μ_{N+1}^{+1} corresponds to a vibrational excited state of the $N+1$ electronic state.

We note that by including vibrational excitations in our discussion, we have taken

a small step beyond the system described by the Anderson Hamiltonian. However, most of the Coulomb blockade physics we have discussed thus far will still apply to this situation, and we can still use the rate equations to model the transport through the device. But we must be careful when we consider electronic transport through the excited level. For example, take the case depicted by Figure 4.12, where only μ_{N+1}^{+1} is located between the Fermi levels of the source, μ_S, and drain, μ_D, electrodes is an example of a situation that needs to be considered carefully. Although the energy levels configuration depicted in Figure 4.12 appears to be one that could sustain current flow through a SMT, this assertion actually is not true within the assumptions of the sequential tunneling model. This is because in this energy configuration, the most probable chain of events that would happen is that an electron hops onto μ_{N+1}^{+1}, then the electron decays to the $N+1$ ground state, μ_{N+1}. After the electron enters the $N+1$ ground state, no new electron can jump onto the molecule because such a transition would require energy equal to μ_{N+2}, which is above both μ_D and μ_S. The lack of current flow for the case where $|\mu_D| < |\mu_{N+1}^{+1}| < |\mu_S|$ means electronic transport in the blockade region will not be affected by direct tunneling through excited levels of the electronic states. We note that this argument assume the rate of electrons relaxation from the vibrational excited state of a molecule to its ground electronic state is faster than the rate of electrons tunneling on/off the molecule. This assumption is found to be consistent with our experimental results.

Let us now explore how the presence of an excited level influences transport

in the non-blockade region. We solve the rate equations for the case described in Figure 10. There are be three occupation probabilities P_0, P_1^g and P_1^e, where P_1^g and P_1^e are the probabilities for an additional electron to be in the ground and excited level of the $N+1$ electronic state, respectively. The calculations involve setting $\frac{dP_0}{dt} = \frac{dP_1^g}{dt} = \frac{dP_1^e}{dt} = 0$ and using $P_0 + P_1^g + P_1^e = 1$ to derive the steady state current, which is

$$\begin{aligned}\frac{I}{|e|} &= -P_0(\gamma_S^g f_S^g + \gamma_S^e f_S^e)P_1^g\gamma_S^g(1-f_S^g) + P_1^e\gamma_S^e(1-f_S^e) \\ &= \frac{\gamma_S^g\gamma_D^g(f_D^g - f_S^g)(\gamma_S^e(1-f_S^e)+\gamma_D^e(1-f_D^e)) + \gamma_S^e\gamma_D^e(f_D^e - f_S^e)(\gamma_S^g(1-f_S^g)+\gamma_D^g(1-f_D^g))}{(\gamma_S^g+\gamma_D^g)(\gamma_S^e+\gamma_D^e) - (\gamma_S^g f_S^g + \gamma_D^g f_D^g)(\gamma_S^e f_S^e + \gamma_D^e f_D^e)}.\end{aligned} \tag{4.34}$$

Here $(f_S^g, f_S^e, f_D^g, f_D^e)$ are the Fermi functions calculated at μ_{N+1} and μ_{N+1}^{+1} for the source and drain electrodes. Figure 4.13 is a conductance map that describes a SMT with two accessible charge states and one excited level associated with the higher charge state. The main difference between Figure 4.13 and Figure 4.9 is the presence of the lines which terminate at the points D and E and have the same slopes as the dI/dV_{SD} lines which denote the boundary of the Coulomb diamonds. As noted in our description of Figure 4.9, the boundary line which includes point $D(E)$ represents points in the $V_{SD} - V_G$ parameter space where μ_{N+1} is aligned with $\mu_S(\mu_D)$. Similarly we find that the line which terminates at point $D(E)$ denotes points in the $V_{SD} - V_G$ parameter space where μ_{N+1}^{+1} is aligned with $\mu_D(\mu_S)$. Therefore, as indicated by the energy diagrams, both $|eV_{SD}|_{pointD}$ and $|eV_{SD}|_{pointE}$ represent the energy difference between the excited and ground states of the $N+1$ electronic state (μ_{N+1}^{+1} - μ_{N+1}

). This is the excitation energy of the $N+1$ charge state. In general, when the N charge state has excited levels associated with it, the conductance map includes excited level dI/dV_{SD} lines that intersect the ground level boundary lines at $V_G < V_0$.

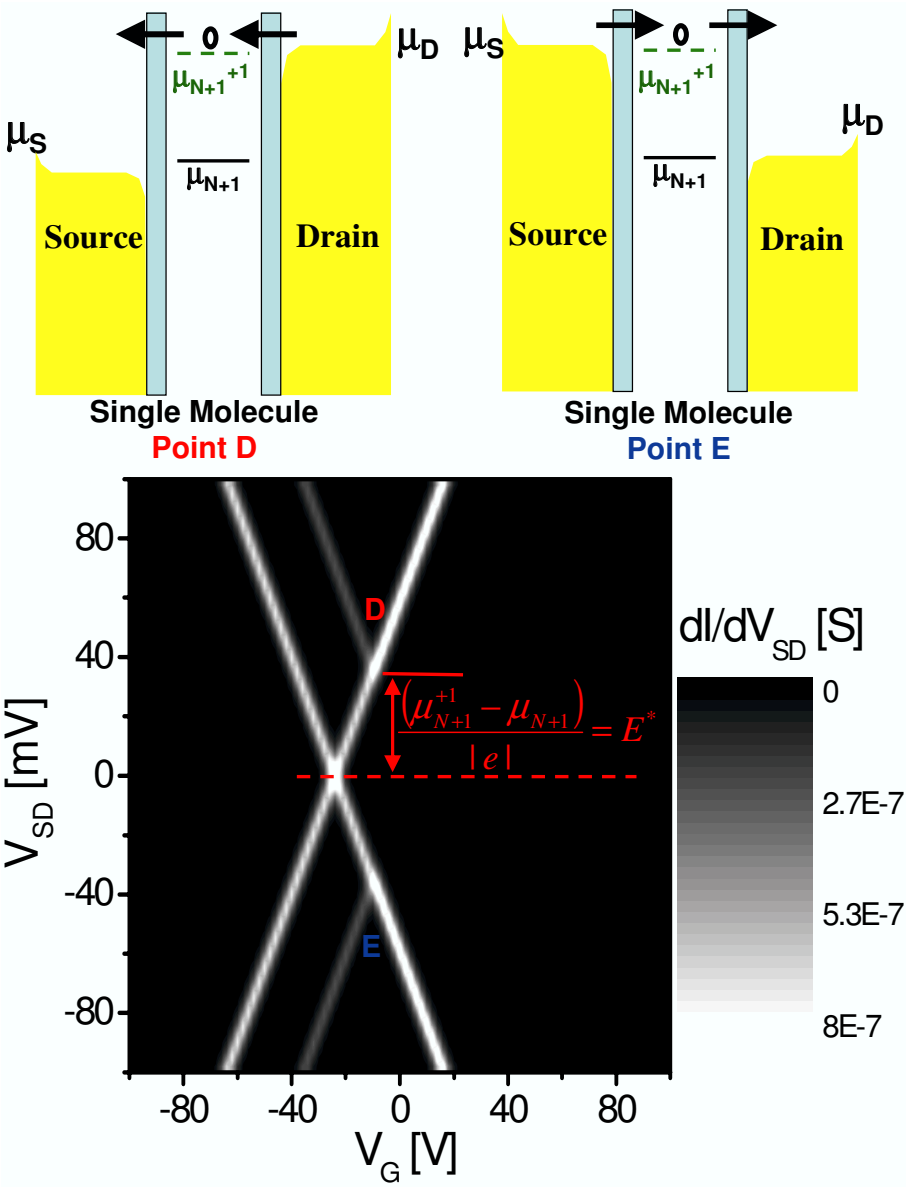

Figure 4.13 : Conductance map of a SMT with one molecular level and an exciation level. The energy diagrams describe direct tunneling through the excited level.

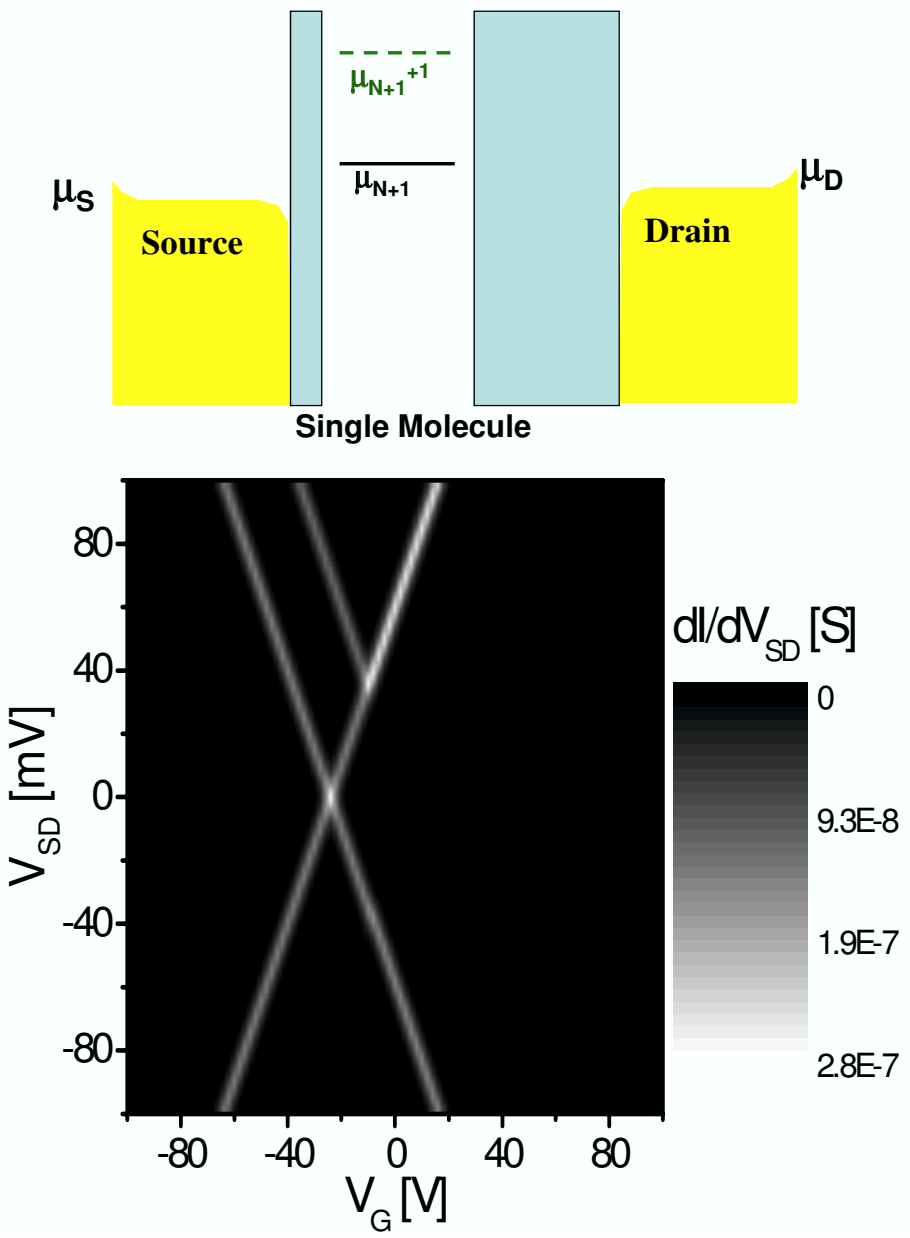

Figure 4.14 : Conductance map of a SMT with one molecular level and an exciation level, but the coupling of the molecule to the two electrodes are asymmetric.

On occasion, we observe an excited level dI/dV_{SD} line for only one bias direction in our experimental conductance map of a SMT. Such experimental results can be

explained by asymmetric coupling between the molecule and the source and drain electrodes (*i.e.* $\gamma_S^g >> \gamma_D^g$ and $\gamma_S^e >> \gamma_D^e$). Figure 4.14 is a conductance map which describe a SMT similar to that in Figure 4.11, but in this case we set $\frac{\gamma_S^g}{\gamma_D^g} = 10$, $\gamma_S^g = \gamma_S^e$, and $\gamma_D^g = \gamma_D^e$. The higher conductance excited dI/dV_{SD} line corresponds to the situation where the excited level is aligned to the Fermi level of the electrode with the smaller electron tunneling rate, since in this case the current amplitude increases more strongly due to the availability of the excited level. In the other situation, where the excited level is aligned to the Fermi level of the electrode with the larger electron tunneling rate, the current amplitude of the excited line is much weaker. In a device with asymmetric coupling the maximum current amplitude through the device is limited by the smaller tunneling rate.

Although thus far we have described the case where the excitations are vibrational in origin, the rate equation formalism used above can be applied equally to electronic excitations. When dealing with electronic excited states, the tunneling rates are related to the detailed shapes of the single-particle level wavefunction. In the case of vibrational excitation, the tunneling rates are associated with Franck-Condon-like factors. The Frank-Condon factor is related to the overlap between the starting vibrational wavefunction (before an electron is hopped on or off the molecule) and the vibrational wavefunction after the tunneling event [68].

We have used rate equations to model, the basic electronic transport characteristic of a SMT. At low temperature, the conductance map of a SMT with large charge

addition energy will exhibit Coulomb blockade behavior. We can measure the vibrational excitation energy spectrum of a SMT by observing the intersection voltages of the excited and ground level dI/dV_{SD} lines in the conductance map. We distinguish excitation features originate from electronic and vibrational modes in the transport characteristics of our SMTs by noting that vibrational features usually have energy less than 50 meV and that vibrational excitation features are observable in both charge states.

4.9 Summary

Our model makes several simplifying assumptions. We have assumed that the rate of electron relaxation from excited states to the ground state of the molecule is fast compared to the tunneling rate. Non-equilibrium transport behavior can be observed if electrons can tunnel on and off the molecule before the electrons are allowed to relax to their ground state [39]. Another assumption we made in our model is that all electronic transport in the SMT involves sequential tunnelings describable by rate equations. We have neglected higher order tunneling processes such as cotunneling [33] . Cotunneling is a second order tunneling process where electrons tunnel through the molecule via virtual intermediate states that are classically inaccessible by energy conservation. Cotunneling processes have been studied both experimentally and theoretically [34–38] in various systems, and in chapters 6 and 7 we will describe them in a SMT system. Finally, we have so far ignored the effects of spin in our

simple model of the SMT. Spin will play a critical role in our discussion of the Kondo effect in chapters 8 and 9.

Chapter 5

Coulomb Blockade in Single Molecule Transistors

We have fabricated single molecule transistors by electromigration using C_{60} [23] and transition metal coordination complexes [25]. These SMTs function as single-electron transistors [33,59], with conduction dominated by Coulomb blockade effects. Figures 5.1 and 5.2 shows two of our conductance maps, one from a C_{60}-based SMT and the other from a Co-TMCC-based SMT. These SMTs are made by the fabrication process described in chapter 2. These structures are made on SiO_2 insulating layers on top of degenerately p^+ doped silicon substrates. Indium contacts to the silicon substrates serve as contacts with the gate electrodes, which are used to modulate the electrostatic potential of the molecules. All electrical measurements are performed in a variable temperature vacuum probe station using an HP 4145B semiconductor parameter analyzer at cryogenic temperatures. The overall structure of the conductance data can be understood using the sequential tunneling model of Coulomb blockade physics described in chapter 4.

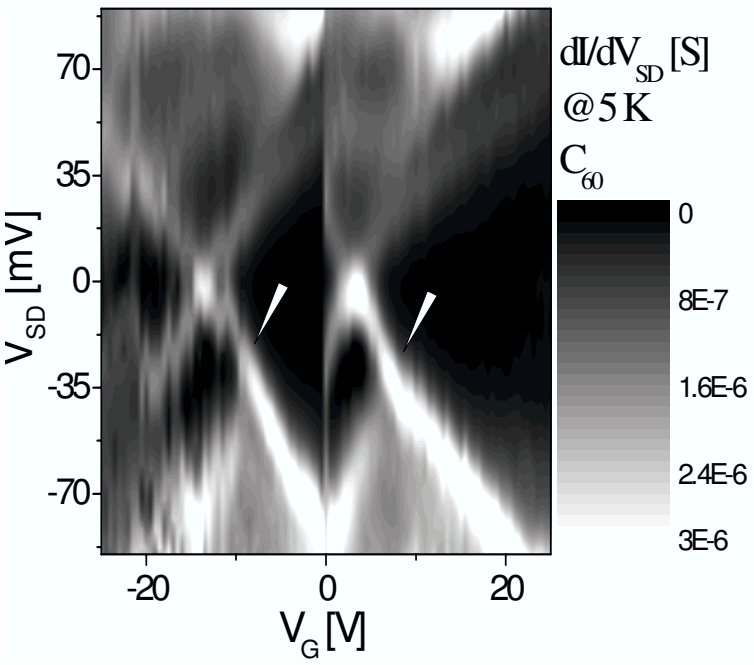

Figure 5.1 : Conductance maps from C60-based SMT [23]. The white arrows show the vibrational feature in the non-blockaded region of the map.

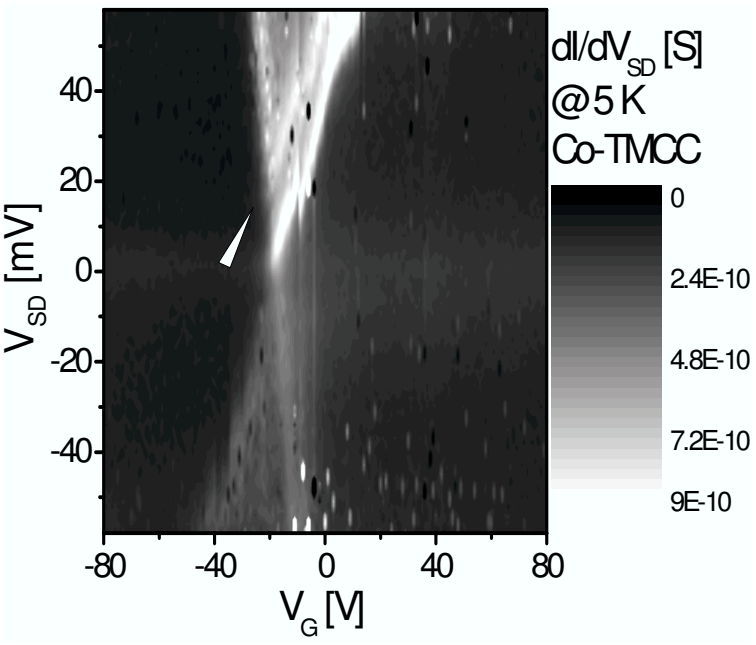

Figure 5.2 : Conductance maps from Co-TMCC-based SMT. The white arrow shows the vibrational feature in the non-blockaded region of the map.

We have described the basic physics and the expected transport characteristics of SMTs in chapter 4. From Eq.(4.32), we know that the charge addition energy may be estimated from the maximum V_{SD} of the blockaded region. However, due to the low gate coupling of our devices and the restricted bias range we use to minimize the chance of current-induced irreversible changes, we cannot extract the full value of the charge addition energies of our devices. We can infer from their conductance maps that the E_a of the two devices shown in Figs. 5.1 and 5.2 significantly exceeds 100 meV.

At a certain value of gate voltage called the charge degeneracy point, it becomes energetically degenerate for the charge of the molecule to change by one electron.

At the charge degeneracy point, the conductance gap vanishes at zero bias, and as V_G is increased through a degeneracy point, the average number of electrons on the molecule is increased by one. Fig. 5.1 shows two nominal degeneracy points from one device; this is an example of offset charge instability. Since any change in the local charge environment of the molecule acts like an effective gate potential, the uncontrolled switching of charged defects or charge traps can leads to effective shifts in V_G. Therefore, the two degeneracy points of Fig. 5.1 are actually the same point, and the Coulomb blockade features are simply duplicates. Because of uncertainty about the local charge environment, it is generally not possible to infer directly which molecular charge state corresponds to a particular charge state in an SMT. However, based on electrochemical studies, one can narrow down the possibilities. For example, the left charge state in Fig. 5.1 is most likely either C_{60} or C_{60}^{-} [49], and the left charge state in Fig. 5.2 is most likely Co(III).

In Chapter 4, we showed that the sequential tunneling model can be extended to include quantized excitations of the molecule. These conductance peaks appear when excited levels of the molecules become energetically accessible. The energies of these levels can be determined from the bias voltages at which the conductance peak lines intercept the Coulomb diamond. Among all the SMTs that exhibit conductance peak lines outside the conductance gap only a small number of excitation energies are regularly observed. This reproducibility of excitation features among many different devices of a single molecular species leads us to believe that these conductance peak

lines represent excitations levels intrinsic to the molecules. The excitation features are indicated by white arrows in Figs. 5.1 and 5.2.

The magnitudes of these excitation energies help us identify these conductance peak lines as vibrational features. The energy magnitudes of these excitations are generally too small to be related to the electronic levels of nanometer-scale molecules. The fact that these features are present irrespective of the charge state of the molecules also suggests that these features are vibrational in origin. Finally, some of the energy magnitudes of the excitation features match known vibrational modes of the molecule. For example, the prominent 35 meV resonance in Fig. 5.1 is similar in energy to a Raman-active vibrational mode of C_{60}, corresponding to the C_{60} sphere deforming to and from a prolate ellipsoid [69].

Previous investigations of C_{60}-based SMT by Park *et.al.* [27] have reported excitations of both a molecule-surface binding oscillation ($\sim$ 5 meV) and a cage deformation mode ($\sim$ 35 meV). One reason that the 5 meV vibrational features are absent in our C_{60}-based SMTs may be due to the differences between our electromigration breaking techniques and Park *et.al.*'s. We use a two-step technique where electromigration breaking occurs at both room and cryogenic temperatures. We found our two-step technique allows us to make smaller inter-electrode gap devices consistently. Our devices tend to have better molecule-electrode couplings than Park *et.al.*'s devices, as inferred from comparison between typical conductance levels of our devices. The general differences in nano-scale morphologies could explain differences in observable

vibrational modes in our devices. This could also help explain why we were able to observe the Kondo effect in our C_{60}-based SMTs (see chapter 9), while Park *et.al.* initially did not.

In Figure 4.13, we depict a theoretical conductance map that describes a SMT with two accessible charge states and one excited level associated with the higher charge state, calculated by rate equations. Disregarding the offset charge instability in Fig. 5.1, the transport behaviors in the two plots are fairly similar. Much of the noise in the data is an artifact of the numerical differentiation procedure. The overall background conductance of the experimental plot is higher than the theoretical map, but this may be attributed to direct tunneling through the source-drain gap and higher-order tunneling through the molecule (see chapter 6). Part of the reason for the wider features in our experimental map may be because we have neglected the effect of electron relaxation in our theoretical model.

Finally, I note that each molecule in a molecular device is likely to have a different capacitive coupling to the source, drain, and gate electrodes due to the geometrical and chemical variation in the local environment. The fact that the conductance maps of most of the devices we label as SMTs have only one set of slopes for their Coulomb diamond boundaries shows that these devices are truly single molecule based.

Chapter 6

The Cotunneling Theory

Higher order tunneling processes are called cotunneling because they involve the simultaneous tunneling of two or more electrons [33]. We will continue to ignore spin in our present discussion until we get to the Kondo effect. Our sequential tunneling model predicts that at low temperature, $k_BT << E_C$, the conduction through the SMT is exponentially suppressed in the blockade regime. However, the inclusion of the cotunneling processes could lead to much enhanced conduction in the blockade regime. A cotunneling event which leaves the molecule in an excited level is called inelastic, but otherwise cotunneling is elastic.

In elastic cotunneling an electron virtually hops from one lead to an energy level on the molecule that is classically inaccessible, and in the same quantum process, an electron from the same classically inaccessible level on the molecule hops off to the other lead. Figure 6.1a,b shows two such processes schematically. Elastic cotunneling is analogous to the superexchange mechanism in chemical electron transfer theory. [70–73]. Elastic cotunneling leaves the energy of the tunneling electron and the molecule unchanged. Thus, this process can occur at arbitrarily low V_{SD}. This cotunneling process is essentially temperature and V_{SD} independent as long as $|eV_{SD}|, k_BT << E_a$. In short molecules, both cotunneling and direct tunneling as described in eq.(4.1) can occur, and the two processes can quantum mechanically

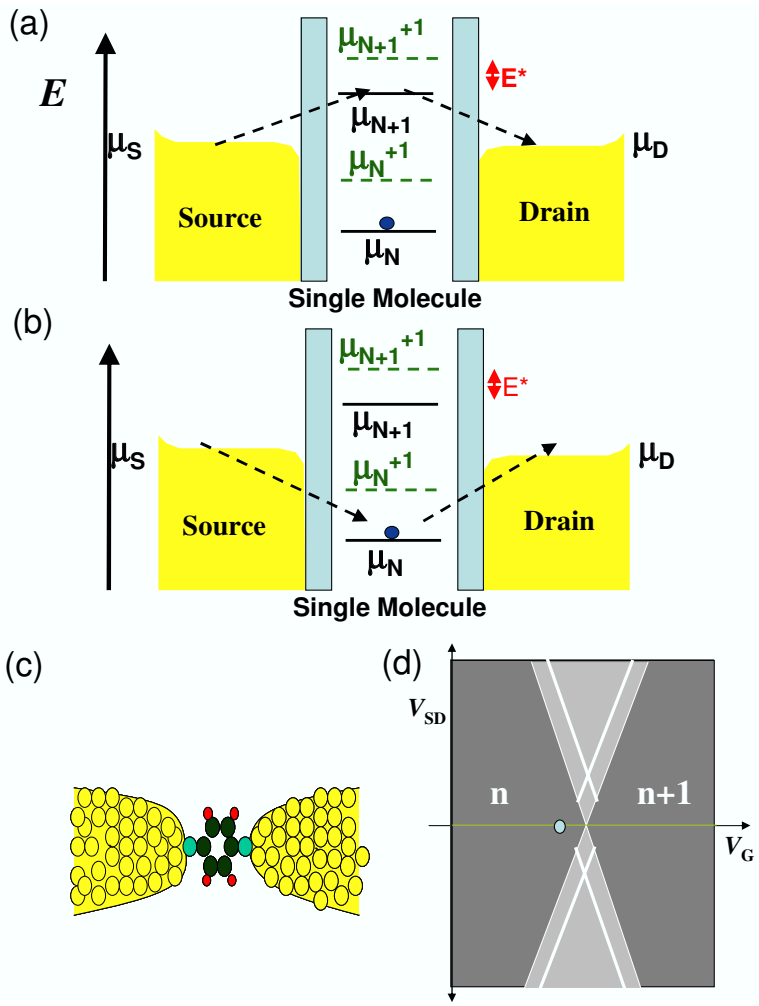

Figure 6.1 : Energy diagrams of the elastic cotunneling processes. (a) elastic cotunneling involving electrons. (b) elastic cotunneling involving holes. (c) the vibrational modes of the molecule is unexcited in the elastic cotunneling process. (d) the overall background conductance of a SMT increases uniformly due to elastic cotunneling.

interfere with each other.

Experimentally, in the blockade regime of many of our conductance maps, we observe uniform, nonzero background conductance. It is difficult to resolve the origin of the background conductance (whether it is due to direct or co-tunneling) since no detailed geometric information about the junctions is accessible. However, since we have unambiguously observed inelastic cotunneling in our devices, it is highly likely that elastic cotunneling is responsible for at least some of this background conductance.

In inelastic cotunneling an electron virtually hops from one lead to an energy level on the molecule that is classically inaccessible, and in the same quantum process, an electron from a second, lower energy, classically inaccessible level on the molecule hop out to the other lead. Figure 6.2a,b shows two such processes schematically. Despite the sequential way we have described both the elastic and inelastic cotunneling, we should keep in mind that in the cotunneling mechanism, the events of electron tunneling from one of the leads into the dot and tunneling from the dot to the other lead occur as a single quantum process. In the inelastic cotunneling process the energy of the tunneling electron is changed and the molecule is left in an excited state by the process.

We can estimate the electron tunneling rate of an inelastic cotunneling process, γ_{in}, by noting that the uncertainty relation allows an electron to spend a finite amount of time in a classically inaccessible state [33]. We can approximate this time

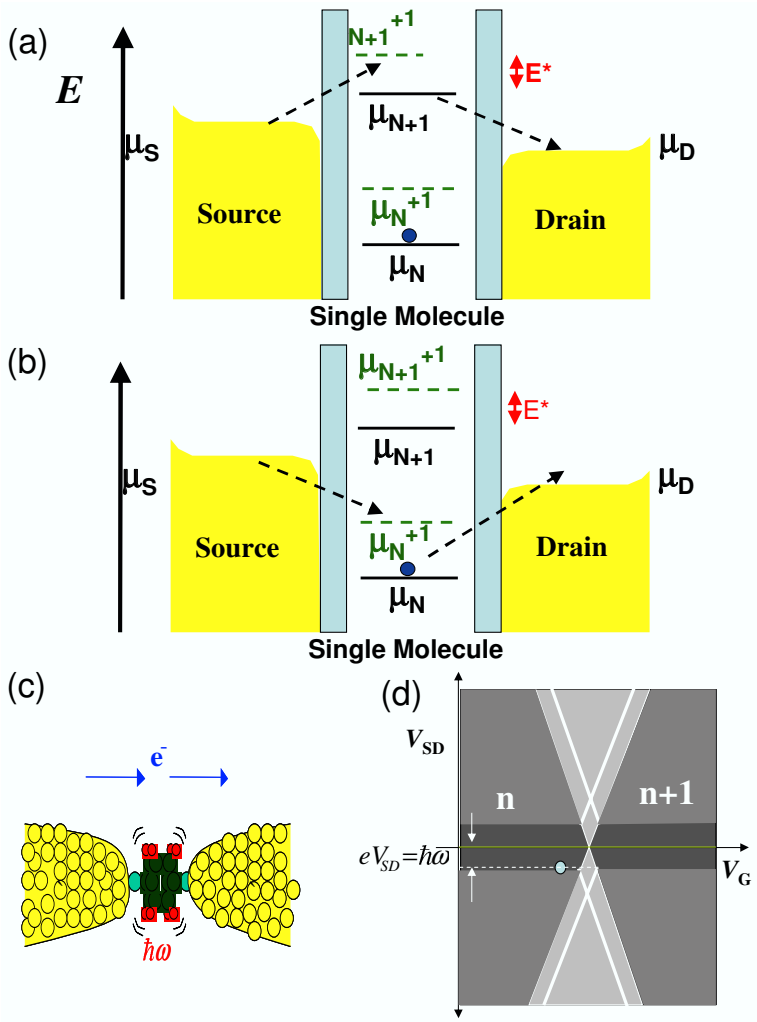

Figure 6.2 : Energy diagrams of the inelastic cotunneling processes. (a) inelastic cotunneling involving electrons. (b) inelastic cotunneling involving holes. (c) the vibrational modes of the molecule is excited in the inelastic cotunneling process. (d) the conductance of a SMT increases uniformly above the bias voltage whose energy is equal to the vibrational energy of the mode excited due to inelastic cotunneling.

as h/E_C. Therefore, the inelastic tunneling rate can be estimated as

$$\gamma_{in} \sim \frac{\gamma_S \gamma_D}{E_C}, \tag{6.1}$$

and in the case of symmetric coupling,$\gamma_S = \gamma_D$,

$$\gamma_{in} \sim \gamma_S \frac{R_K}{R_{contact}}. \tag{6.2}$$

Recall from eq.(4.10) that one of the conditions for the energy levels of the molecule to be quantized is that $R_{contact} >> R_K$, so the inelastic cotunneling rate is much smaller than the sequential electron tunneling rate.

Unlike elastic cotunneling, which can be observed at vanishing V_{SD}, inelastic cotunneling can be observed only at finite biases (see Figs. 6.1d) For a SMT with an internal excitation energy E^* ($|\mu_{N+1}^{+1} - \mu_{N+1}|$ as defined in our Coulomb blockade discussion is an example of E^*. The value of E^* would be different for different electronic levels.), the onset of the inelastic cotunneling process happens at a threshold voltage $|V_{SD}| = \frac{E^*}{|e|}$. The opening of the inelastic cotunneling channel results in a change in slope of the $I - V_{SD}$ curve of the SMT in the blockade regime. This corresponds to a step in differential conductance of the device as $|V_{SD}|$ passes through the threshold voltage, and this threshold voltage is readily identifiable as the bias position where a peak appears in a plot d^2I/dV_{SD}^2 as a function of V_{SD}. The width of the inelastic cotunneling peak may be thermally broadened. Although we call this kind of cotunneling inelastic, the total electron energy in this process is actually conserved [33]. The energy the electrons uses to excite the vibrational mode of the molecule is given by the bias drop, eV_{SD}.

The energy of the threshold voltage is related to the energy of the real excited state described in Fig. 4.13 as follows. At the edge of the Coulomb diamond, if inelastic cotunneling is the only significant conduction process in the blockade region, then the onset of the inelastic cotunneling process should occurs at the same V_{SD} as the onset of the first-order excited level dI/dV_{SD} line in the non-blockade region. In semiconductor dot experiments [37, 38], the inelastic cotunneling step in the conductance is observed to intersect the excited state tunneling resonance at the boundary of the Coulomb diamond. Experimental evidence suggests that the inelastic cotunneling processes observes in SMT are related to the vibrational excitation of the molecule.

Chapter 7

Single Molecule Inelastic Electron Tunneling Spectroscopy

In chapter 5, we reported experimental transport characteristics from our SMTs that correspond to sequential tunneling through vibrational excited levels of the molecules (*e.g.* 35 meV for C_{60}). We also observed evidences of cotunneling. In both chapters 5 and 6, I have commented that although we can attribute part of the uniform background conductance we observed in our experimental conductance maps to elastic cotunneling, we do not know enough about the nanometer-scale structure of our SMTs to quantitatively analyze the effect. However, by looking at the derivative of our conductance maps (d^2I/dV_{SD}^2 as a function of V_{SD} and V_G), we can identify transport features related to inelastic cotunneling processes in our SMTs, and we can correlate specific d^2I/dV_{SD}^2 features with vibrational excitations of the molecules, as determined by Raman and infrared spectroscopy. Tuning electronic levels (changing V_G) near the charge degeneracy point reveals shifts in line shapes and peak positions of these inelastic cotunneling features, suggesting significantly modified electron-vibrational coupling in this region.

Non-resonant tunneling of electrons through molecules by inelastically exciting vibrational modes has been observed since the 1960s and is the basis for inelastic electron tunneling spectroscopy (IETS). Such processes were first developed to study

the vibration spectrum of organic molecules buried in large area tunneling junctions [74–76]. In conventional IETS, as $|eV_{SD}|$ exceeds the energy necessary to excite a vibrational mode of the molecules trapped in the tunneling barrier, a new inelastic channel opend for electronic tunneling, which results in a step in the dI/dV vs V_{SD} plot, and a peak in a d^2I/dV_{SD}^2 vs V_{SD} plot. One usually looks at the d^2I/dV_{SD}^2 as a function of V_{SD} because in such plots the IETS features are more discernable.

Recently, IETS has been refined to probe small groups ($\sim$ thousands) of molecules via crossed wires [40, 77, 78] and nanopores [41], and single molecules using STM [17, 79–82] . IETS of single nanometer-scale molecules in a three-terminal geometry, in which a gate electrode allows in situ adjustment of the energy levels, has been reported by only our group to date [25].

We found that the Co-TMCC-based SMTs to have the highest propensity for expressing IETS features in their transport data among the different types of SMTs we tested. We believe this behavior has to do with the differences in the vibrational mode couplings between the different molecules and the metallic electrodes, Therefore, we will concentrate our discussion of single molecule IETS on experimental results from the Co-TMCC-based SMTs.

At various temperatures, we measured the current I as a function of V_{SD} and V_G from -100 to $+100$ V using a semiconductor parameter analyzer. We computed dI/dV_{SD} and d^2I/dV_{SD}^2 as a function of V_{SD} and V_G by numerical differentiation. Direct comparison between second derivatives obtained via the numerical differen-

tiation method and the second harmonic lock-in method finds excellent agreement. Because numerical differentiation can introduce artifacts into the resulting derivatives, we are careful to identify genuine features in d^2I/dV_{SD}^2 by comparing multiple data sets taken at the same or nearly the same gate voltage.

We have examined 407 Co-TMCC deposited electrode pairs, and we found 27 devices that clearly display a single degeneracy point in their conductance maps. The majority of these devices also show a resonance at zero V_{SD} in one charge state identified as a Kondo resonance. The Kondo effect manifests itself in transport data of SMTs as enhanced conductance at zero V_{SD} when there is a magnetic moment on the molecule. We will discuss the Kondo effect and the coupling between the vibrational modes and the Kondo effect in chapter 8 and 9. The charge addition energy in these devices typically exceeds 100 meV, but the inelastic modes occur at relatively low energies ($\sim$ 10's of meV), implying that the modes being excited are unlikely to be electronic. Control devices with electrodes exposed only to THF never display IETS or Kondo physics.

In 12 out of the 27 devices, the conductance in the classically blockaded region and/or outside the Kondo resonance is large enough to allow clean measurements of d^2I/dV_{SD}^2 . Figure 7.1 shows the derivative of the conductance maps of two such devices at 5 K. Far from the edges of the Coulomb diamonds, there are prominent features within the blockade or Kondo regimes that we have indicated with black arrows. There are some asymmetries in the line shapes of these d^2I/dV_{SD}^2 peak fea-

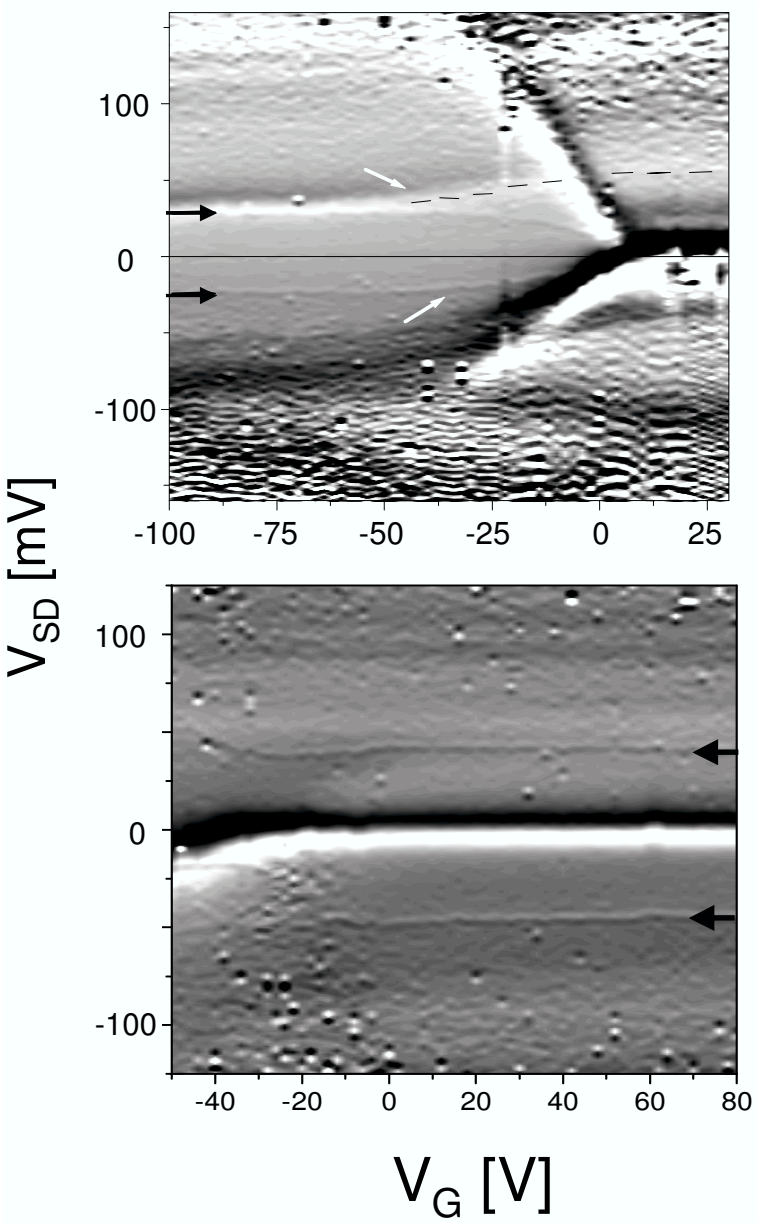

Figure 7.1 : Derivative of the Conductance maps of two Co-TMCC SMTs [25]. The brightness scales of the top and bottom maps are -8 x 10^{-5} A/V^2 (black) to 3 x 10^{-5} A/V^2 (white), and -2 x 10^{-5} A/V^2 (black) to 2 x 10^{-5} A/V^2 (white), respectively. The zero-bias features correspond to Kondo peaks in dI/dV_{SD}. Prominent inelastic features are indicated by black arrows. In both devices, when the inelastic features approach the boundaries of the Coulomb blockade region, these levels shift and alter line shape (white arrows). Black dash line in left map traces an inelastic feature across the Coulomb blockade region boundary and into the Kondo regime.

tures. These asymmetries may arise from coherent interference between the inelastic cotunneling process and other processes, such as direct tunneling [83] or higher-order tunneling effects like the virtual emission and re-adsorption of a vibrational quantum [84, 85]. This kind of interference is similar to the Fano effect seen in other spectroscopic measurements [86, 87], in which resonances are not simple peaks, but can look like dips or derivatives of peaks, depending on the relative phases between the complex amplitudes of the various completing processes.

We also observe that far from the degeneracy point, the d^2I/dV_{SD}^2 features often appear as pairs of opposite sign in V_{SD}. For example, in the bottom map of Figure 7.1, there is one peak feature at $\sim$ 45 meV and another peak feature at $\sim$ -48 meV. Ideally, these two features should be exactly symmetrically located around zero source-drain bias since they represent the excitation of the same vibrational mode. But the fact that they are not precisely symmetric can be explained by asymmetric tunnel coupling and capacitance between the molecule and the electrodes in this device. The fact that the Kondo resonance maximum conductance at 5 K is $< 2e^2/h$ (the peak conductance of this device $\sim 0.2e^2/h$) is an indication that the coupling is asymmetric [88] (see chapter 8 and 9).

The d^2I/dV_{SD}^2 features in the blockaded region of our devices occur at essentially constant values of V_{SD} until V_G is varied such that the features approach the edge of the Coulomb diamond. The changes in these features as the charge state of the molecule varies indicate that the inelastic processes are native to the SMT itself,

and not due to some parallel conduction channel. In the top map of Figure 7.1, the negative source-drain bias feature denoted by a white arrow approaches zero V_{SD} as the gate voltage is tuned toward the degenerate point, while the positive source-drain bias feature denoted by another white arrow shifts to higher energies as the charge state of the molecule is changed. This shifting of vibrational mode energies can be understood as a consequence of molecular distortion due to the change of redox state. When an electron hops on or off from a molecule it could change the shape of the molecule in certain directions, and the vibrational modes with displacements along those directions would change their energies as a result of the transition. In other words, a neutral molecule and the charged version of the molecule will probably have different vibrational spectra and shapes. By following the evolution of vibration levels across a charge transition we see that the mechanical properties of individual molecules can be tuned electronically in a SMT.

We also note that the line shapes of the features marked by the white arrows change at the V_G near the edge of the blockade region. This observation is consistent with the fact that the gate electrode shifts the energy of the vibrational level through which the inelastic process proceeds. This alteration changes the amplitude of the inelastic process relative to other processes. This is similar to the argument we used to explain why there are some asymmetries in the line shapes of the d^2I/dV_{SD}^2 peak features far from the degeneracy point above, but in this situation we can tune the relative amplitudes of the different tunneling processes by varying the gate voltage.

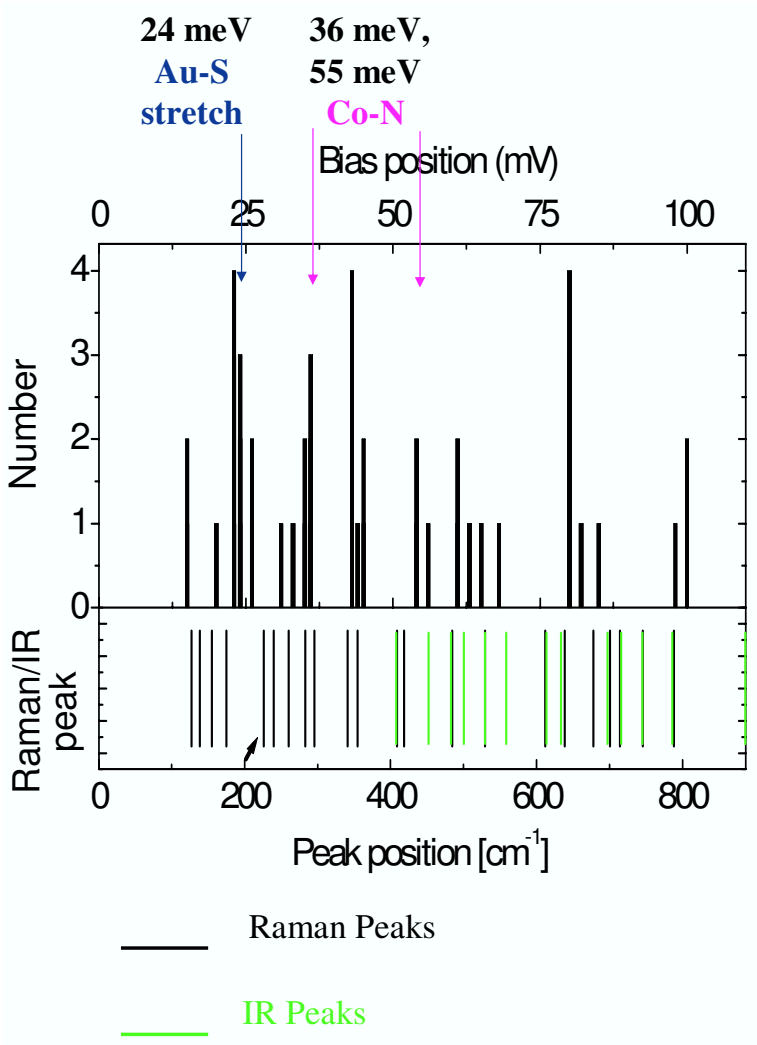

Figure 7.2 : Histogram of the IETS features compare with Raman and IR features [25]. (top) Histogram of $|V_{SD}|$ positions of 43 features in d^2I/dV_{SD}^2 that are persistent at constant V_{SD} over at least 10 V gate voltage range, for the 12 samples discussed. Bin size is 1 meV. Width of actual features is at least 5 meV, with position indicating feature center. Blue and purple arrows indicate tentative peak assignments. (bottom) Raman (black) and IR (green) peak positions taken of Co-TMCC in the solid state at room temperature. The indicated Raman peak near 28 meV is only present in films of Co-TMCC self-assembled on Au electrodes.

We examined the d^2I/dV_{SD}^2 vs V_{SD} data from all 12 of our devices that show clear IETS features that remained at fixed V_{SD} as V_G is varied. We identified a total of 43 candidate inelastic features at $V_{SD} < 120mV$, ranging in apparent width from 5 to 20 mV at ~ 5 K. The narrowest inelastic features broaden visibly as the temperature is elevated above 20 K. Figure 7.2 shows a histogram (bin size = 1 mV) of the V_{SD} positions of the features identified from detailed examination of the d^2I/dV_{SD}^2 vs V_{SD} data. The lower panel of the figure shows Raman (Stokes) peak position (data taken on a powder of as-synthesized Co-TMCC) and IR absorption peak positions (data taken on powder of as-synthesized Co-TMCC pressed into pellet form, blended with KBr). The correlations between the spectra and inelastic features in d^2I/dV_{SD}^2 strongly support that vibrational inelastic cotunneling processes are at work in these molecular transistors.

The fact that different SMTs exhibit different subsets of IETS features is a natural consequence of the sensitivity of IETS to the nanoscale structure of the molecular junction. The electron-vibrational coupling between the vibrational modes of the molecule and the electrodes is strongly dependent on the alignment of the molecule in the junction [89]. First-principles calculations have demonstrated that the alteration of a single chemical bond between the molecule and the electrodes can completely alter the relative intensity of the different vibrational modes contributions to the inelastic electron tunneling spectrum of a molecular device [90].

Comparison with the Raman spectra of the as-synthesized Co-TMCC and related

compounds (*e.g.* ligands without the Co^{2+} and ligands without the SCN) suggest tentative peak assignments for the IETS features. The peaks near 36 and 55 meV are likely the Co-N stretch [91] , while that near 44 meV is tentatively a -SCN deformation [91] (implying that not every S is bonded to a Au surface atom, consistent with x-ray photoemission data of the compound [25]). The 24 meV peak is tentatively the Au-S bond [92]; this claim is further supported by the appearance of a $\sim$ 28 meV Raman peak on monolayers of Co-TMCC self-assembled on Au electrodes, while such a peak is absent in Raman spectra of both the as-synthesized Co-TMCC and bare electrodes.

To summarize, we have examined inelastic features in the transport properties of single molecule transistors. In the inelastic cotunneling regime, these devices allow the acquisition of inelastic tunneling spectroscopy data as a function of gate voltage. While each device may only show a few inelastic features, a histogram of this data correlates well with IR and Raman spectra of the molecule in question. The added tunability of SMTs permits the examination of vibronic processes as a function of the energetic of the electronic levels, an experiment performed first by our group.

Chapter 8

The Kondo Theory

Before we talk about what happens when we include the effects of spin in our discussions of SMTs, I would like to discuss the effect of dilute magnetic moments in bulk metallic systems. The two topics are related in that they both lead to the Kondo effect. Although the Kondo effect was observed in bulk metallic system back in the 1930s [93] and explained in the 1960s [42] , definitive signatures of the Kondo effect in the single-electron system were not observed until 1998 [61, 63].

Let us start by recalling the Drude model for bulk metallic conduction [94]. In this model the resistivity of a metal is directly related to the temperature of the system until low temperatures. As the temperature decreases there are fewer and lower energy phonons to scatter with the conduction electrons. Thus the resistivity is decreased. At low temperature the resistivity saturates because the imperfections and intrinsic impurities of the crystalline lattice of a real metal limit the mean free path of conduction electrons at all temperatures. There is actually a T^5 temperature dependence on the resistivity at very low temperature due to the remaining electron-phonon scattering, but we will ignore this minor effect.

In our discussion of the mechanism of the Kondo effect, we will use a handwaving approach. The Kondo effect is a many-body process that should really be treated as a crossover phenomenon with the renormalization group approach. The language of

"bond" I employ in the discussion should be taken as a cartoon for experimentalist. Now let us imagine adding a dilute amount of atoms with unpaired electrons into a bulk metallic system. The new atoms will try to decrease their kinetic energy by forming bonds with the conduction electrons [95–97]. In these bonds the electrons from the new atoms will be localized, but the conduction electrons will start out delocalized, so for the bond to form the conduction electrons must expend some energy to become somewhat "localized". Therefore, in order for the bond to form, the energy cost of "localizing" the conduction electron must be less than the reduction of kinetic energy due to the formation of the bond. In a metallic system this typically happens at temperature less then tens of Kelvins.

In a normal metallic system when a conduction electron passes close to an ordinary impurity, there is a finite probability that the conduction electron will interact with the impurity and scatter to a different direction. But if the impurity in question is one of the atoms with unpaired electrons and that the system is at low enough temperature that a bond could begin to form, then the probability for the conduction electron to be scattered will increase with decreasing temperature, thus the resistivity will increase with decreasing temperature [93] . Finally, when the system is at a very low temperature, every electron passing near an impurity with unpaired electrons will participate in the forming of a bond before being scattered. The situation is called the unitarity limit and at temperatures below that limit, the resistivity will stop rising and saturates at a level higher than that for a normal metallic system [95].

This increasing and saturating of resistivity along with other anomalous thermodynamics phenomena at low temperature of a metallic system with dilute magnetic impurities are collectively called the Kondo effect [93,98–101] . I note that my above description of the Kondo effect which is intended as a simple introduction is very qualitative, but I will try to be more quantitative in my discussion of the Kondo effect in SMTs.

Now let us see how we get the Kondo effect by including spin in our discussion of the SMT. Unless otherwise stated, in our discussion of the Kondo effect, whenever we refer to the conductance of a SMT, we mean the equilibrium conductance of the SMT. Experimentally, the equilibrium conductance is the differential conductance measured when only a small bias is applied across the SMT in order to define a direction of current flow (usually < 1 mV). From our previous description of Coulomb blockade in SMT, we note that at low temperature, a SMT with $R_{contact} >> R_K$ and $\Gamma << k_B T, e^2/C + \delta E$ can hold a fixed, integer number of electrons and that the number of electrons on the molecule can be changed one at a time by manipulation of V_{SD} and/or V_G. In ignoring spin in our previous discussion, we have implied that a single localized state on the molecule can hold either zero or one electrons (with no magnetic moment). However, since electrons have spin, each localized state on the molecule should be able to hold zero, one (with magnetic moment), or two electrons. In the case of two electron occupancy the electrons should be of opposite spin. Here we will also make the assumption that the localized states have

Kramers degeneracy, meaning the localized states are spin degenerate. The inclusion of spin does not change the physics of Coulomb blockade in SMT we discussed in the previous sections. Although a molecular state can hold two electrons, it will still cost an amount of energy equal to the charging energy to add the second electron to the molecule.

A SMT is actually very similar to a metallic system with one isolated impurity atom. The electrons in the electrodes are akin to the conduction electrons in a metallic system and the electrons on the molecule are similar to the electrons in an impurity atom. When we change the number of electrons on the molecule one at a time in a SMT, it is similar to when we change the impurity atom in a metallic environment from one that is non-magnetic (analogous to having paired electrons on the molecule) to one that is magnetic (analogous to having unpaired electrons on the molecule). However, the analogy is not exact in that most electrons transporting through a SMT must pass through the molecule, whereas this is not true in the metallic system case. I will address the consequences of this difference of geometry later, but for now let us see how we can get the Kondo effect from an isolated magnetic atom in a metallic environment and a SMT.

We know from our discussion of Coulomb blockade physics that we can change the charge state of the molecule by one on a SMT be changing the V_G applied across the device. This means that a SMT can be made to have a magnetic moment on its molecule, similar to a system with an isolated magnetic atom in a metallic

environment, simply be manipulation of the gate voltage.

We can understand the behavior of a SMT as well as an isolated magnetic atom in a metallic environment by looking at the Anderson Hamiltonian first introduced in Equation(4.2). We have previously stated that the Anderson Hamiltonian contains four terms which describe: 1) the conduction electrons of the electrodes, 2) the localized electrons on the impurity, 3) the Coulomb interaction between the electrons, and 4) the mixing between the conduction electrons and the localized electrons. As stated above, by including spin in our consideration, a single localized state on the impurity could have occupancy of zero, one, or two electrons (with Kramers degeneracy).

In order for us to understand how having a magnetic moment on the molecule of a SMT affects the transport behavior of the SMT, we need to understand, within the context of the Anderson Hamiltonian, the nature of the interaction between a localized electron and the conduction electrons. We can approach this problem by trying to solve the Anderson Hamiltonian, but we do not need to solve the full Anderson Hamiltonian to get the answer we want. The Anderson Hamiltonian is actually more complicated than we need. For the case of an isolated magnetic atom in a metallic environment as well as the case of a SMT, there is only one single level on the impurity atom (molecule) that is relevant to the Kondo physics, and that is the level that gives the system a magnetic moment. In a SMT, when its molecule contains no magnetic moment, its transport characteristic would be consistent with

the Coulomb blockade physics we described in the previous sections.

To treat the "simplification" of the Anderson Hamiltonian rigorously we will need to perform a Schrieffer-Wolff canonical transformation [102] on the Anderson Hamiltonian in the limit of weak hybridization ($t << U, |\varepsilon|$), where ε is the energetic separation between the molecular level and the chemical potential of the source and drain. U is the Coulomb repulsion energy defined in Eq.(4.4) (its value is equal to $2E_C$, the charging energy.), and t is the tunneling amplitude whose relationship with Γ, the coupling strength, is given by Eq.(4.12). Figure 8.1 shows the various energetic parameters in the context of the energy diagram of a SMT. The imposition of the weak hybridization limit ensures that the fluctuation of charge on and off the impurity level is negligible. The use of the transformation basically allows us to treat the final term of the Anderson Hamiltonian, the term dealing with the coupling between the conduction electrons and the localized electrons, for the specific situation where there is a magnetic moment on a single impurity state. The result of the transformation is that the final term of the Anderson Hamiltonian is changed to

$$\begin{aligned} H_{ex} &= -\sum_{kk'} J_{k'k}(\Psi_{k'}^{+}\mathbf{S}\Psi_k) \bullet (\Psi_d^{+}\mathbf{S}\Psi_d) \\ \text{, with } \Psi_k &= \begin{pmatrix} c_{k\uparrow} \\ \\ c_{k\downarrow} \end{pmatrix} \quad \text{and } \Psi_d = \begin{pmatrix} d_{\uparrow} \\ \\ d_{\downarrow} \end{pmatrix}, \end{aligned} \tag{8.1}$$

where $2\mathbf{S} = \sigma$ are the Pauli matrices, and $J_{k'k}$ is called the anti-ferromagnetic exchange integral. In the limit where $k \sim k' \sim k_F$, the Fermi wavelength, Eq.(8.1) is

reduced to

$$H_{s-d} = -J(\mathbf{s} \bullet \mathbf{S}), \tag{8.2}$$

where the anti-ferromagnetic exchange integral is given as

$$J \sim \frac{-t^2}{U}, \tag{8.3}$$

s represents the spin of the conduction electron, and **S** represents the impurity spin. This effective Hamiltonian for the coupling between conduction and localized electrons where the localized state contains an unpaired spin is called the s-d model. The transformation demonstrates that the coupling between the local moment and the conduction electrons is anti-ferromagnetic because the exchange integral is negative.

Without going into the details of the Schrieffer-Wolff canonical transformation, I can give a handwaving argument for why the interaction between the localized moment on the impurity level and the moments of the conduction electrons should be anti-ferromagnetic [103]. By stating that their interaction is anti-ferromagnetic we mean that the conduction electrons surrounding the impurity state prefer to have their spins aligned antiparallel to that of the localized electron. Let us imagine a spin up electron is localized in an impurity state. This unpaired electron could use up an amount of energy on the order of $\frac{t^2}{U}$ by virtually hopping to and back from an unoccupied spin up state at the Fermi surface of the electrode. The availabillity of an unoccupied spin up state at the Fermi surface of the electrode implies that the conduction electron at the Fermi surface near the impurity state is spin down. But due to the Pauli Exclusion Principle the spin up electron in the impurity state

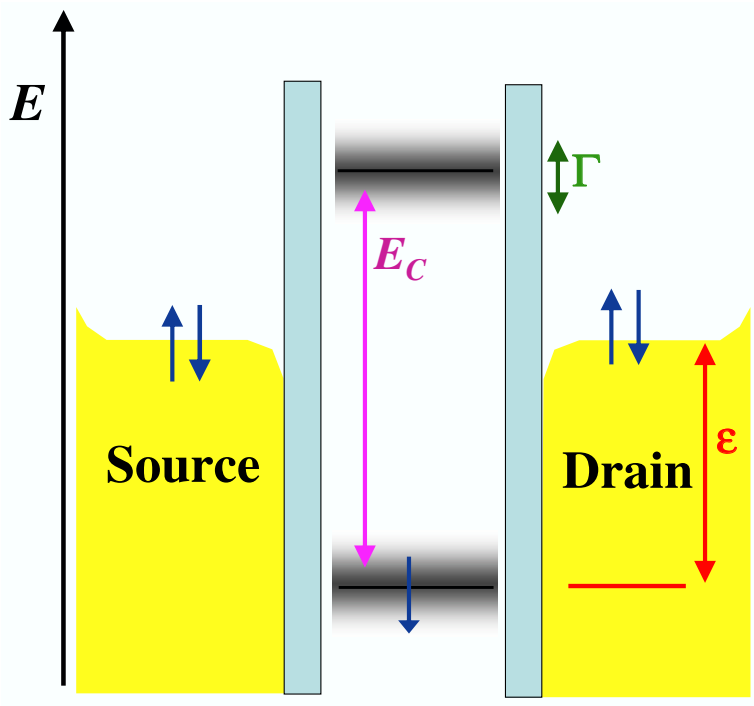

Figure 8.1 : Energy diagram showing the relevant energetic parameters of the Kondo effect in SMT.

would not be able to lower its energy by virtual hopping if the conduction electron at the Fermi surface is spin up as well. Therefore, it is more energetically favorable for the conduction electrons near an impurity state to have spin opposite that of the unpaired electron in the impurity state.

Because of the anti-ferromagnetic coupling between the magnetic moment on the impurity atom and the conduction electrons, the ground state of the system should be a spin singlet state. Conduction electrons surrounding the impurity atom will try to screen the spin of the impurity through spin-flip interactions. A cartoon version of the interaction goes something like this: A conduction electron comes near the local moment and interacts with it, such that the local moment is flipped and the spin of the conduction electron itself is flipped. After this two things can happen: 1) After some time, the original conduction electron interacts again with the local moment, and this gives the conduction electron a finite lifetime. 2) A second conduction electron interacts with the flipped local moment, thus the first and second conduction electrons interact indirectly via the local moment. It is because of the indirect interaction between conduction electrons that the Kondo effect is a many-body effect.

At very low temperature, the conduction electrons and the local moment will form a spin-singlet bond to minimize the energy of the system, and this is what was termed the unitarity limit in our initial discussion of the Kondo effect in a bulk metallic system. If we are talking about bonding in an atomic system, like two

hydrogen atoms, we would expect the binding energy of the spin-singlet to simply be J, but since the Kondo effect is a many-body effect, the characteristic energy (an analogue of the binding energy) for this bond is given by the Kondo temperature, T_K [65].

Although the characteristic energy of this spin-singlet bond is T_K, the Kondo effect actually becomes evident at temperatures above T_K. In the case of an isolated magnetic atom (or a dilute amount of magnetic atoms) in a metallic environment, the presence of the local moment leads to a logarithmic increase in resistivity with decreasing temperature at temperature above T_K. For the case of SMT, due to the difference in system geometry as stated earlier, the Kondo effect manifests itself as an increase in conductance with decreasing temperature of the system. We can understand this exchange of parameters by noting that in a bulk metallic system the impurities acts as impediment for the flow of conduction electrons, whereas in a SMT, the conduction electrons must go through the molecule to carry current through the device. The formation of the spin-singlet in the bulk system leads to increased scattering of the conduction electrons, thus the increase in resistivity, but in a SMT, the bond creates a new channel for the conduction electrons to flow through the device, thus the increase in conductance [93] . A signature of the Kondo effect in a SMT is that whenever there is a local moment on the molecule, a resonant state appears at the density-of-states of the Fermi levels of the electrodes [88, 93, 104]. At $T << T_K$ the width of this Kondo resonance is on the order of $k_B T_K$ [62, 64]

(see Fig. 8.2). Raising the temperature would attenuate the strength of the Kondo resonance.

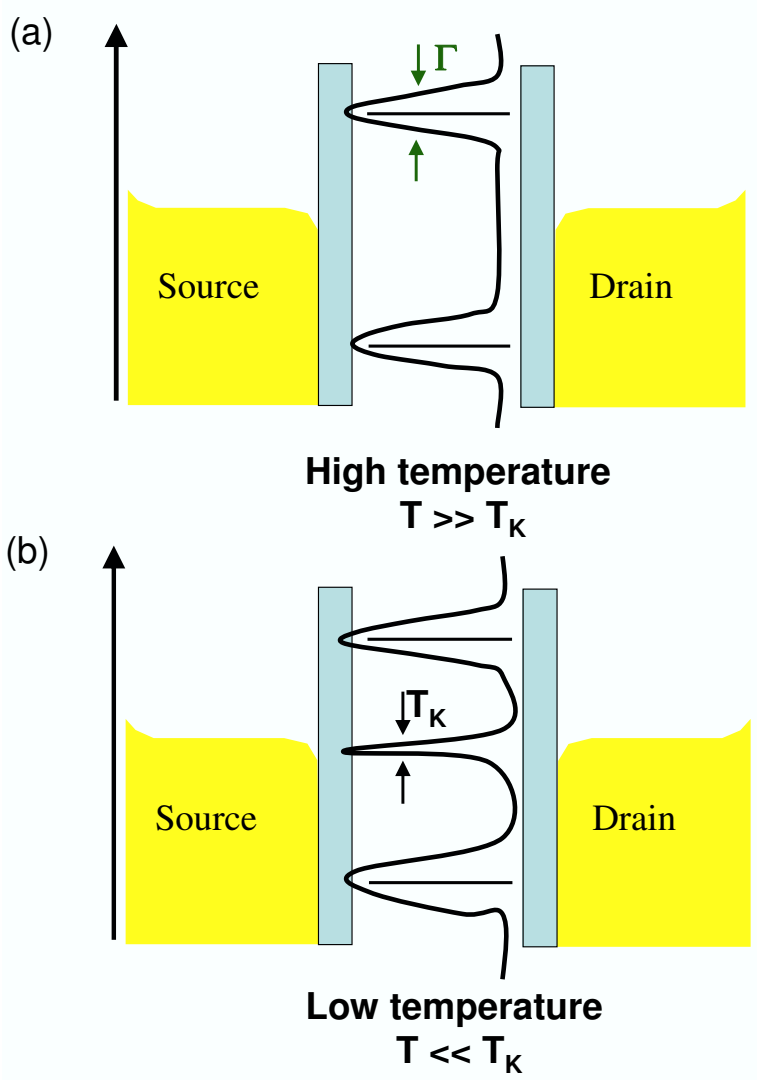

Figure 8.2 : Energy diagram showing the density of states of a SMT with an unpaired spin at (a) T >> T_K and (b) T << T_K.

Now that we have a derived the Hamiltonian relevant to the Kondo problem, we should be able to calculate the transport behavior of a system under the influ-

ence of the Kondo effect. However, these calculations proved to be quite difficult. The original 1964 calculation of Kondo (the person for whom this effect named) was perturbative. It reproduced the experimentally observed logarithmic behavior of resistivity at temperature above T_K, but it predicted a divergent resistivity at zero temperature [93]. The problem is that to get the full physics from Kondo effect, we cannot treat it perturbatively. It is hard to rigorously define the level of difficulty for an impurity to "capture" a conduction electron, and be able to quantitatively define how well formed is a "bond" between an impurity electron and the conduction electrons, especially when the "bond" is a many-body state. Much theoretical progress was made in the 1970's and 1980's in understanding the low temperature behavior of a Kondo system [95–97] . However, a quantitatively way to calculate the bonding strength of the singlet state, and the effect of the singlet formation over the entire temperature range, thus the temperature dependence of the resistivity, were not fully developed until 1994 by Costi and Hewson using the renormalization group approach [95, 105].

These theoretical treatments resulted in predictions with regards to the transport behavior of a system influenced by the Kondo effect that are impossible to test experimentally in a system consisting of dilute magnetic moments in a bulk metallic environment. However, some of these predictions could be readily tested in SMTs. Figure 8.1 shows the energetic of the Kondo problem in a SMT. All relevant parameters were defined previously, but to summarize they are: Γ , the molecular level

width; ε , the energetic separation between the molecular level of interest and the equilibrium chemical potential of the source and drain; and E_C, the charging energy due to on-site Coulomb repulsion. This model assumes that only one molecular level is relevant for observing the Kondo effect, but since experimentally most SMTs have $E_C \sim 1$ eV this should be a valid assumption.

A SMT with a magnetic moment on its molecule can be in one of three regimes of the Anderson model, parameterized by ε/Γ. They are: the empty orbital regime ($\varepsilon/\Gamma < 0$), in which case there can be no Kondo resonance; the mixed valence regime ($\varepsilon/\Gamma \lesssim 1$), in which case both spin and charge fluctuations are relevant; and the Kondo regime ($\varepsilon/\Gamma > 1$), in this case only spin fluctuations are significant (see Fig 8.3). The Kondo regime is well described by the s-d model. We are primarily interested in the transport behavior of SMTs in the Kondo regime.

Using scaling theory it was predicted that in the Kondo regime, the Kondo temperature is given by [106]

$$k_B T_K = \frac{\sqrt{E_C \Gamma}}{2} \exp(-\frac{\pi\varepsilon(-\varepsilon + E_C)}{\Gamma E_C}). \tag{8.4}$$

A cursory look at Eq.(8.4) reveals to us that $k_B T_K$ will always be smaller than Γ . Experimentally, we want T_K to be large so that we could observe the Kondo resonance, at easily accessible temperatures ($T > 4.2$ K). This mean a large Γ is desirable experimentally. If T_K were much lower than the temperature at which the experiments on the SMTs are performed, then it would be difficult to test the theoretical predictions of the Kondo effect. However, if a SMT had $\Gamma \gtrsim E_C, \delta E$,

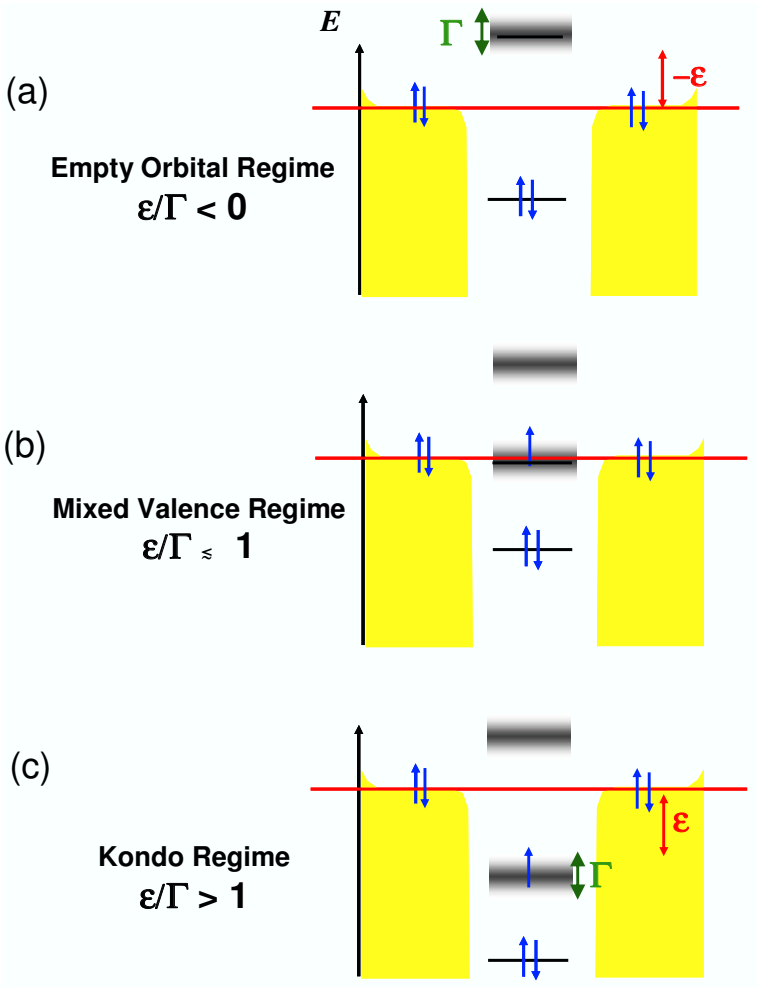

Figure 8.3 : Energy diagram showing the different regimes. (a) The empty orbital regime (b) The mixed valence regime (c) The Kondo Regime.

then the quantization of charge and energy of its molecule levels would be lost. In a SMT the strength of Γ is presumed to be primarily related to the chemical bonding and the geometry between the molecule and the electrodes.

We also note that Eq.(8.4) predicts that the $log(T_K)$ is parabolic with a minimum at $\varepsilon = \frac{E_C}{2}$. This behavior has been observed in semiconductor quantum dot experiments [63,64]. In the simple model described in Figure 8.1, we define $\varepsilon = 0$ at the degeneracy point V_{0S} where the molecular level is singly occupied. As described in our discussion of Coulomb blockade, we can vary the value of ε by changing the gate voltage V_G applied to the SMT. Using Eq.(4.33) we can convert the change in V_G to the value of ε by the relationship

$$\varepsilon = |e|\frac{C_G}{C}\delta V_G. \tag{8.5}$$

The magnitude of δV_G is equal to $|V_G - V_{0S}|$, but its sign is determined by the charge state of the molecule. By measuring the T_K of our SMTs as a function of V_G, we can test the validity of Eq.(8.4), a prediction that is impossible to test in the bulk metallic system.

For the SMT system, we can apply an arbitrary bias voltage V_{SD} across the device and measure the conductance as a function of V_{SD}. Such an experiment allows us to probe the non-equilibrium physics behind the Kondo effect. While one can apply a bias voltage across a bulk metallic system, such experiment would not be very informative since only a small proportion of the bias voltage will be applied across any individual impurity. In general one expects the conductance of a SMT in

the Kondo regime to decrease as the magnitude of the bias voltage applied across the device increases. To explain this phenomenon I will need to explore how the application of bias affects the Kondo resonance.

As stated earlier, one manifestation of the formation of the singlet bond is the Kondo resonance, which is an enhanced density of states at the Fermi levels of the electrodes. The unpaired electron in the molecule couples to the conduction electrons in both electrodes to form the Kondo resonance. When the bias voltage is zero, there is one resonance connecting both electrodes, and the equilibrium conductance of the device is enhanced. Using the Keldysh formalism, Wingreen and Meir [88] found that when a bias voltage is applied across a SMT, the Kondo resonance is split into two resonances of the density of states at the Fermi level of the each electrode, and that the amplitudes of these split peaks are suppressed compared to the equilibrium peak (see Fig. 8.4). The reason for the suppression is that the transfer of electrons from the higher energy Fermi level to the lower energy Fermi level is dissipative.

As a result of the splitting and suppression of the Kondo resonance in non-equilibrium, the conductance of a SMT in the Kondo regime decreases with increasing bias voltage amplitude. In fact, one of the most experimentally accessible signatures of the Kondo effect in a SMT is the Kondo peak in the differential conductance around zero bias. Although the final saturation of the Kondo resonance (the unitary limit) occurs at temperatures below the Kondo temperature, the Kondo peak in the differential conductance first appears at temperatures above T_K. This is because

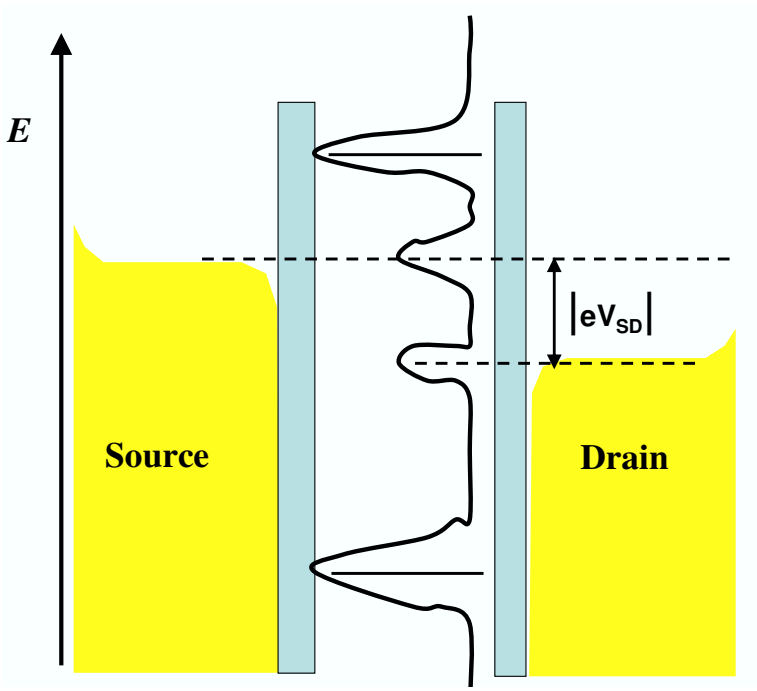

Figure 8.4 : Energy diagram of a SMT in the Kondo regime out of equilibrium. The density of states resonance due to the Kondo effect is split and diminished by the applied source-drain bias.

$k_B T_K$ is only the characteristic energy of the singlet; the Kondo bond actually begins to form at temperatures above T_K. For $T_K < T < 10T_K$, the equilibrium conductance of a SMT is roughly logarithmic in T [65]. The shape of the Kondo peak in the differential conductance versus V_{SD} is expected to be a Lorenztian [88] . At $T << T_K$, the full width at half maximum (FWHM) of the Kondo resonance in $G(V_{SD})$ is expected to scale with T_K, such that

$$FWHM \sim \frac{2k_B T_K}{|e|} \tag{8.6}$$

[62, 64].

For a symmetrically coupled SMT ($\Gamma_S = \Gamma_D$), in the unitary limit, its maximum equilibrium conductance is $G_0 = \frac{2e^2}{h}$, the conductance quantum. For the case of asymmetrical coupling, the maximum equilibrium conductance is reduced by the asymmetry factor

$$F_A = \frac{4\Gamma_S \Gamma_D}{\Gamma_S + \Gamma_D} \tag{8.7}$$

[88, 107, 108]. Eq.(8.7) demonstrate that in the case of asymmetric coupling, it is possible to have a high Kondo temperature while still having a low total conductance, because the conductance through a device in the Kondo regime is limited by the smaller of Γ_D and Γ_S, while Eq.(8.4) shows that T_K is set by their total. Figure 8.5 shows a differential conductance map of a generic SMT, indicating features from all the conductance mechanisms discussed so far in this thesis. The Kondo resonance is shown as the zero-bias peak in the right hand charge state. By Eq.(8.4) ,(8.5) and (8.6), one would expect the width of the Kondo resonance to vary as a function of

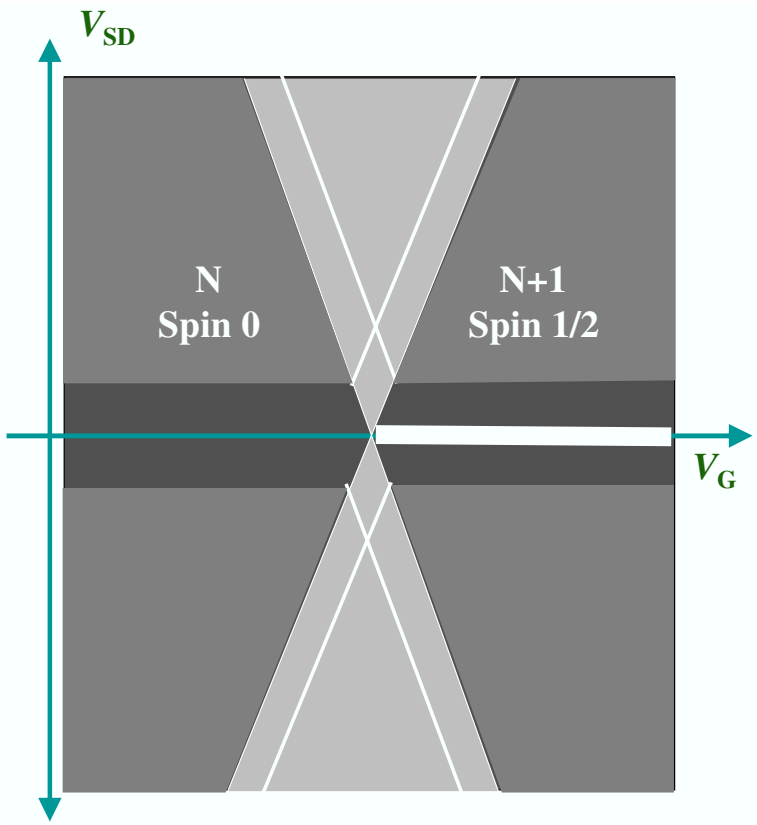

Figure 8.5 : A Cartoon conductance map of a generic SMT, indicating features from all the conductance mechanisms discussed so far in this thesis, including the Kondo effect.

V_G, such that $log(FWHM)$ is parabolic in V_G.

There are two main methods of inferring the Kondo temperature of a SMT from its conductance data. One method is to use eq(8.6), with which T_K is inferred from the FWHM of $G(V_{SD})$, and the other is to look at the equilibrium conductance as a function of temperature. Analytic results of $G(T)$ could be derived for the $T > T_K$ limit [101] by perturbation method and the $T << T_K$ limit [65]by the renormalization group method. However, the crossover regime has only numerical results derived from the numerical renormalization group method [105]. Fortunately,

there is a semi-empirical expression derived by Goldhaber-Gordon for a system where the localized state on the impurity is of spin-1/2. This expression has been proven to provide a good fit to the numerical renormalization group result for the Kondo and the mixed-valence regimes, giving the correct Kondo temperature in each case [105]. The semi-empirical expression is:

$$\frac{G(T)}{G_C} \approx (1 + 2^{(\frac{1}{s}-1)}\frac{T^2}{T_K^2})^{-s}. \tag{8.8}$$

For a spin-1/2 system, the parameter $s \sim 0.22$, and G_C is the maximum conductance, usually the inferred conductance at the unitary limit. There are significant complications that can arise when the localized state on the impurity is more than spin-1/2, and Eq.(8.8) would no longer be valid.

Chapter 9

Kondo Physics in Single Molecule Transistors

9.1 C_{60}-Based Single Molecule Transistors

In this section, we report measurements on C_{60}-based SMTs consistent with the signatures of the Kondo effect. Devices incorporating molecules with a metal ion [28, 29] have been shown to exhibit the Kondo effect in their conduction properties. The Kondo temperatures of our devices inferred from transport data can exceed 100 K, significantly higher than previously reported values in single electron devices. The data also suggest that signatures of inelastic vibrational processes can persist well into the Kondo regime, evidence of coupling between a vibrational excitation and the coherent many-body state.

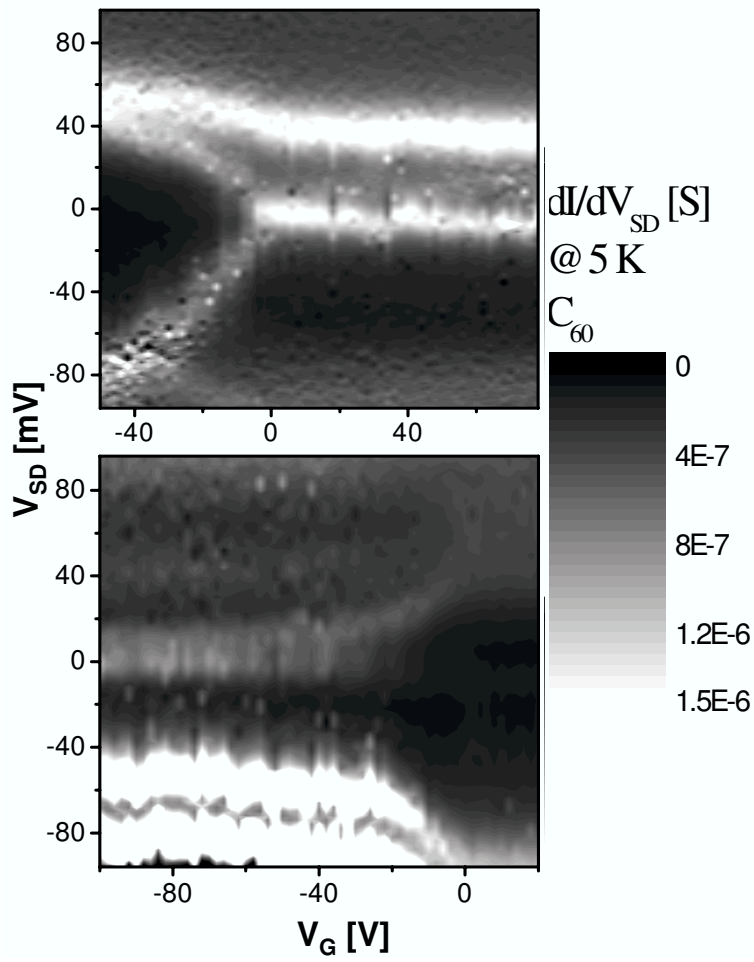

Figure 9.1 : Conductance maps from C60-based SMTs exibiting the Kondo effect [23]. The Kondo effect is manifested as the appearance of a zero bias conductance peak in one molecular charge state. Note the presence of $\sim$ 35 meV sidebands persisting into Kondo regime.

Of the 475 electrode pairs decorated with C_{60} and fabricated with the electromigration technique, five exhibit data like that shown in Figure 9.1 at 5 K. Since only about 15% of the starting electrodes are gateable, this translates to $\sim$ 7% of gateable devices show the Kondo resonance. The transitional behavior from Coulomb blockade to zero bias resonance when the number of electrons on the molecule is changed

to odd is consistent with the Kondo effect in a SMT as we described in chapter 8. Although zero bias resonances are occasionally seen in control samples, those features are always gate independent. The low proportion of C_{60}-decorated electrodes which yield Kondo-like conductance maps is a consequence of the exponential dependence of the Kondo temperature T_K on the intrinsic level width of the molecular levels , which itself is exponentially sensitive to the chemical bonding and the geometry between the molecule and the electrodes (see eq.(8.4)).

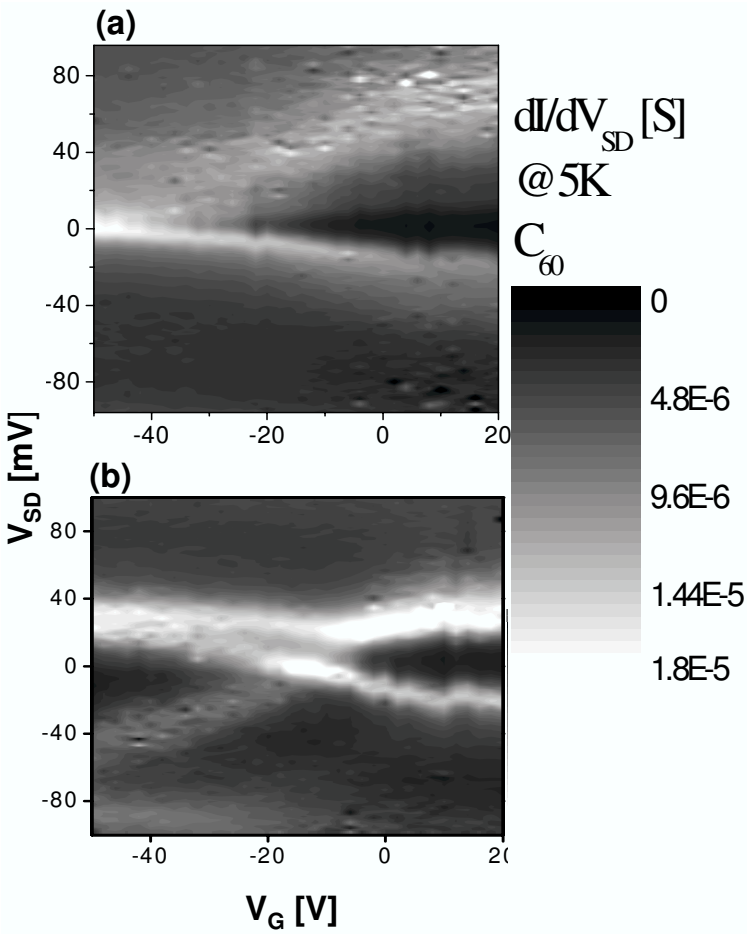

Figure 9.2 : An example of an irreversible change in these SMTs [24] a) shows Kondo at low temperature b) shows only Coulomb blockade after warming device.

Figure 9.2 demonstrate an experimental consequence of this strong dependence of T_K on Γ. Fig. 9.2a shows the conductance map of a device exhibiting the transition from Coulomb blockade to a zero-bias Kondo resonance. During an attempt to characterize the temperature dependence of the zero-bias peak, the device spontaneously changed to a different configuration. Subsequent measurements of the device yielded the conductance map shown in Fig. 9.2b. The transport characteristics of Fig. 9.2b

are consistent with a device with poor gate coupling showing Coulomb blockade physics. Despite this change in transport behavior, the maximum conductance of the device remained $\sim 10^{-5}$ S, consistent with our understanding of the relationship between Γ and the transport behavior of a SMT.

In describing a SMT, Γ is defined as the sum of the level widths due to the couplings Γ_S and Γ_D of the localized molecular state to the source and drain. While the maximum conductance of a SMT is limited by the smaller of two couplings, Γ_S and Γ_D (see eq.(4.27)), the Kondo temperature depends on their sum $\Gamma = \Gamma_S + \Gamma_D$ (see eq.(8.4)). The maximum conductance of the device described in Fig. 9.2a in the Kondo regime is $\sim 0.1(2e^2/h)$. Using eq.(8.7) this means the coupling of the molecule to one of the electrodes is more than twice as strong as to the other. The presence of the Kondo resonance in Fig. 9.2a demonstrates that despite the asymmetry, the sum of the couplings to the two electrodes is relatively high. When the temperature of the system increases, the C_{60} molecule that was responsible for the Kondo transport behavior on the device can move. In the case of this device, the C_{60} movement results in lowering the total coupling ,Γ, thus exponentially lowering T_K. However, the movement of the C_{60} maintains the relative value of the smaller of the two couplings, thus explaining the similar maximum conductance observe in the device both before and after the conformational change.

The Kondo temperature of a SMT can be inferred in two different ways. First, assuming spin-1/2, at fixed gate voltage the zero bias conductance G may be mon-

itored as a function of temperature and fit with the eq.(8.8). However, due to the instability of the molecule-metal configuration in C_{60}-based SMTs, we found it challenging to perform the characterization of these devices over a broad temperature range. From the limited temperature dependence data we were able to acquire from our C_{60}-based Kondo devices, we found their G(T) to be nearly constant, decreasing only slightly from 5 K up to 30 K. This is consistent with large Kondo temperatures, $T_K > 100K$, though the data do not put an upper bound on T_K.

The second method to infer T_K from transport data is to use eq.(8.6), which describes how we can extract T_K from the width of the Kondo resonance peak when the temperature is sufficiently below T_K. Figure 9.3a shows the differential conductance as a function of source-drain bias for a fixed gate voltage of a C_{60}-based SMT in the Kondo regime at two different temperatures. The zero-bias peak in conductance is well fit by a Lorenztian as expected for a pure Kondo resonance. The Kondo resonance peak of this device at 5 K has a $FWHM$ that is consistent with a device that has $T_K > 100K$.

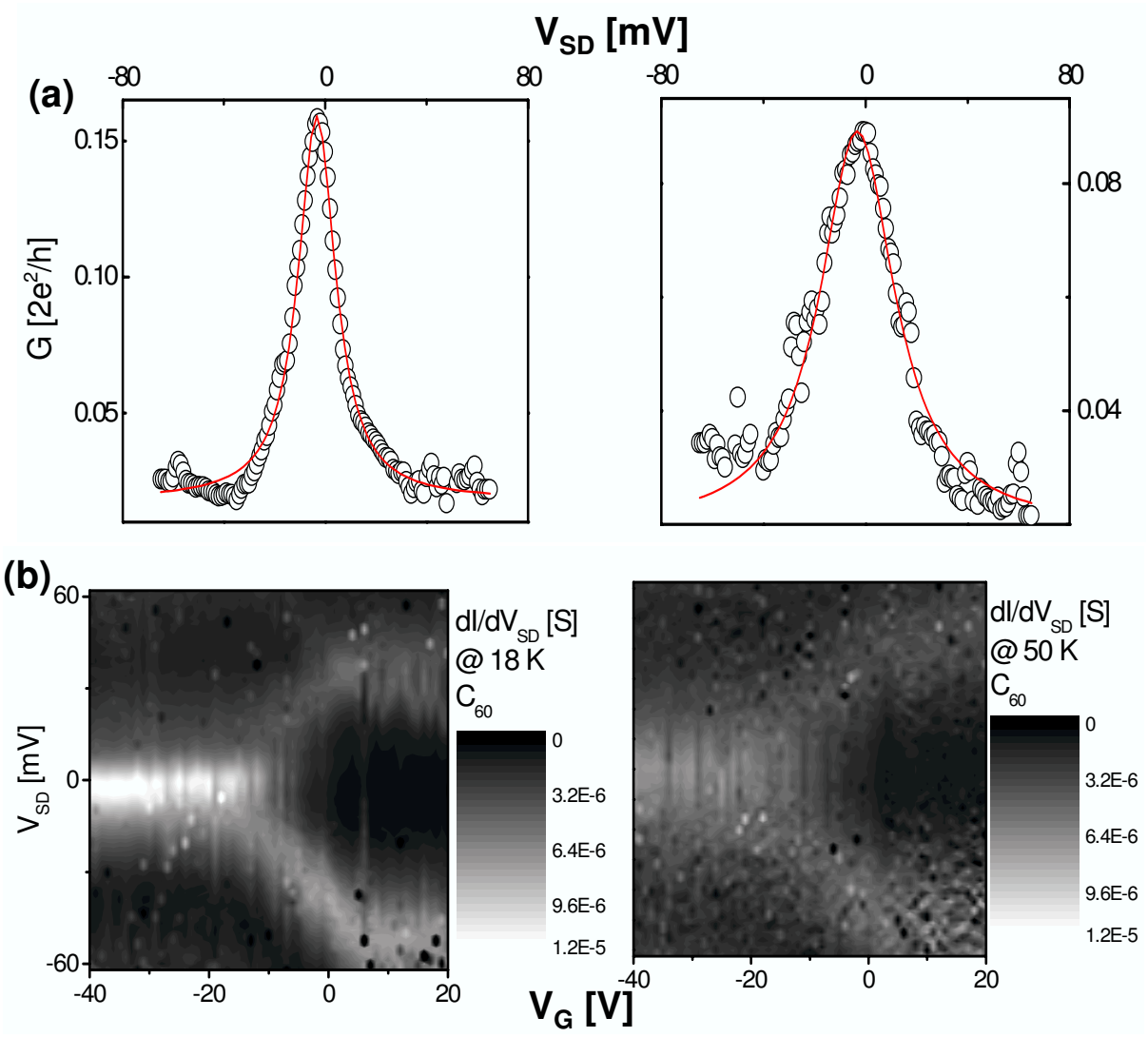

Figure 9.3 : a) Differential conductance of a SMT in the Kondo regime as a function of V_{SD} for the gate voltage indicated in the conductance maps. b) Conductance map of the SMT at 18 K (left) and 50 K (right) [23].

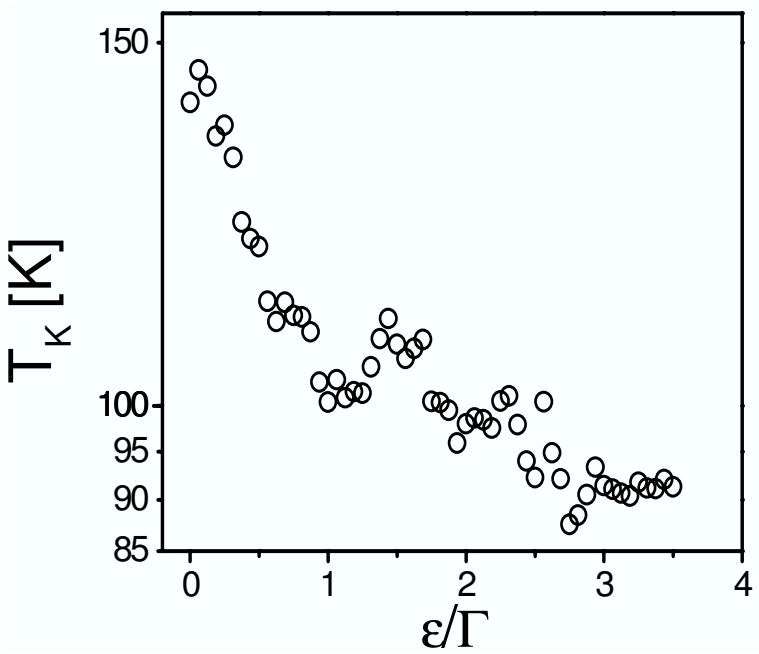

Figure 9.4 : A plot of T_K as a function of ε/Γ for the C_{60} device [23].

Figure 9.3b shows the conductance maps of another C_{60}-based SMT at two different temperatures. From the slope of the boundaries of the blockade regime (see eq.(8.5)), we can estimate the constant of proportionality between changes in eV_G and ε, the energy difference between the localized state and the Fermi level of the leads. For the device shown, the conversion factor $\frac{C_G}{C} \sim 2$ x 10^{-3}. The small size of the factor is not surprising given the oxide layer separating the molecule and the gate electrode is 200 nm thick. The width of the charge degeneracy resonance on the blockaded side of the degeneracy point sets an upper limit on Γ . The $T \to 0$ limit of that width is proportional to Γ, while the degeneracy resonance is thermally broad-

ened at finite temperature. The maximum Γ for this device is ~ 32 meV. Using the measured value of $\frac{C_G}{C}$ and knowing that $\varepsilon = 0$ at the degeneracy point, we can find δV_G using Eq.(8.5). Figure 9.4 shows T_K plotted as a function of ε/Γ for the device shown in Figure 9.3. The $T_K's$ of the plot are inferred from the $FWHM$s of the zero bias conductance peaks at the various gate voltages. As with $G(T)$, these data are, within the noise, nearly temperature independent below 20 K, and an average of several low temperature data sets are plotted. The $T_K's$ decrease as ε/Γ goes above one, which qualitatively agrees with eq.(8.4).

The conductance maps of Figure 9.3b clearly demonstrate that the zero bias resonance is still visible in the transport characteristics of the device up to at least 50 K, validating the high Kondo temperature implied by our analysis of the data. The high Kondo temperatures of our C_{60} SMTs may explain a phenomenon seen in STM experiments using probe tip made from C_{60} adsorbed on platinum-iridium [109]. Those STM measurements indicated a surprisingly narrow peaked density of states for the tips. One explanation for such a feature would be a Kondo resonance between the C_{60} and the tip, perhaps surviving even at 300 K.

We note that other studies of the Kondo effect in single-molecule devices [28, 29] were able to demonstrate the Zeeman splitting of the Kondo resonance in an applied magnetic field. Because of the large intrinsic width ($\sim 10 - 20$ meV) of the zero bias resonance that we observe, and the small size of the Zeeman splitting (115 μeV per Tesla for a free electron), this would be extremely difficult to observe in our samples.

In the two samples shown in Figure 9.1, we can see sidebands parallel to the zero-bias peak located at $V_{SD} \sim 35$ meV. They appear to evolve from the inelastic resonances ascribed to vibrational excitations during the tunneling process (see chapter 5). Similar resonances are seen in Kondo devices incorporating transition coordination complexes [25]. In chapter 7, we discussed IETS features from SMTs, and in top map of Fig. 7.1 of that chapter we saw an IETS feature that smoothly evolve from the blockaded region into the Kondo region, as indicated by the dash line. Through the transition the inelastic feature line shape and intensity changes. We interpret these side-band features that appear in parallel with the Kondo resonance peak and seem to be related to the vibrational mode of the molecules as evidence of phonon-assisted tunneling in the Kondo regime. These features originate from inelastic exchange between an unpaired electron occupying a vibrational level of the molecule and the conduction electrons. This is analogous to the photon-assisted satellite Kondo peaks observed in experiments where a semiconductor Kondo system is irradiated by monochromatic microwaves [110].

These observations of satellite features parallel to the Kondo resonances have led to several theoretical treatments of the Kondo resonance in SMTs in the presence of vibrational modes [111–113]. Some of these calculations have shown that the presence of the vibrational modes could lead to lowering the effective charging energy of the system and renormalizing the effective exchange coupling for the Kondo process, thus enhancing the Kondo temperature. The fact that the C_{60}-based SMTs have

$T_K > 100$ may be indication of that effect. Paaske and Flensberg [113] showed that in the presence of the Kondo resonance, the IETS features can acquire some peak character in the first derivative of the $I - V_{SD}$ curve. This could help explain why the vibrational features in Figure 9.1 appear as peaks instead of steps as described in chapter 7.

9.2 TMCC-Based Single Molecule Transistors

In this section we will describe Kondo physics in SMTs incorporating transition metal complexes designed to contain unpaired electrons. A structural diagram of the transition metal complexes measured in this study, as-synthesized, is shown in Figure 2.3. These molecules are chemically engineered to have four attachment sites for bonding with gold. Formation of Au-S covalent bonds is how these molecules are set into place between the nano-scale gaps. Presumably due to this attachment chemistry, we have a higher proportion of TMCC-based SMTs that exhibit Kondo physics than C_{60}-based SMTs. Also, we are more successful in taking temperature dependent data from the TMCC-based SMTs. As a function of gate voltage we observe transitions from Coulomb blockade conduction to Kondo conduction, manifested as a strong peak in the differential conductance at zero bias in one charge state. At fixed V_G, the temperature dependence of the conductance peaks' amplitude (see eq.(8.8)) and widths agree well with the expected forms for spin-1/2 Kondo resonances. Observed Kondo temperatures of these devices are$\sim$ 50 K. We find that $T_K(V_G)$ of these devices is strongly inconsistent with eq.(8.4), which predicts a strong suppression of T_K as V_G is shifted away from charge degeneracy. We suggest an explanation for this gate dependence based on strong intramolecular exchange, and present supporting electronic structure calculations.

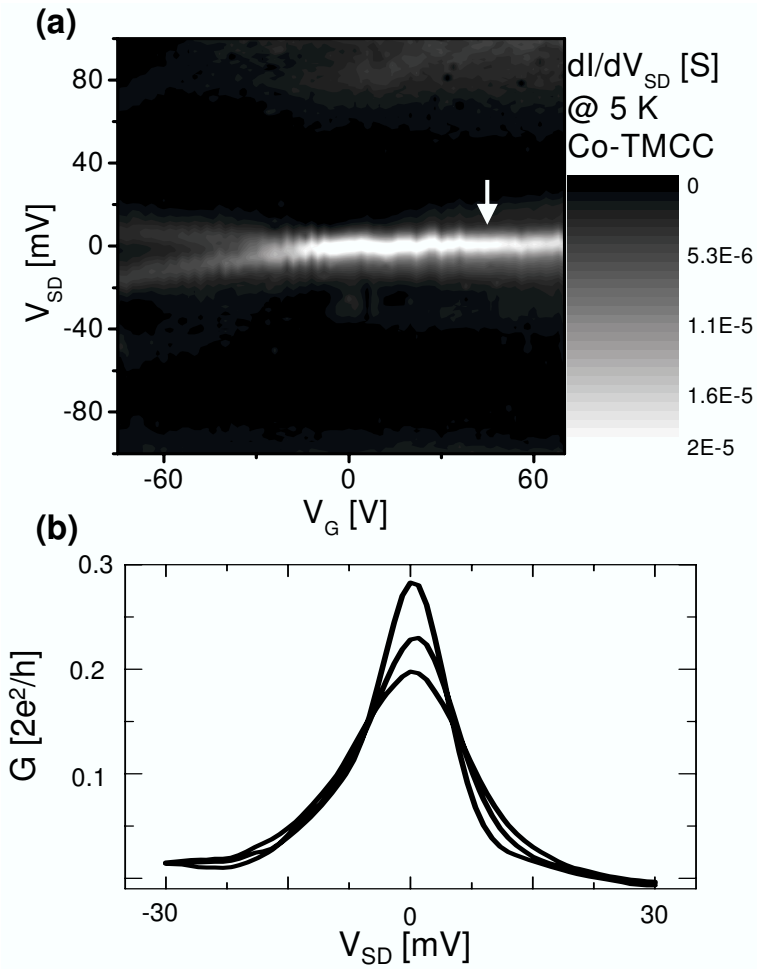

Figure 9.5 : (a) Conductance maps from Co-TMCC based SMT exhibiting the Kondo resonance at 5 K. Brightness scales from G = 0 (black) to 0.3 x $2e^2/h$. (b) G vs. V_{SD} at $V_G = 50$ V $\big($as indicated with white arrow in (a)$\big)$ at (top to bottom) 5K, 16K, and 30K.

Figure 9.5a shows a conductance map for a typical TMCC-based SMT exhibiting a Kondo resonance. We have sufficient gate coupling to observe only a single charge degeneracy point for each device. From the slopes of the boundaries of the Coulomb diamond, we find for this device the conversion factor between eV_G and ε to be $C_G/C \sim 10^{-4}$ The average value of this factor over all TMCC-based SMTs

measured is 10^{-3}. Using the width of the degeneracy points, we found that the typical maximum values inferred from 5 K data in these devices are 3-30 meV. We note that the edges of Coulomb blockade diamonds, while usually distinct in the non-Kondo charge state, are often much weaker or apparently absent in the Kondo charge state. This absence of obvious Coulomb blockade thresholds in the Kondo regime was observed in our C_{60}-based SMTs, and has been reported in other SMT experiments [114].

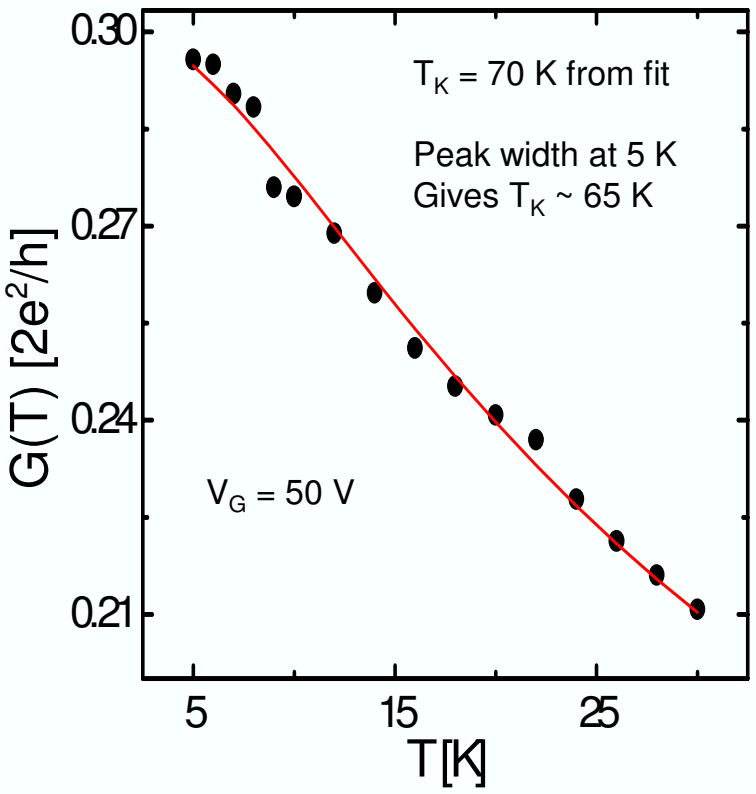

Figure 9.6 : Temperature dependence of Kondo resonant peak height for the device in Fig. 9.5a at $V_G = 50$ V. Solid red line is the expected semi-empirical functional form for spin-1/2 Kondo, with $T_K = 70$ K.

Figure 9.5b shows $G(V_{SD}, V_G = 50\text{ V})$ of the device at three temperatures. The resonant peak decreases in magnitude while increasing in width as the temperature is increased. Figure 9.6 show the peak height of the same device as a function of temperature. The solid line in is a fit to eq.(8.8), the semi-empirical expression for the spin-1/2 Kondo resonance in conductance. After the subtraction of a smooth background conductance, the adjustable parameters are the overall conductance scale, G_C, and T_K. We found quantitative consistency between the T_K inferred from this method and from (eq.(8.6)), assuming the FWHM of a resonance peak at 5 K to be $\sim \frac{2k_B T_K}{|e|}$.

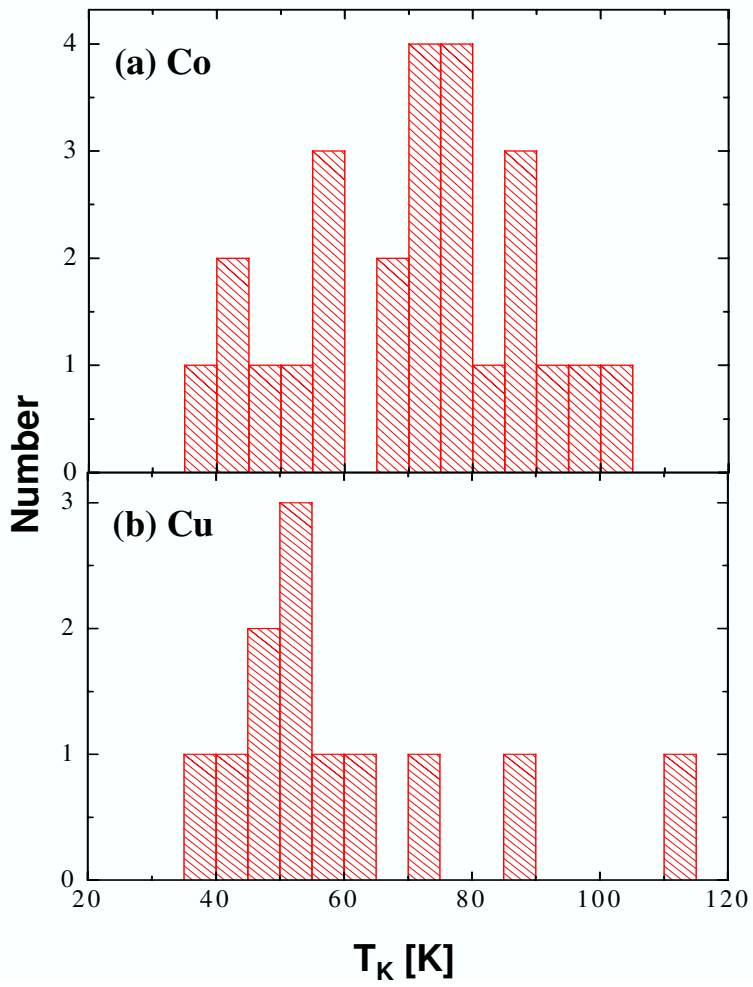

Figure 9.7 : (a,b) Histograms of Kondo Temperatures as inferred from peak widths for Co and Cu complex devices, respectively.

Figure 9.7a,b are histograms of Kondo temperatures inferred from resonance widths for 26 Co-TMCC-based SMTs (out of 921 electrode pairs examined at low temperatures), and 12 Cu-TMCC-based SMTs (out of 397 electrode pairs examined at low temperatures). In our analysis we are only considering devices that exhibit zero-bias resonances and clear charge degeneracy points. The T_K used in plotting

the histograms are extracted at various V_G, but as we will see below $T_K(V_G)$ is nearly constant in these devices.

From Figure 9.7 we can clearly see that the T_K value in our SMTs are very high, ranging from 30 to 110 K. These T_K values are similar to those reported in STM measurements of Co atoms on Au(111) , Cu(111) and Cu (100) surfaces [86, 115]. The fact that the T_K of our SMTs are comparable to those seen in STM experiments can seem at first somewhat surprising, since the transition metal ions in our SMTs are separated from the metal surface by the ligands of the molecules and in STM measurements the transition metal ions sit directly on the metal surfaces.

To understand the high T_K values we observe in our SMTs, let us recall from eq.(8.4) that the Kondo temperature is expected to be $k_B T_K = \frac{\sqrt{E_C \Gamma}}{2} \exp(-\frac{\pi\varepsilon(-\varepsilon+E_C)}{\Gamma E_C})$ in the Kondo regime, $(\varepsilon/\Gamma > 1)$. For small molecules, E_C is likely to be hundreds of meV, while is empirically tens of meV. The prefactor in eq.(8.4) then implies that T_K could be hundreds of Kelvin.

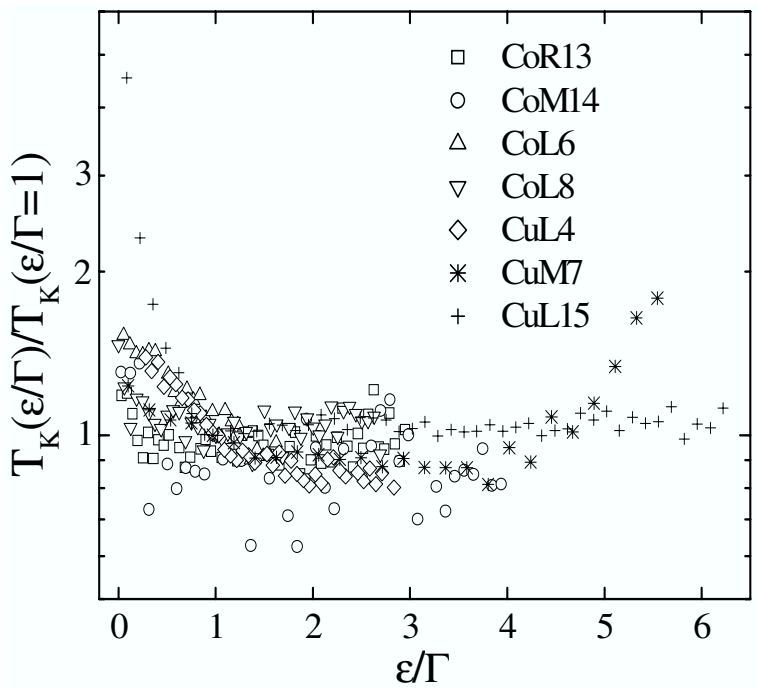

Figure 9.8 : $Log(T_K)$ inferred from FWHM of 5 K Kondo peaks in $G(V_{SD})$, as a function of V_G normalized by the width of the Coulomb blockade charge degeneracy point for several devices. Values of Γ inferred for these devices are, top down, 22.6, 11.5, 18, 3.3, 12.6, 14.2, and 26.8 meV.

Figure 9.8 shows (normalized) T_K as inferred from low-temperature resonance FWHM as a function of inferred ε/Γ for several devices. eq.(8.4) predicts a quadratic dependence of $log(T_K)$ with ε, with a minimum in T_K at $\varepsilon = \frac{E_C}{2}$. The measured dependence of $T_K(V_G)$ is clearly much less steep. Indeed for sample *CUM7*, T_K actually increases as V_G is shifted away from the nearest charge degeneracy. We note that the $T_K(V_G)$ dependence in our C_{60}-based SMTs and from SMTs experiments from other groups for $\varepsilon/\Gamma > 1$ are also weaker than expected.

Let us consider possible explanations for this deviation from expectations. The

simplest way to account for the disparity would be that the zero-bias peaks we observe in our devices are not true Kondo resonances. We can refute this by noting (a) the quantitative consistency of the functional forms for the resonance $G(V_{SD}, T)$ with the Kondo expectation; (b) the appearance of the zero-bias resonance coincident with passing through charge degeneracy points; (c) the lack of such resonances in control devices; (d) the similarity to other Kondo data reported in SMTs [28, 29].

A second possibility to explain our observation is that Γ for the Kondo-relevant level in our devices has non-trivial dependence on V_G, allowing ε/Γ to remain constant with V_G and "pinning" the devices in the mixed valence regime. However, since Γ depends on the atomic-scale geometry of the molecular-electrode interface, no obvious mechanism would do this reproducibly.

Orbital degeneracy for the unpaired spin on the molecule is another possible explaination [116]. When an N-fold degeneracy exists, T_K as defined by eq.(8.4) is enhanced, such that the denominator of the exponent becomes $N\Gamma E_C$. Thus the normalization of the abcissa in Fig. 9.8 would effectively be too large by a factor of N, qualitatively explaining the apparently weak dependence of $T_K(V_G)$ if $N \sim 5$. However, EPR spectra of both the Co and Cu-based complexes in solution phase show no indication of such a large degeneracy. Furthermore, we have performed spin-resolved calculations on the transition metal complexes to examine their electronic structure, as shown in Fig. 9.9. In neither complex are large degeneracies expected. While it is conceivable that the self-assembled compounds could have different orbital

degeneracies that the isolated molecules, it seems unlikely that both complexes, with their differing isolated electronic structures, would have such similar properties.

We suggest a possible explanation for the anomalous gate dependence is that the values of ε/Γ we extracted from our conductance maps are not the "true ε/Γ" relevant to the Kondo Hamiltonian from which eq.(8.4) were derived. In semiconductor quantum dot experiments [63], inferring ε/Γ the way that we have done result in $T_K(V_G)$ that is quantitatively consistent with eq.(8.4). However, intra-molecular exchange, where electrons within the molecule interact with other, is often small in semiconductor dots, but in molecular systems, it could be comparable energetically to the Γ, E_C, ε and δE of the molecular system. Strong exchange interaction could shift the majority and minority spin levels within the molecule relative to one another. Qualitatively, we can envision an occupied majority spin orbital participating in the Kondo resonance while being considerably deeper energetically than the highest occupied minority spin orbital. This would imply that the ε relevant to determining T_K could differ significantly from the ε inferred from conductance map. The occasional observation of Kondo resonances with similar T_K value on both sides of charge degeneracy points further indicates that intra-molecular exchange cannot be neglected in these devices.

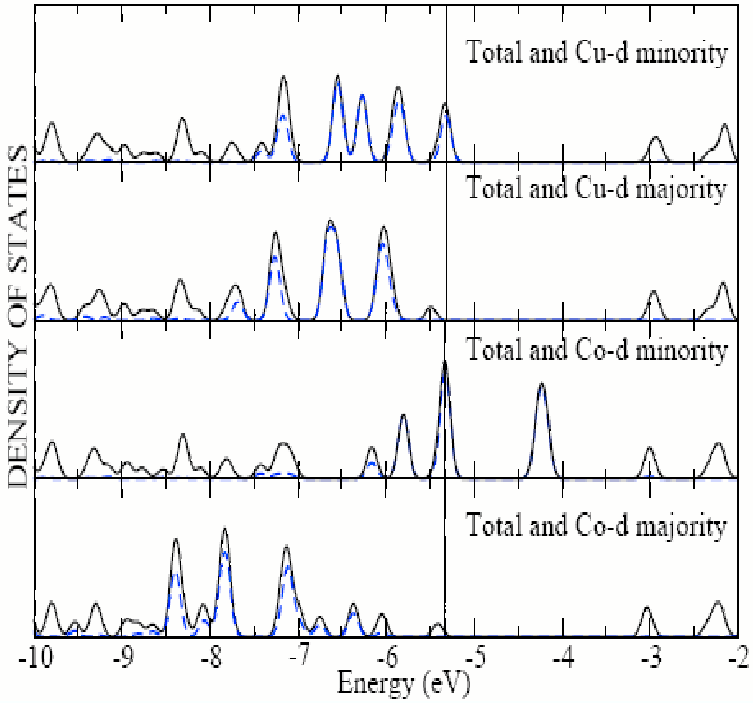

Figure 9.9 : DFT calculation of the energy structure of the TMCCs. Spin-resolved projected densities of states of the Cu(II) and Co(II) complexes, respectively. Minority (upper) and majority (lower) spin levels are indicated, demonstrating the strong effects of intramolecular exchange. The black curve is the total DOS, and the blue curve is the DOS projected onto the transition metal *d* states.

Our collaborators have performed calculations on the transition metal complexes to examine the strength of exchange correlations, as shown in (Figure 9.9). In both Co and Cu complexes, intra-molecular exchange is strong. In the Co case, to a good approximation ligand field effects split the d-states into one doubly degenerate, one nearly doubly degenerate, and one singly degenerate set of states. The complex has a total spin of $S = 3/2$, as confirmed by ESR. A minority spin half-occupied d state is at the Fermi level with two nearly degenerate d states 1.1 eV above the Fermi level and

the remaining occupied minority d electron 0.5 eV below the Fermi level. Exchange splittings pull the majority d-band down significantly, with the highest occupied majority d state 1.8 eV below the Fermi level. The fermiology is complicated by an additional delocalized unpolarized two-fold degenerate carbon 2p state lying 0.05 eV below the Fermi level. Also there is a delocalized doubly degenerate molecular state 0.85 eV below the Fermi level. The Cu complex has a total spin of S = 1/2, with the Fermi level unchanged in comparison to Co. This means that the minority spin d states are pulled to lower energies by approximately 1.1 eV as shown in figure 5. Jahn-Teller distortion is not considered, since the substrate-complex interaction is expected to be large compared to this effect.

These electronic structure calculations reveal another effect of strong intramolecular electronic correlations: the majority spin states have significantly greater d orbital hybridization with the ligand nitrogens than minority spin states. Thus in the single-particle level picture the effective Γ of a majority spin state could differ from that of a minority spin state. It has also been suggested [117] that screening correlations in the mixed valence regime can renormalize the measured Γ to a value different than the Γ relevant to the Kondo temperature. The large G of the majority spin state could help explain the observation that the Kondo temperatures observed in our TMCC-based SMTs are comparable to T_K measured from systems where the transition metal ion were directly bonded metallically to a metal surface.

These first density functional calculations indicate strong hybridization of major-

ity spin density with ligand states, suggesting that the strong interaction between the molecular spin and the metal conduction electrons seen in these experiments is an intrinsic consequence of the chemical structure of the molecule. Furthermore, these calculations show us that the exchange interactions in these molecules are strong enough to shift the majority and minority spin levels relative to each other significantly.

Although the density functional calculations do not directly explain the anomalous $T_K(V_G)$ behavior we observed in out TMCC-based SMTs, it does tell us two interesting things about the energy levels of the molecules: (1) The highest occupied and lowest unoccupied levels of both the Co and Cu based TMCC are minority spin d states that are almost completely localized on the transition metal ion. (2) The highest occupied majority spin states of both the Co and Cu based TMCC are further away from the Fermi level than their highest occupied minority spin states, but the highest occupied majority spin states of both molecules are delocalized over the entire molecule. In other words, the level in a TMCC-based SMT that has the smallest ε is a minority spin state with small Γ, and the level with the largest Γ is a majority spin state with a relatively large ε.

A handwave idea that could explain our observed of the weak $T_K(V_G$ behavior is that the molecular level that participates in the Kondo process is actually the highest occupied majority spin state, but the molecular level that participate in the Coulomb blockade process is the highest occupied (in the case of Co-TMCC based SMTs) or

lowest unoccupied (in the case of Cu-TMCC based SMTS) minority spin state. In this scenario the "true ε" that is relevant to the Kondo Hamiltonian would not be zero at the charge degeneracy point, and the measured Γ from the conductance map would not be the one relevant to the Kondo process. If the "true ε" is not tuned by the gate voltage in the Kondo regime the way we predicted, then this may explain our observed $T_K(V_G)$ behavior. This different $\varepsilon(V_G)$ dependence could also help explain the absence of obvious Coulomb blockade thresholds in many of our devices when the Kondo resonance is present.

However, there are two major problems with the handwave idea I proposed above. First, it implies that one should be able observe Kondo resonances in all accessible charge states, and this is not true experimentally except in very rare cases. We can argue that when we change the number of electrons on the TMCCs, it is plausible that this electronic excitation can reduce the coupling of the majority spin state to the electrode, thus removing the Kondo process from consideration, but without detail calculation of the electronically excited TMCCs, we cannot make that assertion rigorous. Second, the handwaving argument suggests that there are two different ε's in our system. One ε (the one that correspond to the minority spin state) is important in the part of the of the conductance map that show Coulomb blockade behavior and another ε (the one that correspond to the majority spin state) is important in the Kondo resonance side of the conductance map, and that at the charge degeneracy point of the conductance map there is some kind of discontinuous change in the ε

that is important to the system. In a way this problem have a similar origin as the first objection to the handwave argument in that it arise partly because we do not know how an electronic excitation affect the energy level structure and the coupling strength of the molecule.

Another possibility that may explain the anomalous $T_K(V_G)$ behavior in our SMTs is that coupling of charge and vibrational modes [111, 112] localized to the molecule can strongly renormalize both T_K and its gate dependence relative to the case with no vibrational coupling [118]. Preliminary numerical renormalization group calculation shows that large electron-phonon coupling in the molecule could lead to flat $T_K(V_G)$ behavior as observed in our experiments [118].

We end this section by presenting a result with implications for the eventual development of technologies based on SMTs. Previous investigations of SMTs have been performed at cryogenic temperatures in part because device geometric stability at the atomic level is difficult to maintain at room temperature in such systems. In the low temperature electromigration approach to SMT fabrication, the structure of the resulting electrodes and interfaces is frozen in a metastable state. Upon warming the devices to room temperature, annealing, surface reconstruction, and surface diffusion of Au atoms can significantly modify device conductance irreversibly, by altering the inter-electrode geometry.

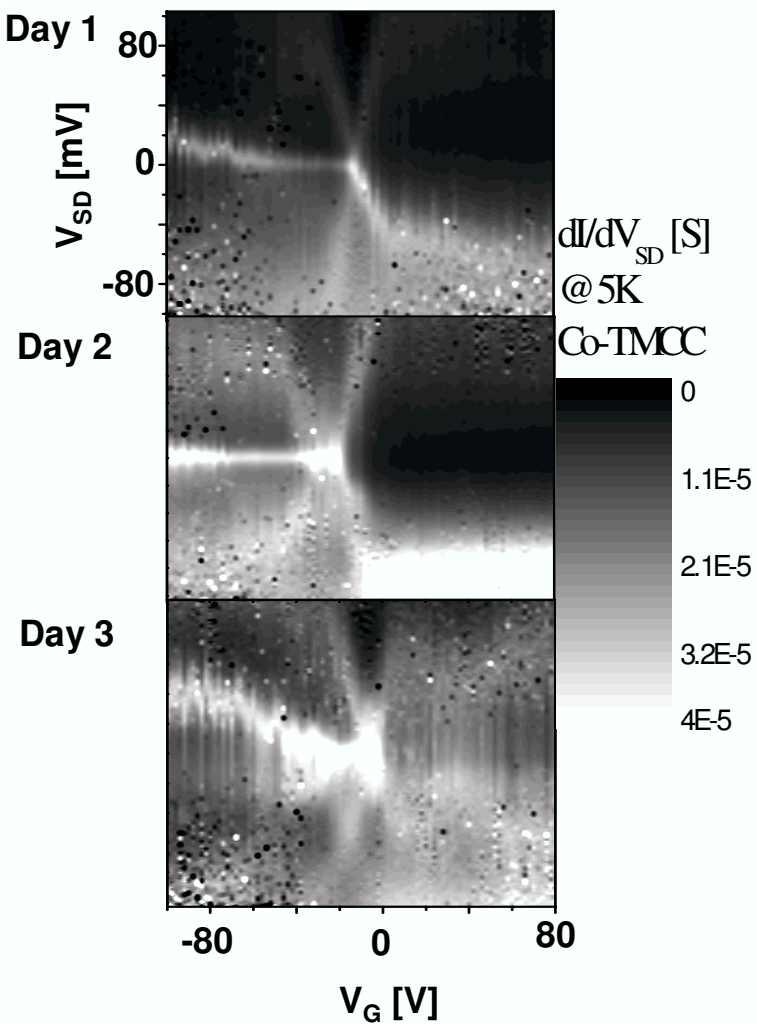

Figure 9.10 : conductance map of Co-complex SMT at 5 K on three successive days. Between each day, the device spent at least 18 hours at 300 K.

Figure 9.10 shows the conductance map of a particular Co-complex SMT at 5 K, on three successive days. Between day 1 and day 2, the sample was warmed (in high vacuum) to room temperature and allowed to sit for 18 hours before being re-cooled. A similar thermal cycling took place between day 2 and day 3. While details of the map change, the main essentials remain: a well-defined Coulomb blockade

with electron addition energy in excess of 100 meV, with a charge degeneracy point between V_G = -20 V and 0 V.

This particular device is clearly relatively robust under extended times at 300 K. We believe that the strong covalent bonding of the molecule to both source and drain electrodes is one reason for this impressive stability relative to bare junctions. By choosing a more refractory metal for electrodes, and with improvements in surface preparation, we believe that SMTs capable of room temperature operation are possible.

In measuring the electronic properties of single molecule transistors containing transition metal complexes, we observe strong Kondo physics, with $T_K(V_G)$ that is vastly weaker than that seen in semiconductor quantum dot realizations of the Kondo effect. We suggest that strong exchange within the molecule, as supported by electronic structure calculations of the complexes, likely play a role in such a departure from the predictions of the simple Kondo model. While a complete understanding will require more sophisticated modeling, these measurements demonstrate that correlated states involving SMTs can exhibit rich effects not seen in their semiconductor quantum dot counterparts. In both our C_{60}-based and TMCC-based SMTs we observed large Kondo temperatures. We note that fabricating SMTs that are mechanically and electrically stable and exhibit Kondo physics at room temperature would have significant implications for practical devices. Such SMTs would be switchable by gating from a Coulomb blockaded state to resonant conduction with

conductance approaching $2e^2/h$.

Chapter 10

Conclusion and Outlook

We have employed an electromigration technique to create single molecule transistors based on C_{60} and a new class of transition metal coordination complex. We have discussed in detail our fabrication procedure and method of characterizing SMTs. We place special emphasis on basing our analysis on the statistics of large ensembles of candidate devices and control samples.

Initial measurements demonstrated Coulomb blockade physics in theses devices with charging energy and energy level spacing significantly larger than 100 meV. These energy scales are an order of magnitude large than those observed in semiconductor quantum dot experiments, so these devices could, in principle, operate at liquid nitrogen temperature ($\sim$ 77 K) or higher. However, microscopic geometric instability in these devices due to atomic scale motion of the electrode metal and molecules makes it necessary for most of our SMT experiments to be preformed at temperatures below 20 K.

Further studies showed that quantum excitations of the molecules influence the electron transport behaviors of the SMTs. Interactions between the tunneling electrons and the vibrational modes of the molecules are manifested as enhanced conductance at specific energies in our transport measurements. Direct tunneling of electrons through vibrationally excited molecular states appears as lines of resonant

conductance in conductance maps whose slopes are parallel with the boundary of the Coulomb diamonds. Elastic cotunneling leads to uniform increases of conductance at all energies. Inelastic cotunneling, when unaffected by charge degeneracy, or interference with alternate tunneling channels (such as direct tunneling and higher-order tunneling processes) or the Kondo effect, gives rise to step-like features in the conductance maps. The onsets of these step-like features correspond to the energies of the vibration modes excited. The observation of inelastic cotunneling in our SMTs allows us to perform gate-modulated inelastic electron tunneling spectroscopy for the first time. The added tunability of our SMTs permits the examination of vibronic processes as a function of the energetic of the electronic levels, an experiment not possible in standard two-terminal devices.

Our SMTs also exhibit the Kondo effect at surprisingly high temperature (> 50 K). Kondo transport in a SMT is indicated by the presence of a zero-bias peak in the conductance for one charge state of the SMT and Coulomb blockade for the other. With our C_{60}-based SMTs we demonstrated for the first time that Kondo physics is observable in a SMT even when the molecule contains no metal ions. We also observed evidences of interactions between the Kondo effect and the vibrational modes of the molecules as well as strong exchange correlations of the electrons within the molecules. Our observations have helped spur several theoretical treatments of such interactions.

The study of single molecule devices is a rapidly progressing field. Our research

has concentrated on the transport properties of three-terminal molecular devices with gold electrodes fabricated by a means that provides little control over the placement of individual molecules in our devices. We have explored only a small portion of the available parameter space.

Future molecular devices could employ alternative electrode materials. Gold's high structure mobility, comparatively low melting point, and almost complete lack of oxide formation at ambient conditions have made it an ideal material for electromigration-based electrode fabrication. However, some of those virtues become drawbacks when we look from the standpoint of interface stability and geometric control of the microscopic structures of our devices. The use of more refractory metals such as platinum and palladium is one route toward improving device stability. Another route is passivation. By surrounding the molecule of interest with a dense array of short, inert molecules, such as alkane chains, one can reduce the motion of the surrounded molecule [119] as well as the metal on which the short molecules are attached.

Silicon has also been suggested as an electrode material [120, 121]. Despite its relatively low density of states at the Fermi level compared to metals, its surface states, and its tendency to form depletion layers at interfaces, silicon has the advantage of being one of the best studied materials in the world. The surface chemistry of silicon, its oxide, and its defects are known, and many procedures already exist to manipulate them. However, electromigration cannot be used to fabricate nanoscale electrode gaps in silicon. One may create nanoscale gaps in silicon structures

by controlled etching as has been demonstrated in III-V semiconductor multilayer structures [120].

But, even for electrode materials that would allow for electromigration fabrication, we can think of alternate fabrication methods that could allow for better control over the placement of molecules. For example, we can imagine synthnesizing a solution of well separated single-crystal metallic nano-rods that have nanoscale diameter and micron-scale length with well-defined and controllable crystallographic surfaces. Then, we mix the nano-rods with a solution of molecules that have been functionalized to bond with the crystallographic surfaces that correspond to the ends of the nano-rods. These molecules could be engineered to have two attachment sites on opposite ends, thus allowing for the formation of rod-molecule-rod structures. We can spin-cast the resulting solution on a substrate, then use standard lithography methods to make contacts with the various rod-molecule-rod structures. Such structures cannot be made at present, but with the recent advances in nanocrystal growth [122], it may be possible in the near future.

In addition to alterative device fabrication, we can consider different experimental approaches. We have considered only DC measurements of our device, but there are higher frequency measurements that could be tried that range from radio to optical frequencies. Radio-frequency semiconductor quantum dots have been used as highly sensitive, broad bandwidth electrometers at dilution fridge temperatures ($\sim$ 100 miliKelvin) [123, 124]. With the hundreds of meV charge addition energies of SMTs,

rf-SMT would be able to operate at liquid nitrogen temperatures. Based on results of high frequency STM experiments [125–128], it may be possible to detect the spin state of a single molecule in a magnetic field through radio-frequency measurement of a SMT. Optical excitation of the inter-electrode gap could allow excitation of the electrodes' surface plasmons, which may lead to single molecule light emission during inelastic tunneling [129] and observation of nonlinear optical processes such as surface enhanced Raman scattering [130].

My study of single molecule transistors has been a rewarding experience. We observed interesting physical phenomena that contribute new knowledge and understandings to the growing field of nanoscale electronics.

Bibliography

[1] A. Aviram and M.A. Ratner, "Molecular rectifiers," Chem. Phys. Lett. **29**, 277–283 (1974).

[2] A. Nitzan and M.A. Ratner, "Electron transport in molecular wire junctions," Science **300**, 1384–1389 (2003).

[3] J.M Tour, "Molecular electronics. Synthesis and testing of components," Acc. Chem. Res. **33**, 791–804 (200).

[4] J. Chen, M.A. Reed, A.M. Rawlett, and J. M. Tour, "Large On-Off Ratios and Negative Differential Resistance in a Molecular Electronic Device," Science **286**, 1550 (1999).

[5] M.A. Reed, J. Chen, A.M. Rawlett, D.W. Price, and J.M. Tour, "Molecular random access memory cell," Appl. Phys. Lett. **78**, 3735–3737 (2001).

[6] C.P Collier, E.W. Wong, M. Belohradsky, F.M. Raymo, J.F. Stoddart, P.J. Keukes, R.S. Williams, and J.R. Heath, "Electronically configurable molecular-based logic gates," Science **285**, 391–394 (1999).

[7] C.P. Collier, G. Mattersteig, E.W. Wong, Y. Luo, K. Beverly, J. Sampaio, F.M. Raymo, J.F. Stoddart, and J.R. Heath, "A [2]catenane-based solid state electronically reconfigurable switch," Science **289**, 1172–1175 (2000).

[8] J.G. Kushmerick, D.B. Holt, J.C. Yang, J. Naciri, M.H. Moore, and R. Shashidar, "Metal-molecule contacts and charge transport across monomolecular layers: measurement and theory," Phys. Rev. Lett. **89**, 086802–1–086802–4 (2002).

[9] J.M. van Ruitenbeek, A. Alvarez, I. Pineyro, C. Grahmann, P. Joyez, M. H. Devoret, D. Esteve, and C. Urbina, "Adjustable nanofabricated atomic size contacts," Rev. Sci. Instr. **67**, 108–111 (1996).

[10] M.A. Reed, C. Zhou, C.J. Muller, T.P. Burgin, and J.M. Tour, "Conductance of a molecular junction," Science **278**, 252–254 (1997).

[11] E. Scheer, N. Agrait, J.C. Cuevas, A.L. Yeyati, B. Ludolph, A. Martin-Rodero, G. Rubio Bollinger, J. M. van Ruitenbeek, and C. Urbina, "The signature of chemical valence in the electrical conduction through a single-atom contact," Nature **394**, 154–157 (1998).

[12] J. Reichert, R. Ochs, D. Beckmann, H.B. Weber, M. Mayor, and H. von Lohneysen, "Driving current through single organic molecules," Phys. Rev. Lett. **88**, 176804 (2002).

[13] R.H.M. Smit, Y. Noat, C. Untiedt, N.D. Lang, M.C. van Hemert, and J.M. van Ruitenbeek, "Measurement of the conductance of a hydrogen molecule," Nature **419**, 906–909 (2002).

[14] C. Joachim, J.K. Gimzewski, R.R. Schlittler, and C. Chavy, "Electronic transparence of a single C_{60} molecule," Phys. Rev. Lett. **74**, 2102–2105 (1995).

[15] A. Yazdani, D.M. Eigler, and N. D. Lang, "Off-resonance conduction through atomic wires," Science **272**, 1921–1924 (1996).

[16] S. Datta, W. Tian, S. Hong, R. Reifenberger, J.I. Henderson, and C. P. Kubiak, "Current-voltage characteristics of self-assembled monolayers by scanning tunneling microscopy," Phys. Rev. Lett. **79**, 2530–2533 (1997).

[17] B.C. Stipe, M. A. Rezaei, and W. Ho, "Single-molecule vibrational spectroscopy and microscopy," Science **280**, 1732–1735 (1998).

[18] Z.J. Donhauser, B.A. Mantooth, K.F. Kelly, L. A. Bumm, J.D. Monnell, J.J. Stapleton, D.W. Price Jr., A.M. Rawlett, D.K. Allara, J.M. Tour, and P.S. Weiss, "Conductance switching in single molecules through conformational changes," Science **292**, 2303–2307 (2001).

[19] G.K. Ramachandran, T.J. Hopson, A.M. Rawlett, L.A. Nagahara, A. Primak, and S.M. Lindsay, "A bond-fluctuation mechanism for stochastic switching in wired molecules," Science **300**, 1413–1416 (2003).

[20] D.J. Wold and C.D. Frisbie, "Fabrication and characterization of metal-molecule-metal junctions by conducting probe atomic force microscopy," J. Am. Chem. Soc. **123**, 5549–5556 (2001).

[21] X.D. Cui, A. Primak, X. Zarate, J. Tomfohr, O.F. Sankey, A.L. Moore, T.A. Moore, D. Gust, G. Harris, and S.M. Lindsay, "Reproducible measurement of single-molecule conductivity," Science **294**, 571–574 (2001).

[22] R.A. Metzger, B. Chen, U. Hopfner, M.V. Lakshmikantham, D. Vuillaume, T. Kawai, X. Wu, H. Tachibana, T.V. Hughes, H. Sakurai, J.W. Baldwin, C. Hosch, M.P. Cava, L. Brehmer, and G.J. Ashwell, "Unimolecular electrical rectification in hexadecylquinolinium tricyanoquinodimethanide," J. Am. Chem. Soc. **119**, 10455–10466 (1997).

[23] L.H. Yu and D. Natelson, "The Kondo effect in C_{60} single molecule transistors," Nano Letters **4**, 79–83 (2004).

[24] L.H. Yu and D. Natelson, "Transport in single-molecule transistors: Kondo physics and negative differential resistance," Nanotechnology **15**, S1–S8 (2004).

[25] L.H. Yu, Z.K. Keane, J.W. Ciszek, L. Cheng, M.P. Stewart, J. M. Tour, and D. Natelson, "Inelastic electron tunneling via molecular vibrations in single-molecule transistors," Phys. Rev. Lett. **93**, 266802–1–266802–4 (2004).

[26] H. Park, A. K. L. Lim, A. P. Alivisatos, J. Park, and P. L. McEuen, "Fabrication of metallic electrodes with nanometer separation by electromigration," Appl. Phys. Lett. **75**, 301–303 (1999).

[27] H. Park, J. Park, A.K.L. Lim, E.H. Anderson, A.P. Alivisatos, and P.L.

McEuen, "Nanomechanical oscillations in a single-C_{60} transistor," Nature **407**, 57–60 (2000).

[28] J. Park, A. N. Pasupathy, J. I. Goldsmith, C. Chang, Y. Yaish, J. R. Petta, M. Rinkowski, J. P. Sethna, H. D. Abruña, P. L. McEuen, and D. C. Ralph, "Coulomb blockade and the Kondo effect in single-atom transistors," Nature **417**, 722–725 (2002).

[29] W. Liang, M. P. Shores, M. Bockrath, J. R. Long, and H. Park, "Kondo resonance in a single-molecule transistor," Nature **417**, 725–729 (2002).

[30] L.A. Bumm, J.J. Arnold, T.D. Dunbar, D.L. Allara, and P.S. Weiss, "Electron transfer through organic molecules," J. Phys. Chem. B **103**, 8122–8127 (1999).

[31] W. Wang, T. Lee, and M.A. Reed, "Mechanism of electron conduction in self-assembled alkanethiols monolayer devices," Phys. Rev. B **68**, 035416–1–035416–7 (2003).

[32] J.Park, A. N. Pasupathy, J. I. Goldsmith, A. V. Soldatov, C. Chang, Y. Yaish, J. P. Sethna, H. Abrua, D. C. Ralph, and P. L. McEuen, "Wiring up single molecules," Thin Solid Films **438**, 457–461 (2003).

[33] H. Grabert and M. H. Devoret, eds., *Single Charge Tunneling: Coulomb Blockade Phenomena in Nanostructures*, NATO ASI series B: Physics Vol. 294 (Plenum, New York, 1992).

[34] C. Pasquier, U. Meirav, F.I.B. Williams, D.C. Glattli, Y. Jin, and B. Etienne, "Quantum limitation on Coulomb blockade observed in a 2D electron-system," Phys. Rev. Lett. **70**, 69–72 (1993).

[35] T.M. Eiles, G. Zimmerli, H.D. Jensen, and J.M. Martinis, "Thermal enhancement of cotunneling in ultra-small tunnel-junctions," Phys. Rev. Lett. **69**, 148–151 (1992).

[36] L.J. Geerligs, D.V. Averin, and J.E. Mooij, "Observation of macroscopic quantum tunneling through the Coulomb energy barrier," Phys. Rev. Lett. **65**, 3037–3040 (1990).

[37] S. De Franceschi, S. Sasaki, J. M. Elzerman, W. G. van der Wiel, S. Tarucha, and L. P. Kouwenhoven, "Electron cotunneling in a semiconductor quantum dot," Phys. Rev. Lett. **86**, 878–881 (2001).

[38] R. Schleser, T. Ihn, E. Ruh, K. Ensslin, M. Tews, D. Pfannkuche, D.C. Driscoll, and A.C. Gossard, "Cotunneling-mediated transport through excited states in the Coulomb-blockade regime," Phys. Rev. Lett. **94**, 206805 (2005).

[39] M.M. Deshmukh, S. Kleff, S. Gueron, E. Bonet, A.N. Pasupathy, J. von Delft, and D.C. Ralph, "Magnetic anisotropy variations and nonequilibrium tunneling in a cobalt nanoparticle," Phys. Rev. Lett. **87**, 226801 (2001).

[40] J.G. Kushmerick, J. Lazorcik, C. H. Patterson, R. Shashidhar, D. S. Seferos,

and G. C. Bazan, "Vibronic contributions to charge transport across molecular junctions," Nano Letters **4**, 639–642 (2004).

[41] W.Y. Wang, T. Lee, I. Kretzschmar, and M. A. Reed, "Inelastic electron tunneling spectroscopy of an alkanedithiol self-assembled monolayer," Nano Letters **4**, 643–646 (2004).

[42] J. Kondo, "Resistance minimum in dilute magnetic alloys," Prog. Theor. Phys. **32**, 37–49 (1964).

[43] H.S. Nalwa, ed., *Handbook of Organic Electronics and Photonics* (American Scientific Publishers, New York, 2006).

[44] P.S. Ho and T. Kwok, "Electromigartion in metals," Reports on Progress in Physics **52**, 301–348 (1989).

[45] T.R. Ohno, Y. Chen, S.E. Harvey, G.H. Kroll, J.H. Weaver, R.E. Haufler, and R.E. Smalley, "C_{60} bonding and energy-level alignment on metal and semiconductor surfaces," Phys. Rev. B **44**, 13747–13755 (1991).

[46] S.J. Chase, W.S. Bacsa, M.G. Mitch, L.J. Pilione, and J.S. Lannin, "Surface-enhenced Raman scattering and photoemission of C_{60} on noble-metal surfaces," Phys. Rev. B **46**, 7873–7877 (1992).

[47] C. Chavy, C. Joachim, and A. Altibelli, "Interpretation of STM images - C_{60} on the gold(110) surface," Chem. Phys. Lett. **214**, 569–575 (1993).

[48] R.S. Ruoff and A.P. Hickman, "Van der Waals binding of Fullerenes to a graphite plane," Journal of Chemical Physics **97**, 2494–2496 (1993).

[49] M.S. Dresselhaus, G. Dresselhaus, and J.M. Eklund, *Science of Fullerenes and Carbon Nanotubes* (Academic, New York, 1996).

[50] K.F. Kelly and A. Osgood (2004), characterization of C_{60} monolayer with STM.

[51] A. Ulman, "Formation and structure of self-assembled monolayers," Chemical Reviews **96**, 1533–1554 (1996).

[52] J. Kordis, K.A. Gingerich, and R.J. Seyse, "Atomization energier and heats of formation of gaseous AU2, TB2, TBAU, HOAU, TBAU2, AND HOAU2," Journal of Chemical Physics **61**, 5114–5121 (1974).

[53] O. Dietz, V.M. Rayon, and G. Frenking, "Molecular structures, bond energies, and bonding analysis of group 11 cyanides TM(CN) and isocyanides TM(NC) (TM = Cu, Ag, Au)," Inorganic Chemistry **42**, 4977–4984 (2003).

[54] J.W. Ciszek, M. P. Stewart, and J. M. Tour, "Spontaneous assembly of organic thiocyanates on gold sufaces. Alternative precursors for gold thiolate assemblies," Journal of the American Chemical Society **126**, 13172–13173 (2004).

[55] Q.S. Xie, E. Perezcordero, and L. Echegoyen, "Electrochemical detection of $C_{60}(6^-)$ and $C_{70}(6^-)$ - enhanced stability of Fulleridesin solution," Journal of the American Chemical Society **114**, 3978–3980 (1992).

[56] R. Stratton, "Volt-current characteristics for tunneling through insulating films," J. Phys. Chem. Sol. **23**, 1177–1190 (1962).

[57] C.W.J. Beenakker, "Theory of Coulomb-blockade oscillations in the conductance of a quantum dot," Phys. Rev. B **44**, 1646–1656 (1991).

[58] G. Timp, ed., *Nano-Science and Technology* (AIP Press, New York, 1997).

[59] L. L. Sohn, L. P. Kouwenhoven, and G. Schön, eds., *Mesoscopic Electron Transport* (Plenum, New York and London, 1997).

[60] P.W. Anderson, "Localized magnetic states in metals," Phys. Rev. **124**, 41–53 (1961).

[61] D. Goldhaber-Gordon, H. Shtrikman, D. Mahalu, D. Abusch-Magder, U. Meirav, and M.A. Kastner, "Kondo effect in a single-electron transistor," Nature **391**, 156–159 (1998).

[62] S.M. Cronenwett, T.H. Oosterkamp, and L.P. Kouwenhoven, "A tunable Kondo effect in quantum dots," Science **281**, 540–544 (1998).

[63] D. Goldhaber-Gordon, J. Göres, M. A. Kastner, H. Shtrikman, D. Mahalu, and U. Meirav, "From the Kondo regime to the mixed-valence regime in a single-electron transistor," Phys. Rev. Lett. **81**, 5225–5228 (1998).

[64] W.G. van der Wiel, S. de Franceschi, T. Fujisawa, J. M. Elzerman, S. Tarucha, and L. Kouwenhoven, "The Kondo effect in the unitary limit," Science **289**,

2105–2108 (2000).

[65] M. Pustilnik and L. Glazman, "Kondo effect in quantum dots," Journal of Physics: Cond. Mat. **13**, R513–R537 (2004).

[66] E. Bonet, M.M. Deshmukh, and D.C. Ralph, "Solving rate equations for electron tunneling via discrete quantum states," Phys. Rev. B **65**, 045317–1–045317–10 (2001).

[67] E.B. Foxman, U. Meirav, P.L. McEuen, M.A. Kastner, O. Klein, P.A. Belk, D.M. Abusch, and S.J. Wind, "Crossover from single-level to multilevel transport in artifical atoms," Phys. Rev. B **50**, 14193–14199 (1994).

[68] G.C. Schatz and M.A. Ratner, *Quantum Mechanics in Chemistry* (Prentice Hall, Englewood Cliffs, 1993).

[69] R. Heid, L. Pintschovius, and J.M. Godard, "Eigenvectors of internal vibrations of C_{60}: Theory and experiment," Phys. Rev. B **56**, 5925–5936 (1997).

[70] R.A. Marcus, "On the theory of oxidation-reduction reactions involving electron transfer," J. Chem. Phys. **24**, 966–978 (1956).

[71] H.M. McConnell, "Intramolecular charge transfer in aromatic free radicals," J. Chem. Phys. **35**, 508–515 (1961).

[72] M.D. Newton and N. Sutin, "Electron-Transfer Reactions in Condensed Phases," Annual Review of Physical Chemistry **35**, 437–480 (1984).

[73] M.D. Newton, "Quantum chemical probes of electron-transfer kinetics - the nature of donor-acceptor interactions," Chemical Reviews **91**, 767–792 (1991).

[74] R.C. Jaklevic and J. Lambe, "Molecular vibration spectra by electron tunneling," Phys. Rev. Lett. **17**, 1139–1140 (1966).

[75] E.L. Wolf, *Principles of Electron Tunneling Spectroscopy* (Oxford University Press, New York, 1985).

[76] K.W. Hipps and U. Mazur, "Inelastic electron-tunneling - an alternative molecular-spectroscopy," J. Phys. Chem. **97**, 7803–7814 (1993).

[77] S. Gregory, "Inelastic tunneling spectroscopy and single-electron tunneling in an adjustable microscopic tunnel junction," Phys. Rev. Lett. **64**, 689–692 (1990).

[78] D.T Zimmerman and G. Agnolet, "Inelastic electron tunneling spectroscopy measurements using adjustable oxide-free tunnel junctions," Rev. Sci. Instr. **72**, 1781–1787 (2001).

[79] B.C. Stipe, M.A. Rezaei, and W. Ho, "Coupling of vibrational excitation to the rotational motion of a single adsorbed molecule," Phys. Rev. B **81**, 1263–1266 (1998).

[80] J. Gaudioso, H.J. Lee, and W. Ho, "Vibrational analysis of single molecule chemistry: Ethylene dehydrogenation on Ni(110)," Journal of the American

Chemical Society **121**, 8479–8485 (1999).

[81] J. Gaudioso, L. J. Lauhon, and W. Ho, "Vibrationally mediated negative differential resistance in a single molecule," Phys. Rev. Lett. **85**, 1918–1921 (2000).

[82] L.J. Lauhon and W. Ho, "Effects of temperature and other experimental variables on single molecule vibrational spectroscopy with the scanning tunneling microscope," Review of Scientific Instruments **72**, 216–223 (2001).

[83] B.N.J. Persson and A. Baratoff, "Inelastic electron-tunneling from a metal tip - The contribution from resonant processes," Phys. Rev. Lett. **59**, 339–342 (1987).

[84] A. Nitzan, "On the line widths of vibrational features in inelastic electron tunneling spectroscopy," Nano Letters **4**, 1605–1611 (2004).

[85] M. Galperin, M. A. Ratner, and A. Nitzan, "Inelastic electron tunneling spectroscopy in molecular junctions: peaks and dips," Journal of Chemical Physics **121**, 11965–11979 (2004).

[86] V. Madhavan, W. Chen, T. Jamneala, M. F. Crommie, and N. S. Wingreen, "Tunneling into a single magnetic atom: spectroscopic evidence for the Kondo resonance," Science **280**, 567–569 (1998).

[87] V. Madhavan, W. Chen, T. Jamneala, M. F. Crommie, and N. S. Wingreen, "Local spectroscopy of a Kondo impurity: Co on Au(111)," Phys. Rev. B **64**,

165412–1–165412–11 (2001).

[88] N.S. Wingreen and Y. Meir, "Anderson model out of equilibrium: Noncrossing-approximation approah to transport through a quantum dot," Phys. Rev. B **49**, 11040–11052 (1994).

[89] A. Troisi, M. A. Ratner, and A. Nitzan, "Vibronic effects in off-resonant molecular wire conduction," J. Chem. Phys. **118**, 6072–6082 (2003).

[90] Y.-C. Chen, M. Zwolak, and M. Di Ventra, "Inelastic current-voltage characteristics of atomic and molecular junctions," Nano Letters **4**, 1709–1712 (2004).

[91] G. Socrates, *Infrared and Raman Characteristic Group Frequencies: Tables and Charts* (Wiley, New York, 2001).

[92] H.S. Kato, J. Noh, M Hara, and M Kawai, "An HREELS study of alkanethiol self-assembled monolayers on Au(111)," Journal of physical chemistry B **106**, 9655–9658 (2002).

[93] A.C. Hewson, *The Kondo Problem to Heavy Fermions*, Cambridge Studies in Magnetism (Cambridge University, Cambridge and UK, 1997).

[94] N.W. Ashcroft and N.D. Mermin, *Solid State Physics* (Saunder College Publishing, New York, 1976).

[95] K.G. Wilson, "The renormalization group: critical phenomena and the Kondo problem," Rev. Mod. Phys. **47**, 773–840 (1974).

[96] N. Andrei, "Diagonalization of the Kondo Hamiltonian," Phys. Rev. Lett. **45**, 379–382 (1980).

[97] P.B. Wiegmann, "Toward an exact solution of the Anderson model," Phys. Rev. Lett. **80**.

[98] M.P. Sarachik, E. Corenzwit, and L.D. Longinotti, "Resistivity of Mo-Nb and Mo-Re Alloys Containing one percent Fe," Phys. Rev. **135**, A1041–A1045 (1964).

[99] G. Grner and A. Zawadowski, "Magnetic impurities in non-magnetic metals," Rep. Prog. Phys. **37**, 1497–1583 (1974).

[100] C.M. Varma, "Mixed-valence compounds," Rev. Mod. Phys. **48**, 219–238 (1976).

[101] P. Nozieres, "A Fermi liquid description of the Kondo problem at low temperatures," J. Low Temp. Phys. **17**, 31–42 (1974).

[102] J.R. Schrieffer and P.A. Wolff, "Relation between the Anderson and Kondo Hamiltonians," Phys. Rev. **149**, 491–492 (1966).

[103] P.W. Anderson, "Local moments and localized states," Rev. Mod. Phys. **50**, 191–201 (1978).

[104] J. Konig, J. Schmid, H. Schoeller, and G. Schon, "Resonant tunneling through ultrasmall quantum dots: Zero-bias anomalies, magnetic field dependence, and

boson-assisted transport," Phys. Rev. B **54**, 16820–16837 (1996).

[105] T.A. Costi, A.C. Hewson, and V. Zlatic, "Transport coefficients of the Anderson model via the numerical renormalization group," Journal of Physics: Cond. Mat. **6**, 2519–2558 (1994).

[106] F.D.M. Haldane, "Scaling Theory of Asymmetric Anderson Model," Phys. Rev. Lett. **40**, 416–419 (1978).

[107] D.C. Langreth, "Friedel sum rule for Andersons model of localized impusity states," Phys. Rev. **150**, 516–518 (1966).

[108] T.K. Ng and P.A. Lee, "On-site Coulomb repulsion and resonant tunneling," Phys. Rev. Lett. **61**, 1768–1771 (1988).

[109] K.F. Kelly, D. Sarkar, G. D. Hale, S. J. Oldenburg, and N. J. Halas, "Threefold electron scattering on graphite observed with C_{60}-adsorbed STM tips," Science **272**, 1371–1373 (1996).

[110] A. Kogan, S. Amasha, and M. A. Kastner, "Photon-induced Kondo satellites in a single-electron transistor," Science **304**, 1293–1295 (2004).

[111] P.S. Cornaglia, H. Ness, and D. R. Grempel, "Many-body effects on the transport properties of single-molecule devices," Phys. Rev. Lett. **93**, 147201–1–147201–4 (2004).

[112] P.S. Cornaglia, D. R. Grempel, and H. Ness, "Quantum transport through a deformable molecular transistor," Phys. Rev. B **71**, 075320 (2005).

[113] J. Paaske and K. Flensberg, "Vibrational sidebands and the Kondo effect in molecular transistors," Phys. Rev. Lett. **94**, 176801–1–176801–4 (2005).

[114] A.N. Pasupathy, R. C. Bialczak, J. Martinek, J. E. Grose, L. A. K. Donev, P. L. McEuen, and D. C. Ralph, "The Kondo effect in the presence of ferromagnetism," Science **306**, 86–89 (2004).

[115] N. Knorr, M.A. Schneider, L. Diekhner, P. Wahl, and K. Kern, "Kondo effect of single Co adatoms on Cu surfaces," Phys. Rev. Lett. **88**.

[116] J. Bonca and J.E. Gubernatis, "Qunatum Monte Carlo simulations of the degenerate single-impurity Anderson model," Phys. Rev. B **47**, 13137–13146 (1993).

[117] Q. Si and G. Kotliar, "Metallic non-Fermi-liquid phases of an extended Hubbard model in infinite dimensions," Phys. Rev. B **48**, 13881–13903 (1993).

[118] D.R. Grempel (2005), private communication.

[119] M.T. Cygan, T.D. Dunbar, J.J. Arnold, L.A. Bumm, N.F. Shedlock, T.P. Burgin, L. Jones, D.L. Allara, J.M. Tour, and P.S. Weiss, "Insertion, conductivity, and structures of conjugated organic oligomers in self-assembled alkanethiol

monolayers on Au111," Journal of the American Chemical Society **120**, 2721–2732 (1998).

[120] R. Krahne, A. Yacoby, H. Shtrikman, I. Bar-Joseph, T. Dadosh, and J. Sperling, "Fabrication of nanoscale gaps in integrated circuits," Appl. Phys. Lett. **81**, 730–732 (2002).

[121] S.M. Dirk S.W. Howell, K. Childs, H. Pang, M. Blain, R.J. Simonson, J.M. TOur, and D.R. Wheeler, "Mass-fabricated one-dimensional silicon nanogaps for hybrid organic/nanoparticle arrays," Nanotechnology **16**, 754–758 (2005).

[122] C.B. Murray, C.R. Kagan, and M.G. Bawendi, "Sythesis and characterization of monodisperse nanocrytals and close-packed nanocrystal assemblies," Annual Reviews of Materials Science **30**, 545–610 (2000).

[123] R.J. Schoelkopf, P. Wahlgren, A.A. Kozhevnikov, P. Delsing, and D.E. Prober, "The radio-frequency single-electron transistor (RF-SET): A fast and ultrasensitive electrometer," Science **280**, 1238–1242 (1998).

[124] W. Lu, Z.Q. Ji, L. Pfeiffer, K.W. West, and A.J. Rimberg, "Real-time detection of electron tunnelling in a quantum dot," Nature **423**, 422–425 (2003).

[125] Y. Manassen, R.J. Hamers, J.E. Demuth, and A.J. Castellano Jr, "Direct observation of the precession of individual paramagnetic spins on oxidized silicon surfaces," Phys. Rev. Lett. **62**, 2531–2534 (1989).

[126] Y. Manassen, I. Mukhopadhyay, and N.R. Rao, "Electron-spin-resonance STM on iron atoms in silicon," Phys. Rev. B **61**, 16223–16228 (2000).

[127] C. Durkan and M.E. Welland, "Electronic spin detection in molecules using scanning-tunneling-microscopy-assisted electron-spin resonance," Appl. Phys. Lett. **80**, 458–460 (2002).

[128] C. Durkan, "Detection of single electronic spins by scanning tunnelling microscopy," Contemporary Physics **45**, 1–10 (2004).

[129] R. Berndt, J.K. Gimzewski, and P. Johansson, "Inelastic tunneling excitation of tip-induced plasmon modes on noble-metal surfaces," Phys. Rev. Lett. **67**, 3796–3799 (1991).

[130] J. Jiang, K. Bosnick, M. Maillard, and L. Brus, "Single molecule Raman spectroscopy at the junctions of large Ag nanocrystals," Journal of Physical Chemistry B **107**, 9964–9972 (2003).